

Observation and model-based analyses of ocean biological carbon fluxes and ecosystem dynamics

ABIGALE M. WYATT

A DISSERTATION
PRESENTED TO THE FACULTY
OF PRINCETON UNIVERSITY
IN CANDIDACY FOR THE DEGREE
OF DOCTOR OF PHILOSOPHY

RECOMMENDED FOR ACCEPTANCE
BY THE DEPARTMENT OF
GEOSCIENCES

ADVISER: LAURE RESPLANDY

MAY 2024

© COPYRIGHT BY ABIGALE M. WYATT, 2024. ALL RIGHTS RESERVED.

ABSTRACT

This dissertation examines the ocean biological carbon pump, a complex coupling of biophysical processes that exports carbon from the surface to the deep (5-15 Pg C yr⁻¹), by focusing on the largest component, the gravitational sinking flux (4-9 Pg C yr⁻¹). In the first chapter, I examine the impact of interannual variability, specifically marine heat waves, on ecosystem and export production in the Northeast Pacific using a suite of observational data and an ocean biogeochemical model. The model shows that warming-induced stratification during marine heat waves relieves winter light limitation while decreasing nutrient supply increasing small phytoplankton production at the expense of large phytoplankton, in agreement with observations. This shift in the phytoplankton assemblage is propagated through the food web, leading to a smaller zooplankton assemblage, and weaker export. I also show that previous observation-based estimates of ecosystem production misattributed a spatial gradient in nutrients to a rapid decline in productivity during a recent marine heat wave. These results highlight the difficulty in disentangling spatial and temporal variability when interpreting sparse observations.

In Chapters two and three, I examine the export proxy, thorium-234, used to estimate particle fluxes in situ. I detail the collection of over 1500 individual water samples collected in the Northeast Pacific and the North Atlantic during the 2018 and 2022 NASA EXPORTS field campaigns. These data were analyzed to produce dozens of particle sinking flux profiles using 1-dimensional (1D) thorium budgets that rely on the assumption that the influence of physical dynamics is negligible relative to the flux of thorium adsorbed on sinking particles. Using observed and simulated velocities, I find that physical processes could bias observed flux estimates by 30% in both regions (Chapter 2). In Chapter 3, using an idealized double gyre model to examine physical thorium transport in fine-scale structures I show that coherent mesoscale eddies (lasting > 20 days) are well-suited for thorium sampling due to the decreased likelihood of strong physical transport. In contrast, frontal regions exhibit large vertical velocities that decouple the sinking flux and 1D thorium estimate, suggesting that thorium-based particle sinking fluxes across frontal regions should be interpreted cautiously.

Contents

ABSTRACT	3
o INTRODUCTION	11
0.1 The biological carbon pump	11
0.2 Challenges associated with observations of particle fluxes	15
0.3 Using models to inform interpretations of export observations	18
i ECOSYSTEM IMPACTS OF MARINE HEATWAVES IN THE NORTHEAST PACIFIC	20
1.0 Abstract	21
1.1 Introduction	21
1.2 Methods	22
1.2.1 Definition of Northeast Pacific marine heat waves	22
1.2.2 Composite anomalies and statistical analysis	22
1.2.3 Line P data processing	23
1.2.4 Ocean biogeochemical model (MOM6-COBALT)	23
1.2.5 Size-fractionated chlorophyll a concentration at OSP	24
1.2.6 Argo floats and other datasets	24
1.3 Results	24
1.3.1 Characterizing marine heat waves in observations and MOM6-COBALT ocean model	24
1.3.2 Northward expansion of nitrate-depleted region in response to marine heat waves	25
1.3.3 Reduced ecosystem production and export in NPTZ	27
1.3.4 Modulated response in the Alaska Gyre	31
1.4 Discussion & Implications	32
1.4.1 Confinement of marine heatwave biological response to the transition zone	32
1.4.2 Collapse of observation-based production misattributed to marine heat wave	32

1.4.3	Shift in phytoplankton assemblage due to contrasting size-class response	34
1.5	Appendix A: Argo NCP Calculation	35
1.6	References	36
2	QUANTIFYING SPATIOTEMPORAL VARIABILITY OF ^{234}Th-DERIVED ESTIMATES OF THE OCEAN BIOLOGICAL CARBON FLUX	38
2.0	Abstract:	39
2.1	Introduction	40
2.1.1	Quantifying sinking fluxes in two export regimes during the NASA EXPORTS program	40
2.1.2	Estimating particulate sinking flux from ^{234}Th dynamics	43
2.1.3	Author's contribution to published works	44
2.2	Methods	45
2.2.1	^{234}Th -derived particle fluxes in the Northeast Pacific	45
2.2.2	Estimating physical transport of ^{234}Th from in-situ observations in the Northeast Pacific	46
2.2.3	Conversion to particle fluxes using size-fractionated particle-to-Th 234 ratios	47
2.2.4	^{234}Th -derived particle fluxes in the North Atlantic	48
2.2.5	Estimating physical ^{234}Th transport inside a simulated North Atlantic eddy	49
2.3	Results	51
2.3.1	Observed ^{234}Th radioactivity and steady-state fluxes near OSP	51
2.3.2	Interpreting change in ^{234}Th radioactivity as temporal variability	52
2.3.3	Interpreting changes in ^{234}Th radioactivity as spatial variability and transport	53
2.3.4	Observed ^{234}Th radioactivity and steady-state fluxes near PAP	55
2.3.5	^{234}Th spatial variability and transport in a simulated North Atlantic eddy	55
2.4	Discussion	57
2.4.1	Spatial vs. temporal variability of sinking fluxes in the Northeast Pacific	57
2.4.2	High-resolution sampling captures fine-scale spatial variability	59
2.4.3	North Atlantic small-scale spatial variability	60
2.5	Conclusions	61

3	EVALUATION OF 1D THORIUM MODELS AND EXPORT AROUND DYNAMIC PHYSICAL STRUCTURES LIKE EDDIES AND FRONTS	62
3.0	Abstract	63
3.1	Introduction	64
3.2	Methods	68
3.2.1	Ocean model description	68
3.2.2	^{234}Th sinking fluxes: 1D-SS and 1D-NSS models	70
3.2.3	Eddy detection and selection	72
3.2.4	Identification of frontal regions	74
3.3	Results	75
3.3.1	Simulated contrasts between eddies and frontal regions	75
3.3.2	Lagrangian eddy sampling improves high sinking flux estimates . .	77
3.3.3	Strong vertical transport in frontal regions obscures sinking flux estimates	80
3.4	Discussion	84
3.4.1	Efficacy of the steady-state model	84
3.4.2	Systematic underestimation of sinking fluxes using the 1D-SS estimate	86
3.4.3	Frontal dynamics may inhibit the interpretation of sinking fluxes .	87
3.5	Conclusions	89
4	CONCLUSION	91
REFERENCES		95

Listing of figures

1	Snapshot of eddy kinetic energy using velocity field from Ocean Surface Currents	13
2	Example of observed and modeled particulate organic carbon (POC) flux variability and net community production at Ocean Station Papa (OSP) in August	16
1.1	Observations of SST and Chl compared to MOM6-COBALT	23
1.2	Argo float trajectories overlaid on late summer surface nitrate concentrations in WOA and MOM6-COBALT	25
1.3	Comparison of observations from BGC-Argo floats and subsampled MOM6-COBALT	26
1.4	Impact of 2014-2015 warm blob along Line P	27
1.5	Annual mean surface nitrate concentrations from WOA and MOM6-COBALT	28
1.6	Modeled composite anomaly of the nine marine heatwaves	29
1.7	MHW anomalies for the 9 individual years and their composite vs. one standard deviation	30
1.8	Seasonal response to MHWs in the NPTZ	31
1.9	Seasonal response to MHWs in the AG	33
1.10	Observed and modeled summer chlorophyll contained in large and small phytoplankton in the AG and NPTZ	33
1.11	Net community production (NCP) calculated as nitrate drawdown from winter inventory using BGC-Argo data and subsampled model	34
2.1	Sampling locations of NASA EXPORTS field campaigns. a) Mean June chlorophyll concentration with June satellite chlorophyll concentration . .	41
2.2	Thorium-234 activity and chlorophyll fluorescence versus density with equivalent depths on secondary y-axis	52

2.3	Epoch average 1D-SS ^{234}Th flux with integrated vertical advection and diffusion included	54
2.4	Edge experiment, sampling across a front	56
2.5	Observed North Pacific EXPORTS POC flux at 50 m and mean observed trend vs. subsampled MOM6-COBALT model 2018 output	58
3.1	Schematic of thorium-234 and uranium-238 radioactivity in the water column	66
3.2	NEMO-LOBSTER model snapshot	69
3.3	Spatial and temporal distribution of simulated eddies in the model domain .	73
3.4	Probability density distributions inside eddies and fronts	76
3.5	Example of an eddy trajectory, fluxes and thorium budget in eddy	78
3.6	Classification of eddies based on their relative 1D-SS and 1D-NSS-eddy errors	79
3.7	Edge-like transect location over model surface phytoplankton biomass	80
3.8	Transect sampling across a front	82
3.9	Profiles of sampling across a front	83
3.10	How representative are eddies of the flux surrounding them?	85

Acknowledgments

THE FIRST PERSON I NEED TO THANK IS MY PARTNER, Brian Yust.

I also want to thank my lab group. They are the best.

And Laure.

And the rest of the department.

Esp. my committee, Bess and Gabe.

My family too.

Everyone from NASA EXPORTS especially Ken, Claudia, Sam, Muntsa.

It was in the paper. I assumed they checked their facts.

—Steve Zissou

0

Introduction

0.1 THE BIOLOGICAL CARBON PUMP

The ocean biological pump (BCP) is a mechanism that annually transports 5-15 Pg C yr⁻¹ from the surface into the deep ocean (Emerson et al., 2014; Boyd et al., 2019; Wang et al., 2023), acting as a significant regulator of atmospheric CO₂. In the surface ocean, photosynthetic organisms called phytoplankton take up inorganic carbon and convert it into

organic matter. This organic carbon is subsequently transformed through predator-prey interactions, metabolic processes, and nutrient kinetics, with a fraction escaping surface recycling and exported to the ocean interior, where it is isolated from the atmosphere on timescales of decades to thousands of years depending on the depth at which it is sequestered and remineralized (Archer et al., 2000; Kwon et al., 2009; DeVries et al., 2012; Palevsky and Doney, 2018). Global estimates of carbon export stem from several techniques: direct extrapolation from in-situ observations (Henson et al. 2011), coupled food web-physical circulation models (Bopp et al. 2001, Stock et al., 2020; Kwiatkowski et al., 2020), or observation-informed inverse models (Siegel et al. 2014; Wang et al., 2023). However, the observations and models on which these estimates are based are globally coarse, only providing fleeting glimpses of the biological carbon pump spatio-temporal variability and relying on sometimes crude representations of the processes that control it.

The BCP consists of a myriad of pathways, including the gravitational sinking of particulate matter, zooplankton diurnal and seasonal migration, and physical pumps associated with mixed layer entrainment and large-scale and eddy-induced subduction (e.g., Steinberg & Landry, 2017; Boyd et al., 2019, Resplandy et al 2019). Although the gravitational sinking flux is arguably the best-known and most studied pathway, it is still one of the largest sources of uncertainty of the BCP, accounting for $4\text{-}9 \text{ Pg C yr}^{-1}$ (DeVries & Weber, 2017; Boyd et al., 2019). Uncertainties in global estimates of the gravitational sinking flux arise from the high complexity and spatio-temporal variability of biophysical processes regulating the production and export of particulate organic carbon. Primary and secondary production in the euphotic zone spawn an assortment of particulate debris such as dead plankton and fecal pellets, the characteristics and quantity of which vary with the plankton

assemblage and amount of net ecosystem production. The particulate detritus rains down from the surface, with sinking speeds and remineralization rates set by their size, density, porosity, content and ecosystem composition (McDonnell and Buesseler 2010; Riley et al. 2012; Omand et al., 2020, Luo et al 2020, Baumann et al., 2023) and aggregation and disaggregation throughout the water column (Alldredge and Silver 1988; Lam and Marchal, 2015). These processes vary at the scale of ocean eddies and filaments (1 – 100 km), Benitez Nelson et al 2007; Maas et al., 2014; Stuckel et al 2017, 2018; Steinberg & Landry, 2017; Resplandy et al 2019) and on interannual time-scales (Karl et al., 1996; Lampitt et al., 2010) requiring numerous large observations datasets to capture this broad range of spatio-temporal scales.

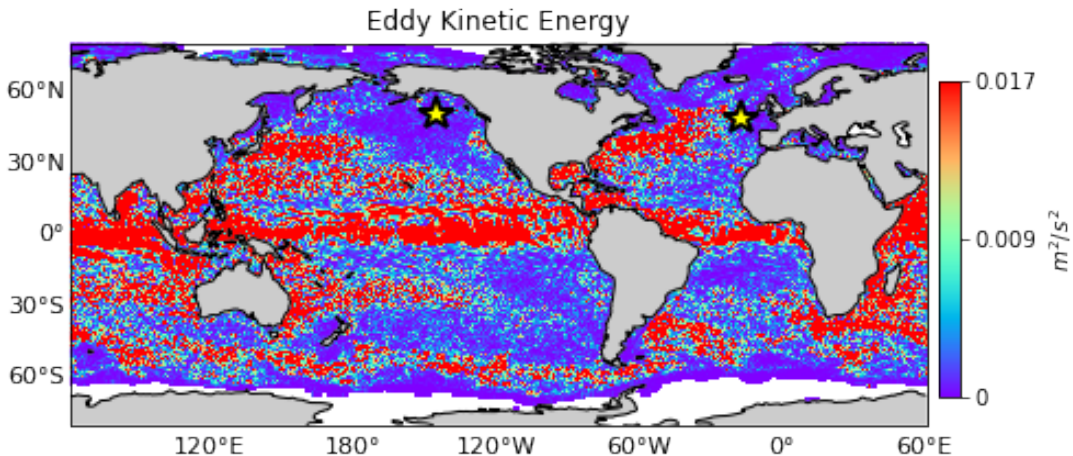


Figure 1: Snapshot (Oct 16, 2019) of eddy kinetic energy using velocity field from Ocean Surface Currents Analyses Real-time (OSCAR, EKE is approximated here as $(u' + v')/2$ where u' and v' are deviations from the annual mean zonal and meridional components of the velocity). EXPORTS 2018 (Pacific) and 2022 (Atlantic) field campaign locations are shown as yellow stars.

The NASA EXport Processes in the Ocean from Remote Sensing (EXPORTS) program was a large-scale sampling program specifically designed to observe and quantify the

various mechanisms controlling the BCP, including the particulate sinking flux (Siegel et al., 2016). By deploying several observational platforms in two contrasting export regimes: the Northeast Pacific Ocean in 2018 (Siegel et al., 2021) and the North Atlantic Ocean in 2022 (Johnson et al., 2024) the EXPORTS program collected co-located and concurrent high-resolution datasets characterizing primary production, secondary production, sinking fluxes, and inorganic nutrient concentrations, as well as ancillary datasets such as optical and acoustic data.

The Northeast Pacific is characterized by low eddy kinetic energy (EKE, Fig. 1) physical dynamics, limited seasonality in primary production due to iron limitation (Martin & Fitzwater, 1988), a relatively low export ratio, the ratio of the exported matter to the amount produced by phytoplankton, and low transfer efficiency, the flux attenuation from just below the surface mixed layer to deeper depths (Buesseler & Boyd, 2009). Long term datasets in the region, including the Ocean Station Papa (OSP) dataset going back to 1949 (Freeland 2007), the Canadian Line P program (Pena & Varela, 2007) and biogeochemical Argo floats (Plant et al., 2016) suggest, however, that plankton and export production are sensitive to interannual variability (Wong et al., 1999; Harrison 2002) and extreme temperature anomalies, also called marine heat waves (Yang et al., 2018; Bif et al., 2019).

The North Atlantic, in contrast, is characterized by high EKE (Fig. 1), a strong spring phytoplankton bloom (Siegel et al., 2002; Henson et al., 2009; Yang et al., 2021) and intense mesoscale and submesoscale dynamics (Garçon et al., 2001; Erickson & Thompson, 2018). Such fine-scale dynamics and associated intense vertical velocities induced by fronts have been shown to modulate plankton production (Mahadevan et al., 2012, 2016, Freilich and Mahadevan, 2019; Levy et al., 2012, 2024) and the magnitude of sinking fluxes lo-

cally (Benitez-Nelson et al., 2007; Buesseler et al., 2008; Resplandy et al., 2019; Stukel et al., 2017, 2018).

In this work, we combine observational datasets with coupled physical-biogeochemical models to further our understanding of the BCP response to interannual and fine-scale variability and test BCP observational sampling methods. In the Northeast Pacific primary, secondary and export production are influenced by year-to-year variations introduced by marine heatwaves, which we examine in Chapter 1 of this dissertation. In the North Atlantic, fine-scale physical dynamics influence particle fluxes and observation based estimates of them, thus an assessment of the impact of small scale spatial and temporal variability of the sinking fluxes is necessary for refined interpretation of the EXPORTS data, which is the subject of Chapters 2 and 3 of this work.

0.2 CHALLENGES ASSOCIATED WITH OBSERVATIONS OF PARTICLE FLUXES

Different in situ observation methods of export can yield a wide range of sinking flux estimates (Fig. ??), for instance, during the 2018 EXPORTS cruise sinking flux observations at OSP included floating sediment traps (red diamonds, black outline) and the thorium-proxy method (blue triangles, black outline, Fig. 2). Both approaches show a higher flux of about $3 \text{ mmol m}^{-2} \text{ d}^{-1}$ at 100 m that decreases with depth reaching values of $1 \text{ mmol m}^{-2} \text{ d}^{-1}$ at 500 m. Yet, the different techniques show significant uncertainty with estimates ranging from $1 - 6 \text{ mmol C m}^{-2} \text{ d}^{-1}$. Further, the comparison of observations taken in 2018 (markers with black outline) to trap and thorium derived fluxes from prior years (red and blue markers without black outline) moored traps (1983-2006, yellow squares) and Argo float-derived net community production (2008-2018, purple circles), reveals that interan-

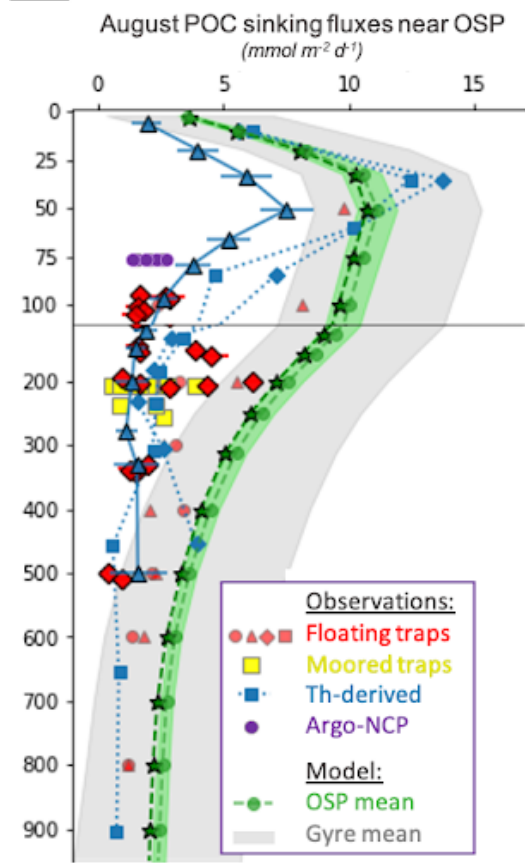


Figure 2: Example of observed and modeled particulate organic carbon (POC) flux variability and net community production at Ocean Station Papa (OSP) in August. Observational datasets include floating sediment traps (red markers, Timothy et al., 2013; Estapa et al., 2021); moored sediment traps (yellow markers, Wong et al., 1999), thorium-derived fluxes (blue markers, Charette et al., 1999, Buesseler et al., 2020) and net community production derived from Argo float nitrate concentrations (purple circles, Plant et al., 2016). Individual profiles are connected by the shape of the marker. Black outlines on the marker indicate they were from the 2018 NASA EXPORTS cruise. Modeled data from MOM6-COBALT (Wyatt et al., 2022) includes OSP mean from 1958–2020 (green circles with shaded band indicating 1-standard deviation), OSP in 2018 specifically (green stars, black outline) and the entire subpolar gyre (gray shading).

annual variability in this region can influence sinking fluxes by a factor of > 2 (e.g. from 7 - 14 $\text{mmol C m}^{-2} \text{d}^{-1}$ at 50 m).

Sediment traps, arguably the most direct observational method, are effectively buckets deployed at depth moored to the ocean floor, attached to a surface drifter, or untethered neutrally buoyant floats (Estepa et al., 2020, e.g., red and yellow symbols in Fig. 2). They

physically intercept and passively collect sinking material over time (Honjo and Manganini 1993; Wong et al. 1999). Trap estimates, however, may be biased by the hydrodynamics of the surrounding flow (Buesseler et al., 2009), the difficulty in collecting slow sinking fluxes (Baker et al., 2020), or by particle consumption and contamination by zooplankton (Buesseler et al, 2007). Further, traps are often deployed on time scales of days to months and often at depths well below the euphotic zone so they do not provide high-resolution estimates of particle

In contrast, the naturally occurring thorium-234 (^{234}Th) uranium-238 (^{238}U) radio-tracer pairing, which has been used for several decades, can be used as a proxy for particle export (Buesseler, 1998; Benitez-Nelson et al. 2001, e.g., blue symbols in Fig. 2). This indirect method assumes that the difference between the particle-reactive daughter isotope, ^{234}Th , and the conservative parent, uranium, is due to the former's attachment to sinking particles. This approach requires multiple, two-liter water (previously ten liters) samples per flux profile (Benitez-Nelson et al., 2004, Clevenger et al., 2021) and a concurrent assessment of the carbon- ^{234}Th ratio to convert the ^{234}Th flux to a carbon flux. While this method can provide high-resolution flux estimates it is constrained by the halflife of ^{234}Th (24 days) and relies on a 1-dimensional accounting of ^{234}Th activities ignoring any contribution from fine-scale physical dynamics, thus short-term variations in particle fluxes and physical transport of ^{234}Th can be difficult to quantify.

A third method is mass balance framework, perhaps the most indirect method of export flux estimation, equating export with net community production (NCP) under steady-state assumptions. This framework uses the time-variance of in situ concentrations of biologically important tracers such as nitrate, dissolved inorganic carbon, or oxygen, which

can often be observed from autonomous vehicles like Argo floats (e.g. Haskell et al., 2020, Argo-NCP in Fig. 2). The consumption and production of these tracers during photosynthesis can be estimated by quantifying concentration changes due to ocean dynamics and atmospheric interactions. These frameworks, however, are generally limited by their ability to accurately constrain the physical dynamics and may conflate spatial variability with temporal variability as I show in this dissertation (Chapter 2, Wyatt et al., 2022).

0.3 USING MODELS TO INFORM INTERPRETATIONS OF EXPORT OBSERVATIONS

The modeling of export fluxes is based on the observations highlighted in section 2. These observational techniques generally agree that export fluxes in the ocean resemble a simple power law (Fig. 2 and Equation 1, Martin et al., 1987).

$$\Phi_z = \Phi_{z_0} \left(\frac{z}{z_0} \right)^b \quad (1)$$

Where Φ_z is the export flux at a given depth, z , which can be predicted from the known flux at a reference depth, Φ_{z_0} , (often $z_0 = 100$ m) given the dimensionless attenuation coefficient parameter, b , (0.70 - 0.98, Gloege et al., 2017). This parameter can be determined from regional flux rates, with larger values indicating faster attenuation and increased remineralization. More recently, other parameterizations such as exponential or rational fits, have been proposed (Cael & Bisson, 2018), with adjustments for temperature and oxygen dependencies (lower temperature and lower oxygen concentrations leading to lower remineralization rates, Laufkötter et al., 2017).

Ocean biogeochemical models like the models used in this thesis (COBALT in Chapter 1 Resplandy et al., 2012; and LOBSTER in Chapter 3, Stock et al., 2020) simulate the

fundamental processes that control organic matter production in the upper ocean. These biogeochemical models simulate the fluxes of nutrients and carbon between the dissolved stocks (nitrate, ammonium, iron, dissolved organic matter etc.) and groups of phytoplankton, zooplankton, and detritus, and are coupled to general circulation models (e.g., GFDL-MOM6 or IPSL-NEMO, Adcroft et al., 2019; Madec et al., 2008) that resolve the fundamental equations that represent radiative transfer, thermodynamics, fluid dynamics, and transport processes. These models coupling ocean dynamics and biogeochemistry expand the temporal and spatial coverage of observations providing an opportunity to build on our mechanistic understanding of the BCP. For example, we can examine the impacts of spatiotemporal variability, such as interannual anomalies, large-scale circulation, or fine-scale dynamics, on ecosystem production and export, and we can assess the biases and uncertainties introduced by sparse sampling by sub-sampling model outputs similarly to field observations, e.g. using autonomous float trajectories or ship tracks.

In this work, I re-contextualize observational data from the Northeast Pacific by sub-sampling a coupled physical-biogeochemical model to examine the influence of interannual variability, specifically, marine heat waves, on the BCP, finding that the phytoplankton response varies with size class, leading to a decrease in particulate export (Chapter 1). Then I contrast the impact of physical transport on in situ observations of thorium-derived fluxes in both the Northeast Pacific and North Atlantic Oceans (Chapter 2), finishing with a deeper dive analyzing the impact of fine-scale dynamics on production and export near eddies and filaments in North Atlantic, with an assessment of sampling strategies using a high resolution, eddy-permitting model (Chapter 3).

*Supposedly Cousteau and his cronies invented the idea
of putting walkie-talkies into the helmet. But we made
ours with a special rabbit ear on the top so we could pipe in
some music.*

—Steve Zissou

1

Ecosystem impacts of marine heatwaves in the Northeast Pacific



Ecosystem impacts of marine heat waves in the northeast Pacific

Abigale M. Wyatt¹, Laure Resplandy^{1,2}, and Adrian Marchetti³

¹Department of Geosciences, Princeton University, Princeton, NJ, USA

²High Meadows Environmental Institute, Princeton University, Princeton, NJ, USA

³Earth, Marine and Environmental Sciences, University of North Carolina, Chapel Hill, NC, USA

Correspondence: Abigale M. Wyatt (awyatt@princeton.edu)

Received: 25 February 2022 – Discussion started: 8 March 2022

Revised: 1 September 2022 – Accepted: 28 October 2022 – Published: 14 December 2022

Abstract. Marine heat waves (MHWS) are a recurrent phenomenon in the northeast Pacific that impact regional ecosystems and are expected to intensify in the future. Prior work showed that these events, including the 2014–2015 “warm blob”, are associated with widespread surface nutrient declines in the subpolar Alaska Gyre (AG) and the North Pacific Transition Zone (NPTZ) but reduced chlorophyll concentrations in the NPTZ only. Here we explain the contrast between these two regions using a global ocean biogeochemical model (MOM6-COBALT) with Argo float and ship-based observations to investigate how MHWS influence marine productivity. We find that phytoplankton and zooplankton production respond relatively modestly to MHWS in both regions. However, differences in the response to seasonal iron and nitrogen limitation between large ($>10\text{ }\mu\text{m}$) and small ($<10\text{ }\mu\text{m}$) phytoplankton size classes explain the differences in ecosystem response to MHWS across the two biomes. During MHWS, reduced nutrient supply limits large phytoplankton production in the NPTZ (−13 % annually) but has a limited impact on the already iron-limited large phytoplankton population in the AG (−2 %). In contrast, MHWS yield a springtime increase in small phytoplankton in both regions due to shallower mixed layers and weaker light limitation. These modest changes are in apparent contradiction with prior estimates suggesting a collapse in net community production during the warm blob. We show, however, that 70 % of the decline in net community production previously calculated from nitrate Argo data can be attributed to artifacts in the method and that only 30 % can be attributed to interannual variability, in line with our model-based results. Although modest, the primary production anomalies associated with MHWS modify the phytoplankton size distribution, resulting in a significant shift towards small phytoplankton pro-

duction (i.e., lower large-to-small-phytoplankton ratio) and reduced secondary and export production, especially in the NPTZ.

1 Introduction

Marine heat waves (MHWS) are a recurring phenomenon in the northeast Pacific, with nine events on record since 1958 (Xu et al., 2021). The largest such event, which occurred during the satellite chlorophyll era, was a persistent marine heat wave known as the “warm blob” that appeared in 2014 and 2015 and was characterized by a greater than 2°C surface temperature anomaly in the northeast Pacific (Freeland and Whitney, 2014; Bond et al., 2015; Di Lorenzo and Mantua 2016). The 2014–2015 marine heat wave broadly influenced ecosystems in the northeast Pacific Ocean with a shift in marine species’ geographical distribution and anomalous appearances of fish species outside of their known range across the northeast Pacific (see Bond et al., 2015) with some effects persistent or permanent (Suryan et al., 2021). In situ observations indicate that the warm blob particularly affected ecosystems in two regions: the subpolar Alaska Gyre (AG) and the North Pacific Transition Zone (NPTZ roughly between 30 to 45° N), i.e., the region of strong chlorophyll and nitrate gradient that demarcates the boundary between the AG and the eastern subtropical gyre. Major impacts of this warm blob included a $\sim 35\%$ decrease in satellite surface chlorophyll in the NPTZ (Whitney et al., 2015), a reduction in surface nitrate concentrations and phytoplankton biomass, and an increase in cyanobacteria dominance along the subarctic transect Line P which samples both the NPTZ and AG regions (near 50° N , Peña et al., 2019). Further, es-

timates of net primary productivity suggested there was an ecosystem collapse in the second year of the warm event near Ocean Station Papa in the AG (OSP, 50.1° N, 144.9° W, Bif et al., 2019b), despite a lack of satellite surface chlorophyll anomaly in this region.

Prior work offered a bottom-up explanation for the chlorophyll anomalies observed in the NPTZ during MHWs, noting that the 2014–2015 heat wave was associated with decreased winds that reduced nitrate concentrations and inhibited primary production (Whitney, 2015). This bottom-up explanation does not explain why the decrease in chlorophyll was highly localized (confined to the NPTZ) while anomalously low nitrate concentrations extended 600 km north (into the AG) of any significant chlorophyll anomalies (Peña et al., 2019). In addition, surface chlorophyll alone provides little information on food web changes or how marine heat waves influence secondary production and marine biogeography. Finally, it is unclear to what extent the observed anomalies in nitrate and chlorophyll are unique to the warm blob or typical of the MHWs in this area.

The AG and NPTZ are distinct ecological biomes. The AG is a high-nutrient, low-chlorophyll (HNLC) region, characterized by high nitrate concentrations but moderate primary production throughout the year due to iron limitation that prevents the development of a strong spring bloom (Martin and Fitzwater, 1988; Harrison, 2002; Boyd et al., 2004; Peña and Varela, 2007). In contrast, the NPTZ is a region characterized by strong seasonality in nitrate and chlorophyll due to the seasonal biological consumption and the Ekman transport of nutrients (Chai et al., 2003; Polovina et al., 2008; Ayers and Lozier, 2010). As a result, the NPTZ evolves from a subpolar-like, iron-limited biome when nitrate is abundant in spring to a nitrate-depleted, subtropical-like biome in summer, with the position of the chlorophyll front associated with the bloom (2 mg m^{-3} chlorophyll contour) shifting $\sim 10^\circ$ northward in summer from its southernmost position in winter (30 to 40° N, Bograd, et al., 2004; Glover et al., 1994).

In this study, we examine the ecosystem response to the nine MHWs that were recorded since 1958 in the AG and NPTZ biomes. Using a combination of observations and ocean biophysical model results, we first characterize MHWs in Sect. 3.1. Then in Sect. 3.2, we examine the extent of nitrate depletion during MHWs and show that the boundary between the subpolar HNLC region and the NPTZ shifts during these events, expanding the region of nitrate depletion. We then analyze the biological response to MHWs in the NPTZ and the contrasting response in the AG (Sect. 3.3 and 3.4), with particular emphasis on the responses of the two phytoplankton size classes. Our results indicate that during MHWs, though the chlorophyll anomaly is confined to the NPTZ, both regions exhibit a shift in the phytoplankton assemblage toward the smaller size class, resulting in the reduction of secondary and export production.

2 Methods and datasets

2.1 Definition of northeast Pacific marine heat waves

Following the method of Xu et al. (2021), we calculate the area mean sea surface temperature anomalies (SSTa) relative to the climatology of the region 35 to 46° N, 150 to 135° W using the monthly data from 1958–2020 of the Extended Reconstruction SST dataset (ERSSTv4, Huang et al., 2015). Northeast Pacific marine heat waves are defined as periods when the monthly deviation relative to the climatology exceeds 1 standard deviation for 5 months or more. The same method is used to detect marine heat waves in the ocean model (see Sect. 2.3 for model details). We define heat waves considering their impact on the spring–summer blooming season. For example, what we refer to as the “year 1990 heat wave” started in November 1989 and ended in March 1990, thus impacting the ecosystem in 1990. In both ERSST and the model, the marine heat waves or warm years selected using these criteria are 1962, 1963, 1965, 1990, 1991, 2005, 2014, 2015 and 2019, similar to what was found by Xu and coauthors (Fig. 1).

2.2 Composite anomalies and statistical analysis

We compute the composite of the nine MHW events to evaluate the impact of heat waves on marine ecosystems, examining SST, mixed layer depth (MLD), surface nutrients and six ecosystem variables (chlorophyll, large phytoplankton production, small phytoplankton production, ratio of large to small phytoplankton production, zooplankton production and export production). To calculate the MHW composite, we remove the 1958–2020 linear warming trend at each model grid point. The climatology of all years was calculated at each spatial point and removed from the 9 selected MHW years to get the annual anomalies of each MHW year. The 9 MHW years were then averaged together to get a single, composite MHW year. To quantify the size of the perturbations caused by MHWs, we compared the magnitude of the MHW anomalies to the variability during non-MHW years calculated as the average monthly standard deviation. We focus on two subregions representative of the NPTZ (39 to 45° N and 160 to 135° W) and the HNLC Alaska Gyre (48 to 54° N and 160 to 145° W)

To test whether the spatially averaged MHW anomalies ($N = 9$) differed significantly from the non-MHW years ($N = 53$), the six ecosystem variables were compared across the two datasets using the two-variable Kolmogorov–Smirnov (K-S) test. This test is a suitable choice as it does not require a normal probability distribution or equal variance of the two datasets. A threshold p value <0.05 is used throughout this paper to indicate “significant” differences, indicating that changes in that variable are attributable to MHWs. For annual values, production variables were annually integrated, and chlorophyll was annually averaged. For seasonal values,

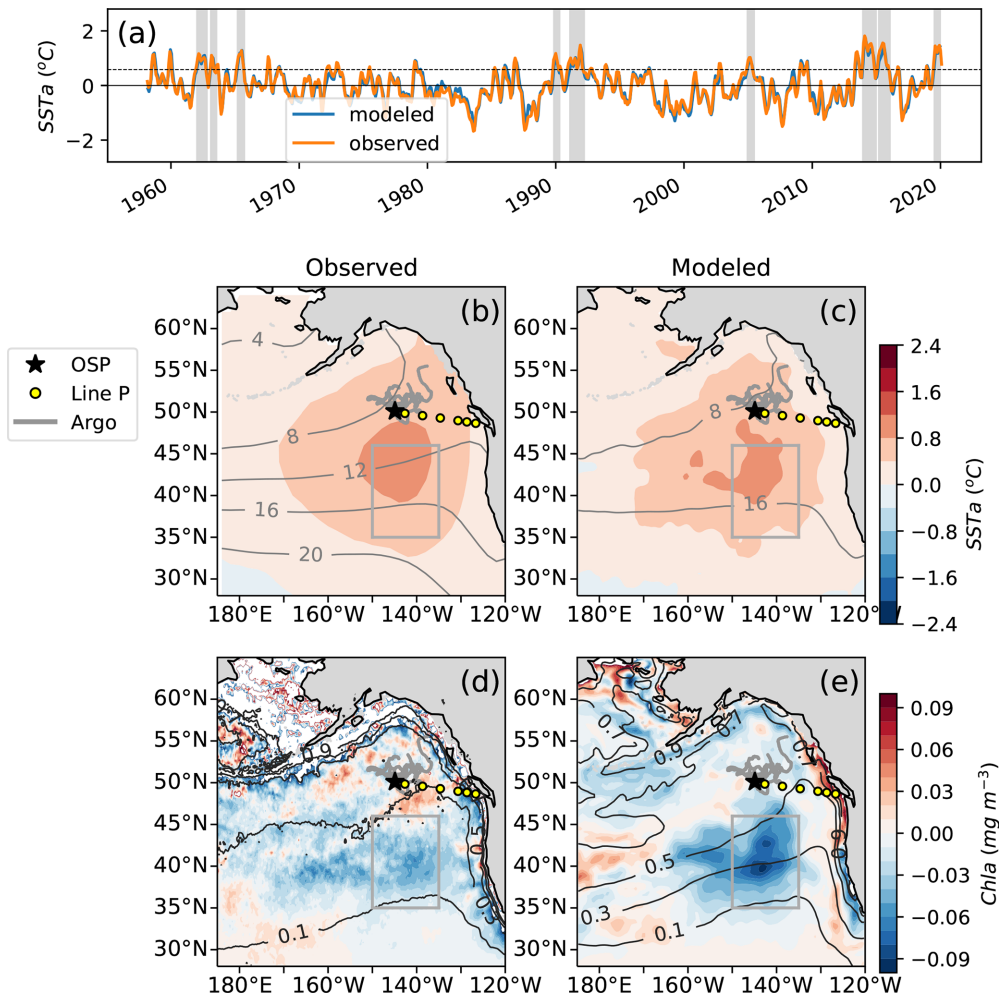


Figure 1. (a) Observations of sea surface temperature anomalies (SSTa) from extended reconstructed sea surface temperature data (ERSST, orange) compared to MOM6-COBALT simulated SSTa (blue) averaged for 1958–2020 across 35 to 46° N and 150 to 135° W (gray boxes b–e, following Xu et al., 2021; see methods Sect. 2.1). (b) Observational and (c) modeled spatial pattern of the SSTa composite of the 9 MWHs overlaid with SST climatology (black contours). (d) Observed and (e) modeled spatial pattern of the chlorophyll anomalies (Chl *a*) composite of the last four warm events (2005, 2014, 2015, 2019) for which observational chlorophyll data (GlobColour) are available overlaid with the surface chlorophyll climatology (dark gray contours). Line P (P1–P26) shown as yellow circles at every fourth Line P station with the black star denoting P26, also known as Ocean Station Papa (OSP, 50° N, 145° W). Trajectories of BGC-Argo floats with nitrate sensors in the region for 2008–2018 are shown in gray.

the appropriate month(s) were selected and averaged. As we used annual or seasonal mean data, we assume that autocorrelation is negligible and calculate significance based on the total number of years in the time series.

2.3 Line P data processing

We use Line P observations of temperature, salinity, nitrate and Chl *a* available online (downloaded from <https://www.waterproperties.ca/linep>, last access: 19 March 2021). Data from the two summertime cruises, May and June and August/September, were averaged at each of the 26 stations from 2007 to 2020. The January/February cruise data were not used as we focused on the period of seasonal nitrate de-

pletion. For comparison, the model results were sampled at the same station locations, averaged across June, July and August each year to obtain a summer mean.

2.4 Ocean biogeochemical model (MOM6-COBALT)

This study uses the biophysical ocean model described in Liao et al. (2020). This model configuration uses the fourth-generation global ocean/sea ice model OM4p5 developed at the Geophysical Fluid Dynamics Laboratory (GFDL), consisting of the Modular Ocean Model version 6 (MOM6) and the Sea Ice Simulator version 2 (SIS2, Adcroft et al., 2019). The physical ocean circulation model has a nominal 0.5×0.5 resolution in the horizontal and 75 hybrid depth-

isopycnal z^* layers in the vertical. The physical model is coupled with the biogeochemical model Carbon, Ocean Biogeochemistry and Lower Trophics v.2 (COBALTv.2) that simulates a nitrogen-based ecosystem with 33 biochemical tracers and 13 food web components (Stock et al., 2014, 2020). These components include three phytoplankton size classes: large ($>10\text{ }\mu\text{m}$), small ($<10\text{ }\mu\text{m}$) and nitrogen-fixing diazotrophs. Phytoplankton growth is explicitly modeled as size-dependent functions of light, temperature and nutrient limitations (nitrate, ammonia, phosphate, etc.). Small phytoplankton are simulated to be efficient nutrient and light harvester (Munk and Riley, 1952; Geider et al., 1997), in contrast to large phytoplankton, which are parameterized to grow quickly in response to abundant nutrients. For macronutrients (e.g., nitrogen, phosphate), limitation factors are calculated using saturating kinetics, while for iron, an internal iron deficiency term is calculated based on an internal cell quota (see Supplement Eqs. S1–S5 in Stock, 2014, for details). These limitation factors are output from the model as a number between zero and one, with zero indicating complete limitation, i.e., no phytoplankton growth. The nutrient with the lowest value is considered the limiting nutrient (Droop, 1983). Notably, in the study regions, iron is only a limiting nutrient for large phytoplankton. The model also includes three zooplankton size classes of which large ($>2000\text{ }\mu\text{m}$) and medium (200 to $2000\text{ }\mu\text{m}$) make up the mesozooplankton pool with a third, separate small zooplankton class ($<200\text{ }\mu\text{m}$), all of which consume phytoplankton using size-related predator–prey relationships. These nitrogen-based biological tracers are assumed to maintain a stoichiometric relationship with carbon in accordance with the Redfield ratio, $^{106}\text{C} : ^{16}\text{N}$. Chlorophyll is calculated from phytoplankton biomass using a Chl:C ratio that depends on ambient light, temperature, iron availability and size-class-specific nutrient limitation and maximum photosynthetic rates (Geider et al., 1997; Stock et al., 2014, 2020).

The model was spun up from rest using three repetitions of the 1958 to 1985 Japanese atmospheric reanalysis v1.4 (JRA55do v1.4, Tsujino et al., 2018) for a total of 81 years. Initial nutrient, temperature and salinity fields are from the 2013 World Ocean Atlas (WOA, Boyer et al., 2013). Dissolved inorganic carbon (DIC) and alkalinity are from the global ocean data analysis project v2 climatologies (GLO-DAPv2, Olsen et al., 2016), with DIC corrected to 1958 using anthropogenic carbon concentrations from Khatiwala et al. (2013). Initial states of the remaining tracers (Chl, biomass, etc.) were taken from a long, preindustrial control run from the GFDL Earth system model ESM2M-COBALT (Dunne et al., 2012). The model was then run from 1958 to 2019 using the JRA v1.4 forcing and river nutrient fluxes taken from the global NEWS climatology (Seitzinger et al., 2010).

2.5 Size-fractionated chlorophyll *a* concentration at OSP

Discrete summertime measurements of mixed layer, size-fractionated Chlorophyll *a* (Chl *a*) concentrations at OSP were obtained through collection of 300 mL of seawater from a Rosette system during Line P cruises in June of 2000, 2001, 2008, 2013, 2015 and 2018. The 2015 sample was taken during the warm blob, while the 2013 sample was collected following the Mt. Pavlof eruption (Waythomas et al., 2014). Seawater was vacuum filtered through a $5\text{ }\mu\text{m}$ pore-sized polycarbonate filter, and the filtrate was passed through a GF/F filter ($0.7\text{ }\mu\text{m}$ nominal porosity) set up in series. Filters were frozen at -80°C until analysis. Chl *a* extraction was performed using 90 % acetone or ethanol at -20°C overnight, and concentrations were determined fluorometrically using a Turner Designs 10 AU fluorometer (Brand et al., 1981).

Phytoplankton in the study regions are classified into two allometric classes. Small phytoplankton ($<5\text{ }\mu\text{m}$ vs. $<10\text{ }\mu\text{m}$ in model), primarily made up of cyanobacteria (e.g., *Synechococcus*) and nanoflagellates such as chlorophytes and haptophytes, comprise the majority of the biomass in both regions (Boyd and Harrison, 1999). Large phytoplankton ($>5\text{ }\mu\text{m}$ vs. $>10\text{ }\mu\text{m}$ in model), primarily made up of dinoflagellates and diatoms, have a stronger correlation to particulate export production (Buesseler, 1998) and are subject to iron limitation inside the AG.

2.6 Argo floats and other datasets

This study makes use of the 2008–2018 series of BGC-Argo floats with nitrate sensors deployed near OSP (Fig. 2). Specifically, we replicated the analyses of Plant et al. (2016) as updated in Bif et al. (2019a) to evaluate net community production (NCP) from BGC-Argo float nitrate data and then compare NCP estimates derived from nitrate concentrations in the WOA climatology and the MOM6-COBALT model (see Appendix A). Following the quality control analyses of those studies, selected profiles from floats 5903405, 5903891 and 5903714 were dropped due to inconsistencies in the nitrate data (see Bif and Hansell 2019a). Satellite chlorophyll observations (1997 to 2020) are from the GlobColour dataset (<http://globcolour.info>, last access: 9 December 2022), which has been developed, validated and distributed by ACRI-ST, France (Maritorena et al., 2010).

3 Results

3.1 Characterizing marine heat waves in observations and MOM6-COBALT ocean model

Marine heat waves show systematically high SST over a relatively broad area of the northeast Pacific that extends from 35 to 55°N and from 170°E to the North American coast

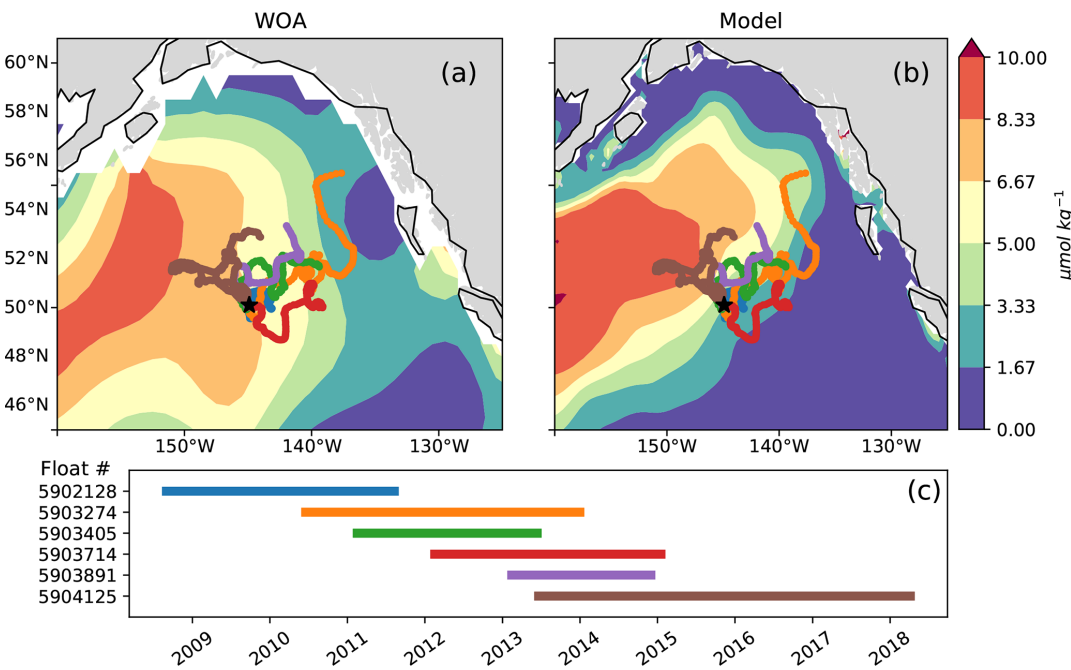


Figure 2. Argo float trajectories overlaid on late summer (August) surface nitrate concentrations in (a) the World Ocean Atlas and (b) MOM6-COBALT. The sampling period of each float is shown in panel (c). Note that float 5904125 (brown) travels west across the east–west nitrate gradient and is the only float sampling the region between 2015 and 2018.

in both observations and the MOM6-COBALT model (up to $+1^{\circ}\text{C}$ on average across the nine events, Fig. 1c, d). Surface Chl, in contrast, exhibits more spatial heterogeneity, with a strong decline in the NPTZ (-0.05 mg m^{-3}) and a mild increase further north in the AG ($+0.02 \text{ mg m}^{-3}$ around station OSP, Fig. 1d, e).

We use the observations from six Argo floats that sampled the AG region around OSP between the years 2008 and 2019 to characterize interannual variability in the region (Fig. 2). These data show the strong signal associated with the 2014–2015 warm event, colloquially termed the warm blob, including summer surface temperatures above 15°C and surface nitrate concentrations below $6 \mu\text{mol kg}^{-1}$ (Fig. 3a, c, e). Using the ocean model sampled along the floats' trajectories yields similar features, with modeled temperatures exceeding 14°C and nitrate concentrations dropping to $<3 \mu\text{mol kg}^{-1}$ during the warm blob period (Fig. 3b, d, f). It is worth noting that in both the observed and modeled profiles, large changes in temperature, nitrate and to a lesser extent salinity are apparent at depth ($>100 \text{ m}$) in early 2015 (see also sampled WOA profiles in Fig. S2). These subsurface changes were sampled by a single float (no. 5904125, brown, Fig. 2) and likely indicate sampling of a different water mass with a shallower thermocline and nitracline, in this case the inner AG (see Sect. 4.2). Regardless, these data support the bottom-up explanation of Whitney (2015) that posited reduced surface nutrient concentrations as a driver of reduced primary production and chlorophyll concentrations during the warm blob.

We can further observe this impact of the 2014–2015 marine heat wave on nitrate and chlorophyll concentrations using 2007–2020 summer cruise data (June–September) from the Canadian Line P program, which sampled from the coast of British Columbia to OSP (yellow dots, Fig. 1). Figure 4 shows a strong signal during the 2014–2015 warm blob along Line P, characterized by higher SSTs ($+2.5^{\circ}\text{C}$) and lower sea surface salinity (SSS; $\sim 0.2 \text{ PSU}$, practical salinity unit) between 130 and 140°W (Fig. 4). During this period, observed chlorophyll data reached concentrations below 0.3 mg m^{-3} (Fig. 4g) while nitrate concentrations are near zero west of P4 (P4–P20, Fig. 4a). We sampled the model results at Line P stations and found similar results, including SST ($+2^{\circ}\text{C}$) and salinity (-0.1 PSU) anomalies during the warm blob, and, despite a model bias toward lower climatological surface nitrate in this region (Fig. 2), the nitrate anomaly associated with the marine heat wave is still well simulated ($-2 \mu\text{M}$, Fig. 4b). The observed chlorophyll anomaly is difficult to characterize due to the patchiness of the chlorophyll field; however, the simulated chlorophyll in the model strongly suggests a decline ($<0.3 \text{ mg m}^{-3}$) during the 2014–2015 period.

3.2 Northward expansion of nitrate-depleted region in response to marine heat waves

The northeast Pacific is characterized by three regions: the nitrate-rich HNLC AG, the nitrate-depleted subtropical gyre and the NPTZ region in between. Climatologically, WOA

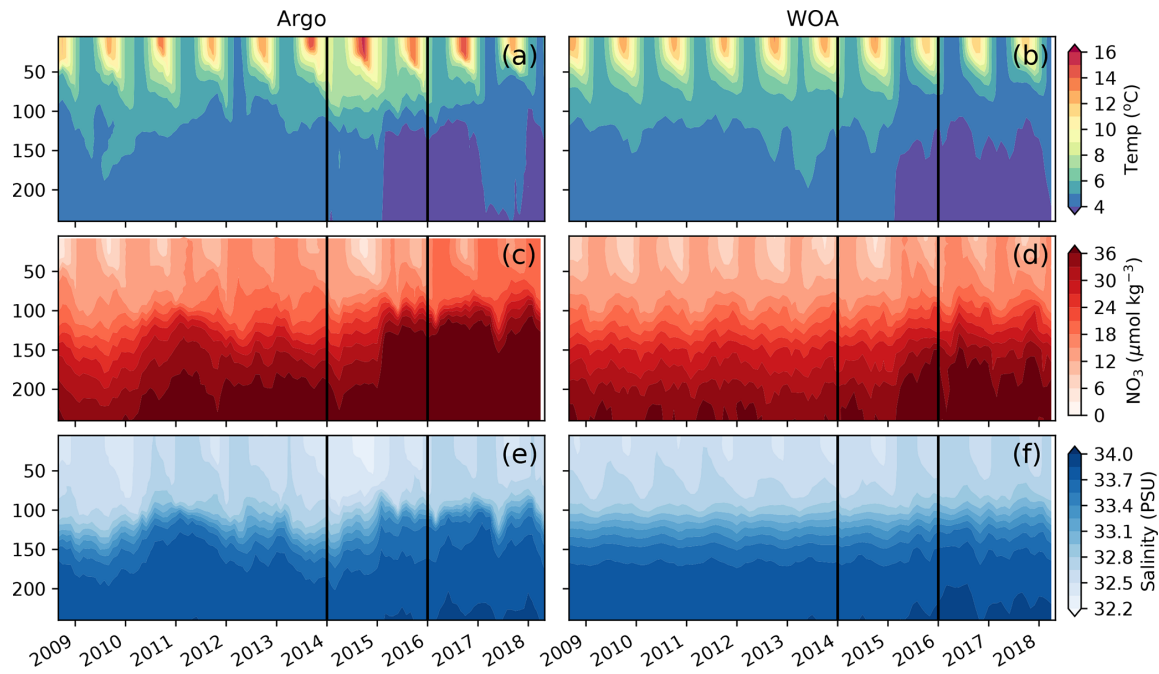


Figure 3. Comparison of observations from BGC-Argo floats shown in Fig. 2 (**a, c, e**) and sampled along their trajectories in MOM6-COBALT (**b, d, f**) for temperature (**a, b**), nitrate concentration (**c, d**) and salinity (**e, f**). The warm blob period (January 2014 to December 2015) is delimited by vertical black lines.

observations show that in winter, the nitrate-depleted region (identified here with surface $\text{NO}_3 < 2 \mu\text{M}$) extends from $\sim 35^\circ \text{N}$ on the western side of the region to $\sim 45^\circ \text{N}$ in the east near the North American coast (Fig. 5a, blue line). By the end of summer (September, green line), biological consumption has expanded the nitrate-depleted region, shifting the $2 \mu\text{M}$ contour by about 2 to 5° northward between 180° and 140°W and by about 10° east of 135°W and along the North American coast. This seasonal displacement of the nitrate front is also captured in the MOM6-COBALT climatology, with an $\sim 8^\circ$ northward shift in the western region and a similar 10° northward shift along the North American coast (Fig. 5b). The large-scale north–south nitrate gradient is, however, more intense in the model, with an approximately $-2 \mu\text{M}$ annual mean nitrate bias in the transition zone and a $+2 \mu\text{M}$ bias in the northwest AG (Fig. S1). Here we combine in situ observations with the results of the MOM6-COBALT ocean biogeochemical model and show that these warm events also systematically expand the spatial extent of nitrate depletion northward.

Examining the nine warm events (1962, 1963, 1965, 1990, 1991, 2005, 2014, 2015, 2019), we find that there is generally an expansion of the nitrate-depleted region northward into the NPTZ during warm events (Fig. 5b). Compared to the climatological $2 \mu\text{M}$ nitrate contour (solid lines), the $2 \mu\text{M}$ nitrate contour during marine heat waves (thin dashed lines) is located ~ 2 further north on average in February and ~ 1 north on average in September (Fig. 5b), with the model

suggesting that the nitrate contour shift is most consistent in the NPTZ. The WOA does not provide interannual information that we can use to evaluate the response to marine heat waves, but we can use observations from the sampling program at Line P (yellow dots), which intersects the $2 \mu\text{M}$ nitrate contour (i.e., transition between the nitrate-depleted and the nitrate-replete regions) in summer to examine its response to the 2014–2015 event.

The Line P program's June and August cruises sample three regimes (Fig. 4): the highly variable but generally nutrient-rich near-shore region ($>10 \mu\text{M}$ at $\sim 125^\circ \text{W}$), followed by the seasonally nitrate-depleted region that extends to roughly 130°W , before reaching the third region characterized by moderate to high nitrate concentrations ($>5 \mu\text{M}$) in the iron-limited AG. Ship-based Line P observations show that the high nitrate concentrations along the coast and in the AG are co-located with colder sea surface temperatures (SST $< 12^\circ \text{C}$) and higher chlorophyll concentrations ($>0.5 \text{ mg m}^{-3}$) in comparison to those observed in the nutrient-depleted region (Fig. 4a). There is a gradient in salinity across the region, with the highest salinity in the west near OSP ($\sim 32.4 \text{ PSU}$) and fresher water near shore in the east ($<32 \text{ PSU}$, Fig. 4c). These observed patterns are replicated in the MOM6-COBALT model, including the east–west contrasts in surface nitrate, SST, SSS, and chlorophyll between the coastal region, the nitrate-depleted region and the subpolar gyre (Fig. 4). However, we note that the modeled surface nitrate concentration is generally lower in com-

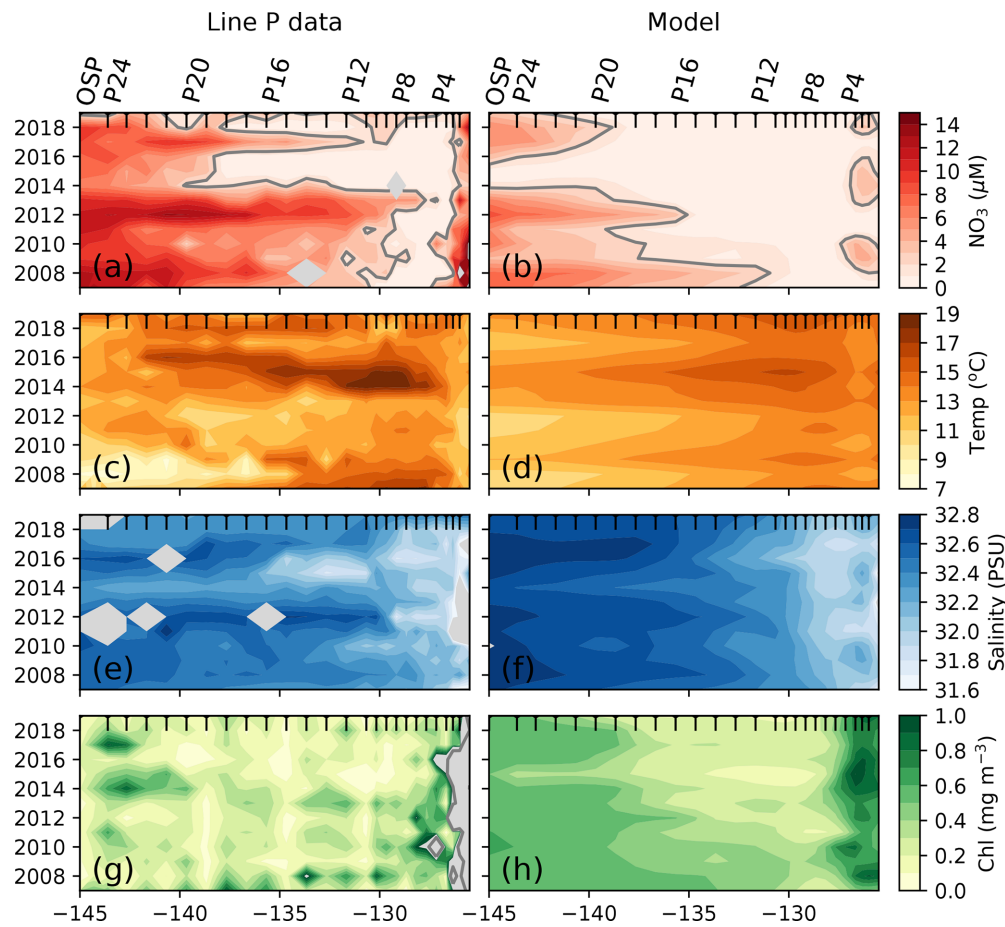


Figure 4. Impact of the 2014–2015 warm blob along Line P. **(a)** Surface nitrate concentration averaged across summer cruises (generally one in June and one in August) along Line P stations P1–P26 (OSP). **(b)** Same as panel **(a)** but sampled in the model at the station locations and averaged from June through August. The 2 μM nitrate contour is shown as a solid gray line. Other panels are the same as panels **(a)** and **(b)** but for observed and modeled sea surface temperature **(c, d)**, sea surface salinity **(e, f)**, and surface chlorophyll **(g, h)**. Gray shading indicates lack of data. Black x-axis ticks indicate station positions. See Fig. 1 for Line P station map.

parison to the Line P data, with maximum values rarely exceeding 8 μM versus 15 μM in the observations (Fig. 3a–b), consistent with the annual mean nitrate bias mentioned above.

The Line P data support the model result and show an expansion of the nitrate-depleted region during the 2014–2015 warm blob (Fig. 4), leading to a westward shift of the 2 μM contour to 140° W in 2014 (vs. a location of ~130° W in the other years). In the model, this westward shift of the nitrate contour is overestimated, extending past 140° W. However, in both the observations and model this implies that nitrate becomes depleted inside the climatological boundary of the HNLC AG. The HNLC region can therefore be considered to contract while the nitrate-depleted region expands.

3.3 Reduced ecosystem production and export in NPTZ

To understand the biological impacts of marine heat waves, we examine the composite of the nine simulated warm events. As expected from observations (Whitney, 2015; Le et al., 2019), the model simulates the greatest biological anomalies in the NPTZ, including a negative chlorophyll anomaly (-0.03 mg m^{-3} , $p < 0.05$, Fig. 6a) comparable with satellite observations (Fig. 1e). This chlorophyll anomaly is spatially co-located with a shallow winter mixed layer anomaly (-10 m , $p < 0.05$, Fig. 6b) that reduced winter surface nitrate ($-2 \mu\text{M}$, $p < 0.05$, Fig. 6c) but has little effect on winter iron concentrations (-0.1 nM , $p > 0.05$, Fig. 6d). The low winter supply of nutrients during these events inhibits the annual production of both large (-8 mmol C m^{-2} Fig. 6e) and small (-6 mmol C m^{-2} Fig. 6f) phytoplankton inside the NPTZ ($p < 0.05$ for both). These negative anomalies in phytoplankton production propagate through the food web, lead-

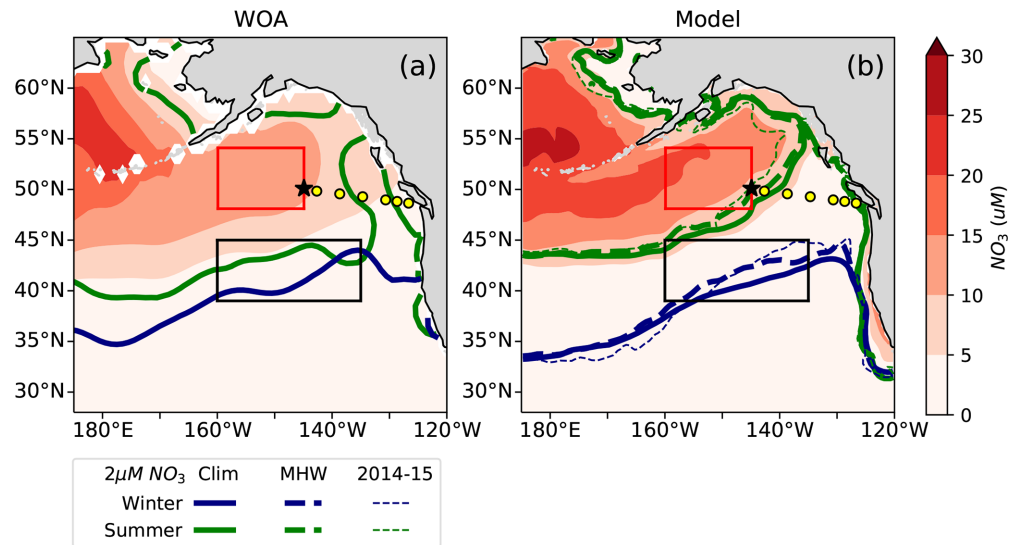


Figure 5. Annual mean surface nitrate concentrations in (a) World Ocean Atlas observations (WOA, Boyer, 2018) and (b) the MOM6-COBALT model. The seasonal location of the 2 μM surface nitrate contour in February (blue) and September (green) is indicated for the climatology (solid lines) and all individual warm events (thin dashed lines). The nitrate-depleted region south of the 2 μM contour generally shifts further north in both winter and summer during warm events. The North Pacific Transition Zone (NPTZ, 39–45° N and 160–135° W) is shown as a black box and the Alaskan Gyre (AG, 48–54° N and 160–145° W) as a red box. Line P stations and OSP are shown as described in Fig. 1.

ing to a drop in simulated zooplankton production of all three size classes (small, medium and large) and thus significantly low total annual secondary production ($-1 \text{ mmol m}^{-2} \text{ d}^{-1}$, $p < 0.05$, Fig. 6g). Similarly, particle export production, which includes zooplankton egestion and phytoplankton aggregation, also exhibits a negative production anomaly concentrated in the NPTZ ($-0.5 \text{ mmol m}^{-2} \text{ d}^{-1}$, $p < 0.05$, Fig. 6h). Although the small phytoplankton and zooplankton MHW production anomalies are relatively small in magnitude and within 1 standard deviation of the model interannual variability ($< 1\sigma$, Fig. 7b), they are statistically different from the mean state (K-S test, all p values < 0.05). We note that the most substantial response in the composite was the reduction in the ratio of large to small phytoplankton production ($p \ll 0.01$), the magnitude of which exceeds the interannual standard deviation (1σ , Fig. 7b). Individually, the annual response MHW events varies from an intense signal in 1965 (e.g., phytoplankton, zooplankton and export production anomalies $> 2\sigma$) to a near-zero perturbation in 1990.

While MHWs yield negative anomalies in annual primary and secondary production in the NPTZ (Fig. 6e–h), the effect varies seasonally, following the ecosystem size-class succession. Climatologically, the NPTZ in the model is characterized by a winter supply of nutrients supporting a modest spring bloom of large phytoplankton that peaks in April ($13.5 \text{ mmol C m}^{-2} \text{ d}^{-1}$, Fig. S4e) followed by a much larger peak in small phytoplankton production in June ($47 \text{ mmol C m}^{-2} \text{ d}^{-1}$, Fig. S4f) that dominates total primary production. Seasonal chlorophyll largely follows the large

phytoplankton production due to a higher simulated Chl : C ratio for large phytoplankton (0.022 vs. 0.014) in this region (Geider et al., 1997; Stock et al., 2020). Thus, chlorophyll peaks in April ($> 0.6 \text{ mg chlorophyll m}^{-3}$) with more modest values during the small phytoplankton peak in June ($0.2 \text{ mg chlorophyll m}^{-3}$). Zooplankton production also follows a size-based progression, with medium-size zooplankton, the primary consumer of large phytoplankton, peaking first in May ($0.8 \text{ mmol m}^{-2} \text{ d}^{-1}$, Fig. S4g), followed by small zooplankton peaking in May/June ($1.4 \text{ mmol m}^{-2} \text{ d}^{-1}$) and then large zooplankton, which consume both large phytoplankton and medium zooplankton, peaking last in June ($0.2 \text{ mmol m}^{-2} \text{ d}^{-1}$, Fig. S4f).

Marine heat waves modulate this climatological progression of the ecosystem in the NPTZ (Fig. 8). The model suggests that marine heat waves promote the growth of small phytoplankton and small- to medium-sized zooplankton in early spring before declining in summer–fall (Fig. 8e, f). This enhanced growth in the model is due to the shallower mixed layer in winter and early spring (-10 m , $p < 0.05$, Fig. 8b) that relieves light limitation and spurs early small phytoplankton and subsequent zooplankton production (Fig. 8e, f) but has little impact on the spring large phytoplankton production (Fig. 8e). Iron limitation, which dominates January–April, is not significantly impacted during MHWs (Fig. 8h); however, the onset of nitrogen limitation, which occurs when the nitrogen limitation factor (dotted red line) intersects the iron limitation factor (dotted blue line), happens nearly a month earlier (early April)

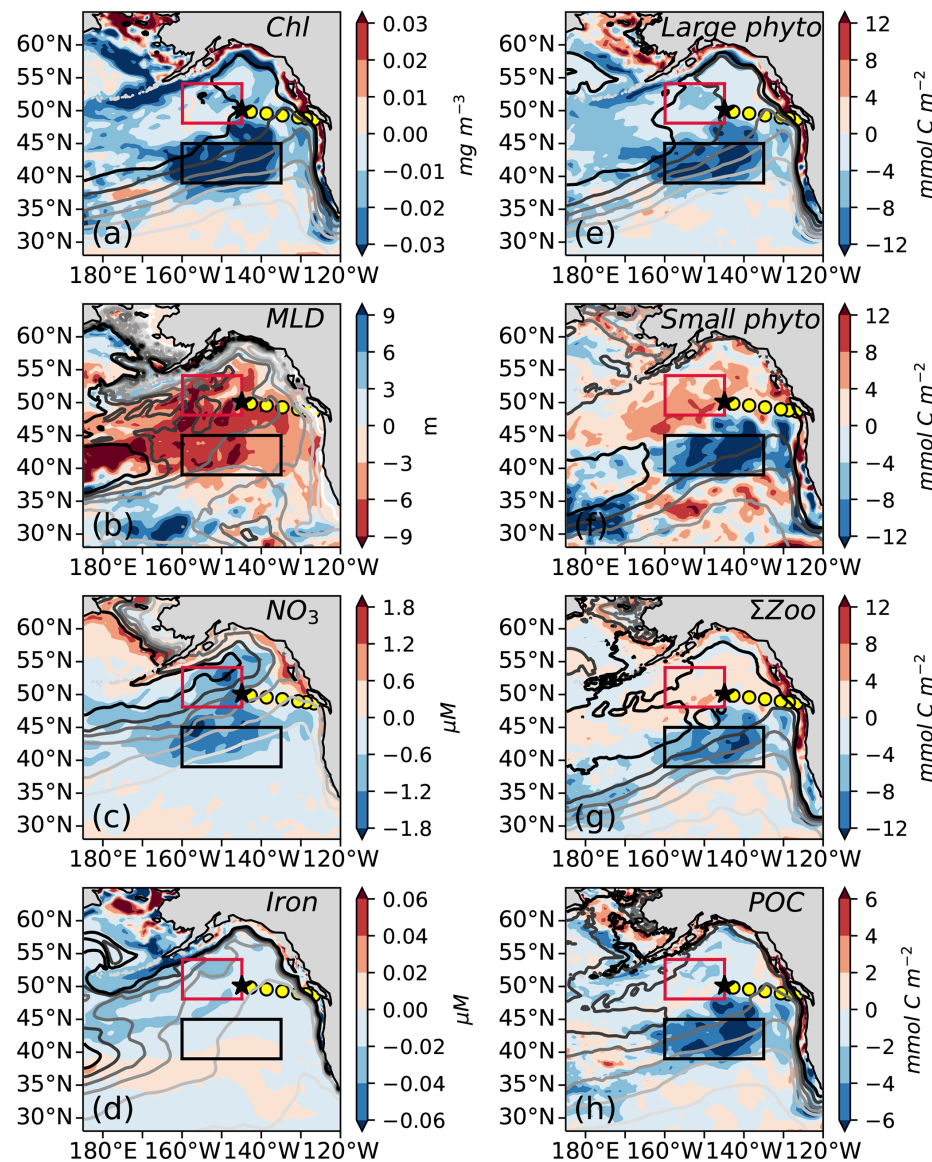


Figure 6. Modeled composite anomaly of the nine marine heat waves (1958–2020) for (a) monthly surface chlorophyll concentration; (b) winter (January–March) mixed layer depth (MLD); (c) winter surface nitrate concentration; (d) winter surface iron concentration; (e) annual depth-integrated large phytoplankton production (0–100 m); (f) annual depth-integrated small phytoplankton production (0–100 m); (g) annual depth-integrated sum of large, medium, and small zooplankton production (0–100 m); and (h) annual particulate organic carbon (POC) export at 100 m depth. Each field is overlaid with contours of the mean climatological state, with darker lines indicating higher values (see mean state maps in Fig. S3). Line P and OSP as shown in Fig. 1; boxes for AG and NPTZ are shown as described in Fig. 5.

than the climatology (solid lines, late April). Further, the nitrogen limitation factor during this period is significantly lower (-0.06 , $p < 0.05$, $\sim 25\%$ of the seasonal signal). Both size classes are limited by the reduced pool of nitrate, with negative anomalies in June ($-5 \text{ mmol m}^{-2} \text{ d}^{-1}$ for small phytoplankton; $-2 \text{ mmol m}^{-2} \text{ d}^{-1}$ for large phytoplankton; $-2.5 \text{ mmol C m}^{-2} \text{ d}^{-1}$ for total zooplankton production; Fig. 8e–f; $p < 0.05$ for all) when nitrate approaches depletion (Fig. S4).

Even with the small increase in early spring small phytoplankton production, the annual mean surface chlorophyll anomaly in the model is significantly negative (-0.03 mg m^{-3} , $p < 0.05$, Fig. 6a), in agreement with satellite observations (Fig. 1e). This slight increase in small phytoplankton production in early spring is only slightly apparent in both modeled and observed chlorophyll (red and green lines, Fig. 8a), as the impact on surface chlorophyll is small. This is again explained by the higher simulated Chl : C ratio of large phytoplankton compared to small phytoplankton

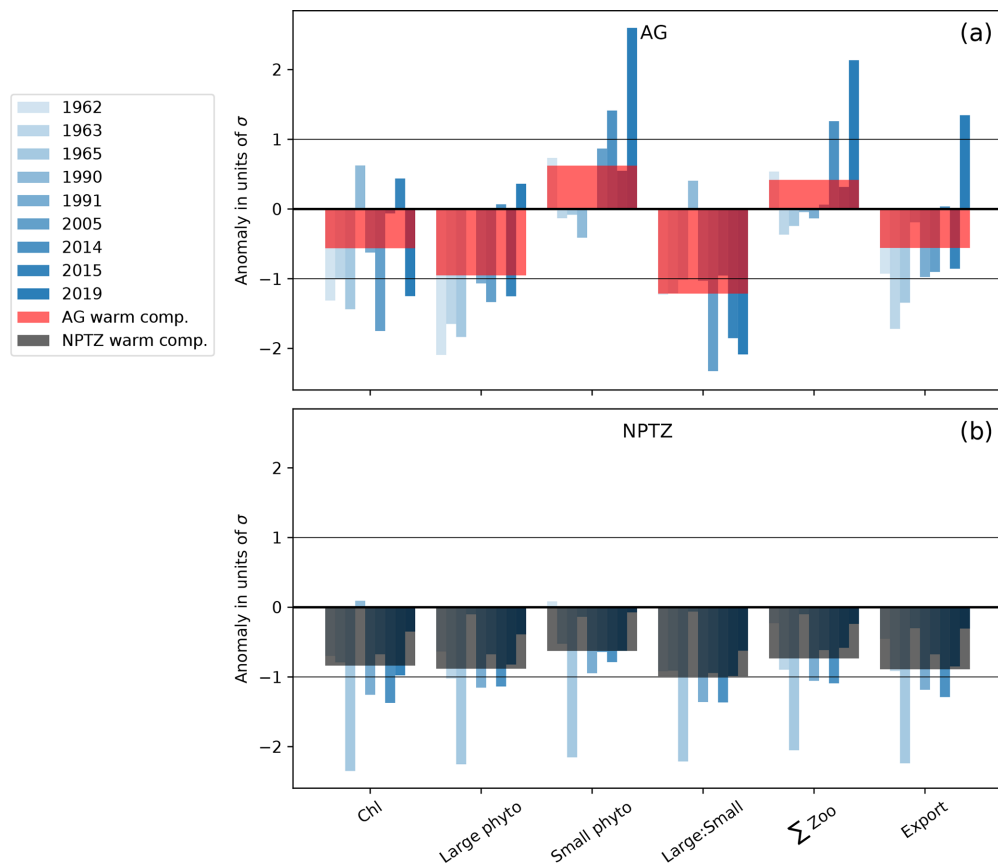


Figure 7. MHW anomalies for the 9 individual years (blue bars) and their composite (red and dark bars) in the (a) the Alaska Gyre (AG) and (b) the North Pacific Transition Zone (NPTZ). Anomalies are normalized by the regional interannual variability calculated as the standard deviation (σ) of the spatially averaged fields (i.e., values < -1 and > 1 are anomalies that exceed 1σ). Anomalies are shown for monthly Chl, as well as annually integrated large and small phytoplankton production, large-to-small-phytoplankton-production ratio (large : small), total zooplankton production (total Z), and export production.

which controls the overall response of chlorophyll to marine heat waves in this region. Indeed, a 4 % decrease in total phytoplankton production yields an 11 % decline in Chl, more closely resembling the decrease in large phytoplankton production (−12 %) than the decreased production of the more dominant but less Chl dense small phytoplankton (−2 %). This model result is consistent with the decrease in chlorophyll captured by satellite observations.

We examine the changes in phytoplankton assemblage across the NPTZ, using the normalized probability density functions of summer chlorophyll concentrations (Fig. 10). In the NPTZ (Fig. 10c, d), the distribution of phytoplankton chlorophyll concentrations for both size classes is bimodal, with one mode consistent with high chlorophyll concentrations typically found in the subpolar AG (large phytoplankton chlorophyll peak centered at 0.28 mg m^{-3} ; small phytoplankton chlorophyll peak centered at 0.25 mg m^{-3} , similar to the AG distribution shown in Fig. 10a–b) and one mode consistent with low chlorophyll concentrations typically found in the subtropical gyre (large phytoplankton chlorophyll peak centered at 0.02 mg m^{-3} ; small phytoplank-

ton chlorophyll peak centered at 0.06 mg m^{-3}). During marine heat waves, the chlorophyll distribution in the NPTZ exhibits a significant shift towards lower chlorophyll concentrations, though the shift is greater for large phytoplankton (shift of -0.05 mg m^{-3} in the mean chlorophyll concentration; $p \ll 0.01$) than for smaller phytoplankton (-0.02 mg m^{-3} in the mean chlorophyll concentration; $p \ll 0.01$). The model suggests that, climatologically, 31 % of the NPTZ area has chlorophyll concentrations $< 0.15 \text{ mg m}^{-3}$ for the large phytoplankton size class but that the proportion of the NPTZ with such low chlorophyll concentrations increases to 41 % during marine heat waves (Figs. 10, S6). Similarly, the proportion of the NPTZ with low small phytoplankton chlorophyll concentrations (chlorophyll $< 0.15 \text{ mg m}^{-3}$) increases from 28 % in the climatological state to 38 % during marine heat waves. In both cases, this shift is consistent with a decrease in the high-chlorophyll mode and an increase in the low-chlorophyll mode, and it is consistent with the decline in satellite chlorophyll observed in this region.

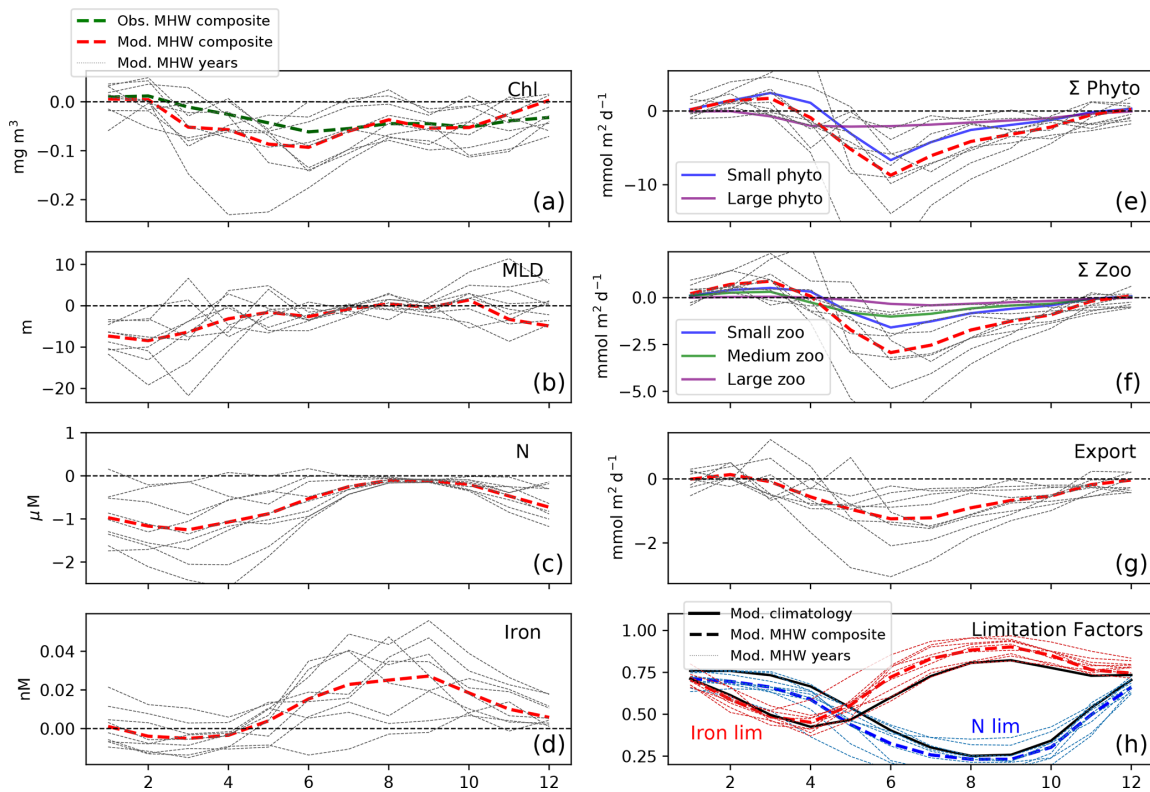


Figure 8. Seasonal response to MHWs in the NPTZ (black box shown in Fig. 5, 38–48° N and 165–135° W). Composite anomalies of the nine-event MHWs for (a) modeled surface chlorophyll (red) and observed surface chlorophyll (GlobColour, green), (b) modeled mixed layer depth, (c) surface nitrate concentration, (d) surface iron concentration, (e) depth-integrated phytoplankton production (0–100 m) with individual size classes (small in blue, large in purple), (f) depth-integrated zooplankton production (0–100 m) with individual size classes (small in blue, medium in green, large in purple), (g) particulate export production at 100 m depth, and (h) large phytoplankton nutrient limitation factors for iron (red) and nitrate (blue) for the mean climatological state (solid line) and the MHW composite (dashed lines). Across all panels, thin lines show anomalies for the 9 individual MHW years.

3.4 Modulated response in the Alaska Gyre

North of the NPTZ, in the AG, the biological impact of marine heat waves is less prominent, with the model suggesting that the decrease in annual large phytoplankton production is compensated for by an increase in small phytoplankton production. Generally, the drivers of the ecosystem response to marine heat waves in the AG resemble the response simulated in the NPTZ (see Sect. 3.3), but the balance between the light-driven increase in small phytoplankton and nutrient-driven reduction in large phytoplankton is different. Specifically, we find that shallow mixed layers reduce light limitation during marine heat waves and trigger an increase in spring small phytoplankton production ($+2 \text{ mmol C m}^{-3}$, $p < 0.05$, Fig. 9e) that exceeds the small but significant reduction in large phytoplankton production ($-1.5 \text{ mmol C m}^{-3}$, $p < 0.05$) caused by decreased nutrients early in the year (nitrate and iron, Fig. 9c, d). The negative chlorophyll anomaly that starts in the spring (April) thus is due to the decreased large phytoplankton, which have a higher simulated Chl:C (0.027), offset by the increased

small phytoplankton (Chl:C = 0.016) production anomaly. Because anomalies are insignificant later in the year for both size classes (late spring to fall), the spring signal dominates the seasonal cycle and results in a negative annually integrated chlorophyll anomaly (-0.09 mg m^{-3} , $p < 0.05$, Fig. 9a). This is consistent with the slightly negative annually integrated chlorophyll anomaly observed in satellite data (-0.02 mg m^{-3} , integrated green line), though those data exhibit a greater compensation between the large negative spring anomaly and a positive summer anomaly (green line in Fig. 9a). Unlike in the NPTZ, the annual composite anomalies in the AG (Fig. 6, red box) all fall within 1σ of the interannual variability except large phytoplankton production and the ratio of large to small phytoplankton production (Fig. 7a). For these variables, this suggests that MHWs are not the largest source of interannual variability in the region. For example, small phytoplankton production has a weak composite anomaly and exhibits a wide range of variability during MHW years: a negative or near-zero anomaly during the years 1963, 1965, 1990, and 1991 and positive anomalies during the remaining events. Despite this variabil-

ity, anomalies in large phytoplankton production are consistently more negative than anomalies in small phytoplankton production (with an exception in 1990), resulting in a decline of the large-to-small-phytoplankton-production ratio and a shift towards smaller phytoplankton similar to the NPTZ region. Indeed, in this region, the MHW impact is greatest on chlorophyll, large phytoplankton production, and especially the ratio of large to small phytoplankton, which all differ significantly ($p < 0.05$) during MHWs compared to the mean state.

The density distribution of summer chlorophyll concentrations in the AG further supports the hypothesis of a shift in the phytoplankton assemblage toward small phytoplankton (Fig. 10a–b). For each phytoplankton size class there is one main mode (large phytoplankton chlorophyll peak centered at 0.29 mg m^{-3} ; small phytoplankton chlorophyll peak centered at 0.25 mg m^{-3}). The model suggests that, climatologically, 42 % of the AG area has large phytoplankton chlorophyll concentrations $>0.4 \text{ mg m}^{-3}$ but that this proportion drops to 35 % during marine heat waves. This shift is associated with a significant reduction in the mean chlorophyll concentration of the large phytoplankton fraction in the region (-0.02 mg m^{-3} , $p < 0.05$, Fig. 10). In contrast, mean small phytoplankton chlorophyll concentrations in the AG remain virtually the same during marine heat waves. This result is supported by the observational OSP mixed-layer size-fractionated Chl *a* measurements, which also displayed atypically low large phytoplankton ($>5 \mu\text{m}$) Chl during the 2015 warm blob (0.082 mg m^{-3} , star, Fig. 10a); in contrast, small phytoplankton Chl *a* exhibits effectively no change (0.29 mg m^{-3} , star, Fig. 10b) during the same period compared to measurements from non-MHW years. These observed Chl values are lower than the simulated values and only sampled during the 2014–2015 warm event. However, they are consistent with a transition of the phytoplankton assemblage toward the smaller size class in the AG region around OSP.

4 Discussion and implications

4.1 Confinement of marine heat wave biological response to the transition zone

Previous studies have demonstrated there is a decrease in primary production in the NPTZ caused by reduced nitrate concentrations during MHWs. During the warm blob, atmospheric blocking by an atmospheric ridge (Le et al., 2019) decreased the wind-driven Ekman transport that generally carries nitrate from the northern AG southward, a process which otherwise supports up to 40 % of the new production (Ayers and Lozier, 2010). Further, nitrate concentrations were reduced by warmer upper-ocean conditions which drove a reduction in winter mixing (Amaya et al., 2021). Our results support these previous studies, with both observations

(Line P, Argo floats) and the MOM6-COBALT model indicating lower nitrate concentrations during MHW across the AG (which also has lower iron) and the NPTZ (Fig. 6c). However, we show that chlorophyll and biological production anomalies are restricted to the NPTZ only (Fig. 6a, e, f). Our results suggest that nitrate concentrations alone cannot explain the confinement of the biological anomalies to the NPTZ and that the interplay between nitrate and iron limitation, more specifically the position of the nitrogen-to-iron limitation boundary (i.e., the boundary between the northern iron-limited regime and the southern nitrate-limited regime), controls the location of the strongest MHW ecosystem anomalies.

We find that production anomalies associated with MHW are strongest in the NPTZ because the influence of reduced winter nitrate supply is greatest in the region that seasonally transitions from iron limitation in early spring to nitrate limitation in summer. In the subtropical gyre south of the NPTZ, nitrate is depleted year-round so that nitrate concentration cannot decrease and impact biological production during MHWs. In the core of the AG, north of the NPTZ, annual production is iron limited for large phytoplankton and mostly light limited for small phytoplankton; thus, changes in nitrate concentration have only a limited effect. In the NPTZ, however, nitrogen limitation starts earlier and is more intense during MHWs, with nitrogen limitation factors that are about 20 % smaller during spring and summer of MHWs than in the climatology (Fig. 8h). As a result, the NPTZ is the region where primary production is most impacted by the decrease in nitrate associated with MHWs.

4.2 Collapse of observation-based production misattributed to marine heat wave

The northward expansion of the nitrate-depleted region during MHW introduces biases in float-based estimates of net community production (NCP) and export. Floats in the vicinity of the NPTZ nitrate front can easily sample both the high-nitrate and nitrate-depleted regimes within a small spatial area ($\sim 300 \text{ km}$, Fig. 2) and over the course of a few weeks or months. Float-based estimates of NCP (Appendix A) interpret nitrate changes sampled along the float trajectories as temporal changes, leading to a misattribution of this spatial variability in nitrate to seasonal biological drawdown. In Bif et al. (2019b), NCP was calculated using the winter-to-summer difference in nitrate concentration measured by six Argo floats in the vicinity of OSP and the NPTZ between 2008 and 2018 (see details of method in the Supplement, Fig. 11). From these data, they concluded that there was a collapse in ecosystem production during the warm blob in 2015. However, this dataset only includes one float sampling the area in 2015 (float 5904125), and the trajectory of that float incidentally sampled the low-nitrate biome in winter before shifting to the higher-nitrate HNLC region in summer (brown track, Fig. 2). The sampling of these two distinct

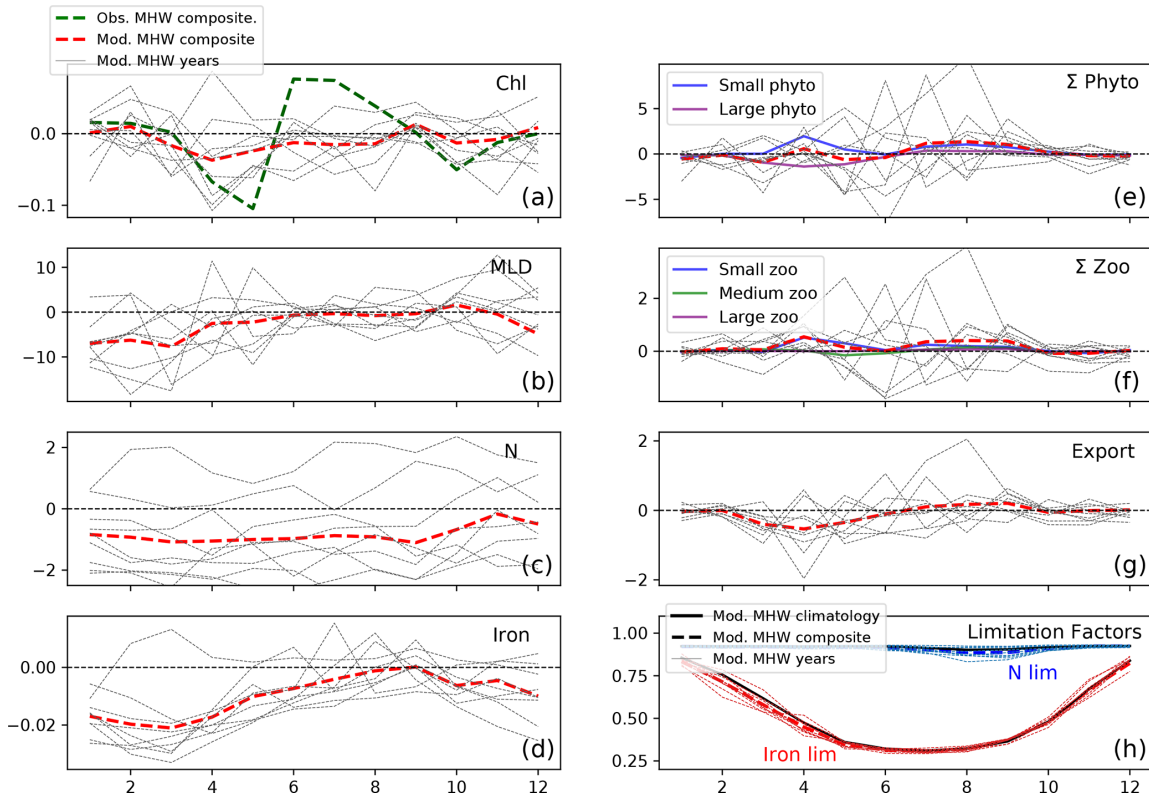


Figure 9. Response to marine heat waves in the AG (red box shown in Fig. 5, 48–54° N and 160–145° W). Same as Fig. 8 but for the AG region.

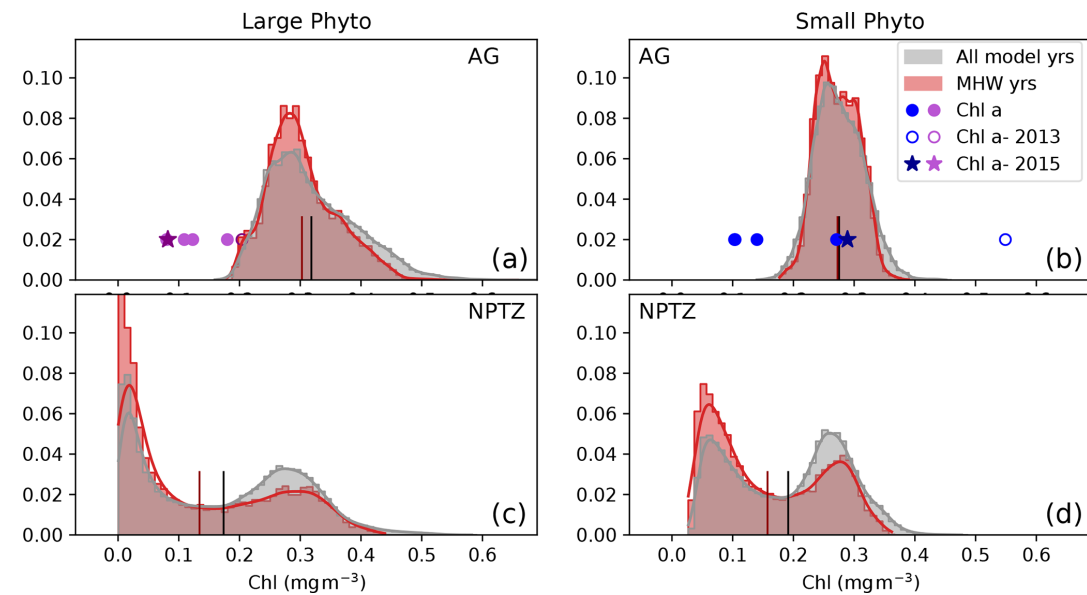


Figure 10. Observed and modeled summer (May–Aug) chlorophyll (mg m^{-3}) contained in the large (a, b) and small (c, d) phytoplankton size fraction in two regions: (a, b) Alaska Gyre and (c, d) North Pacific Transition Zone (see Fig. 5 for maps of zones). Model data are shown as normalized probability density functions for the MHW composite (red) and the climatology (gray). The mean of each is shown as a short vertical line on the x axis (red, black respectively). Chl *a* observations from the six OSP cruises in the Alaska Gyre are shown as symbols on panels (a)–(b) at $y = 0.02$; data for the non-MHW years 2000, 2001, 2008, 2013, 2015 and 2018 are shown as filled circles, while data from the anomalous 2015 warm blob and 2013 volcanic eruption are shown by a star and hollow circle respectively.

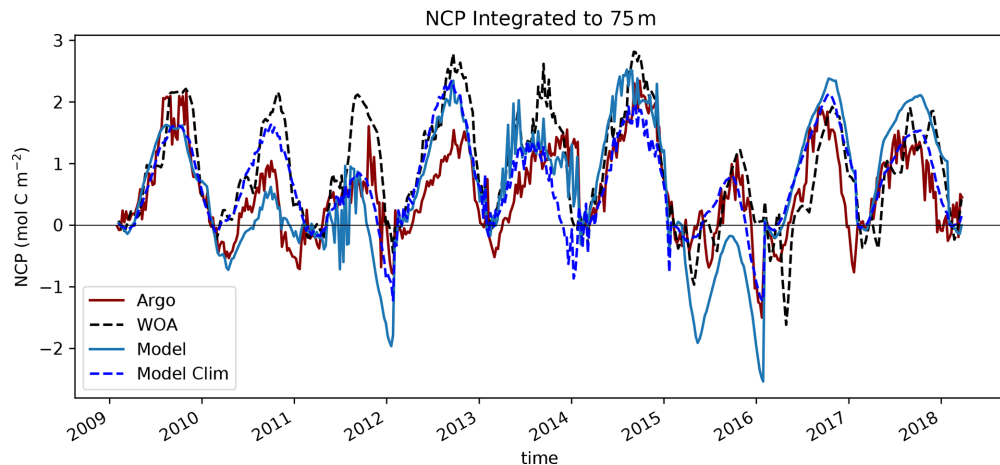


Figure 11. Net community production (NCP) calculated as nitrate drawdown from winter inventory (February) using BGC-Argo float data (dark red). These float trajectories were then used to sample the WOA climatological nitrate field (black dashed), the interannually variable MOM6-COBALT nitrate field (cobalt blue) and the MOM6-COBALT climatological nitrate field (blue dashed) to get synthetic profiles with an apparent NCP calculated similarly.

biomes is supported by the at-depth (>100 m) measurements of temperature, nitrate and salinity, which indicate that this float crossed into a new water mass in early 2015 (Fig. 3). As a result, the winter-to-summer change in nitrate along the float was artificially small and the NCP calculation biased low in 2015.

We quantified the effect of the float shifting from the NPTZ to the AG on the NCP estimate by recomputing the NCP along the same float trajectories (latitude, longitude and time) but sampling three different nitrate fields to create synthetic profiles. We thus obtain three other NCP estimates using nitrate from the climatological World Ocean Atlas (black dashed) and from the model climatological (blue dashed) and interannual (solid blue) fields that can be compared to the observed Argo-based NCP estimate (red dashed, Fig. 11). Note that for climatological profiles, only the month and day are used to sample the fields, while for the interannual field the year is also used. We find that most (>70 %) of the NCP reduction derived from these floats can be explained by sampling the climatological nitrate field and that the apparent ecosystem collapse in 2015 is in fact a feature of the float trajectory that samples across the nitrate north–south gradient (WOA vs. Argo). We performed a similar analysis using the MOM6-COBALT model, first sampling the model climatological nitrate field, and found the same result: the sampling trajectory of the float leads to an artificial NCP collapse in 2015 compared to other years that did not sample across this gradient. When considering model interannual variability and hence the effect of the marine heat wave, we find, however, an even stronger decline in NCP in 2015, suggesting that there is an NCP change caused by the warm blob itself. The model suggests, however, that only 30 % of the decline in NCP can be attributed to the heat wave, while the re-

maining 70 % is attributable to the sampling across the NPTZ nitrate front.

4.3 Shift in phytoplankton assemblage due to contrasting size-class response

Our results suggest that during MHWs, there is a shift in the phytoplankton community toward the smaller size class across both biomes. Large phytoplankton primarily respond to changes in nitrate and iron limitation. In the NPTZ, large phytoplankton are greatly impacted, with a 13 % decrease in annual production (Figs. 6e, S4e) caused by stronger nutrient limitation during MHWs (iron from January–April and then nitrate from June–December, Fig. 8h). In contrast, small phytoplankton in both regimes respond to both reduced light limitation (in spring) and enhanced nutrient limitation (in summer). Inside the NPTZ, where nitrogen limitation is strongest, small phytoplankton production increases in spring but is inhibited through summer until the mixed layer deepens in fall, resulting in a modest 4 % decrease in annual small phytoplankton production. While the changes in the size-specific production anomalies are both within 1σ of the regional interannual variability, there is a systematically greater decrease in large phytoplankton production that results in a large decrease in the ratio of large to small phytoplankton production (decrease of the order of -1σ , Fig. 7b).

In the AG, the annual anomaly in large phytoplankton production is small (-2%), driven by low production in spring when the iron supply is decreased (Fig. 9e). This is likely because the reduced winds that were shown to reduce nitrate supply during MHWs (Whitney, 2015; Le et al., 2019) also impacted the iron supply. Unlike nitrate, however, iron returns to near-climatological levels by summer (Fig. 9d), which suggests that the sources of iron are decoupled from

nitrate through the latter half of the year. As in the NPTZ, the spring small phytoplankton response is positive due to shallower mixed layers; however, in the nitrate-rich AG there is no summertime nutrient limitation of small phytoplankton and thus annual production is increased (+2 %, Figs. 6f, S5f). This contrasting response between the two size classes leads to a sizeable decrease in the large-to-small-phytoplankton-production ratio (decrease of the order of -1.2σ , Fig. 7a).

Across both regions, this shift implies that during MHWs, there is a reduced proportion of large phytoplankton such as diatoms and dinoflagellates versus greater proportions of smaller groups such as cyanobacteria and nanoflagellates. Evidence of this shift has been observed in the AG during the warm blob (Peña et al., 2019), which found higher concentrations of cyanobacteria in the nitrate-depleted region of Line P. Further, the data presented in this paper show higher Chl *a* concentrations in the smaller size classes at OSP (Sect. 3.3, 3.4). However, our work suggests this shift is more widespread, impacting both the AG and the NPTZ. Because diatoms and other large phytoplankton are known to support more productive food webs and more efficient biological carbon pumps (Boyd and Harrison, 1999), their decrease would likely substantially affect the marine ecosystem structure and reduce carbon export potential. This, in turn, increases mortality risks for certain species, may promote geographical redistributions of fisheries, and can create challenging social and political environments stemming from the associated economic impacts (Frölicher and Laufkötter, 2018). In the future, we should anticipate these ecosystem shifts as MHWs are expected to recur (Xu et al., 2021) and the atmospheric pressure systems associated with extreme events will increase in frequency (Giamalaki et al., 2021).

Appendix A: Argo NCP calculation

To calculate NCP, it is assumed that new production is fueled by nitrate supplied from the deep ocean during winter mixing (Dugdale and Goering, 1967). Thus, the temporal change in nitrate stock from the winter, i.e., when the mixed layer is deepest, to a given date must be due to net community production. This temporal change in nitrate is integrated over the top 75 m as follows:

$$\text{NCP} = r_{\text{C:N}} \int_0^{75} \text{NO}_3_{\text{winter}} - \text{NO}_3 dz, \quad (\text{A1})$$

where $r_{\text{C:N}}$ is the Redfield ratio of carbon to nitrogen. This calculation assumes all changes in nitrate are due to NCP, ignoring potential lateral and vertical contributions from physical transport. An integration depth of 75 m is selected to remain above the nitracline to limit the influence of transport, so that changes in nitrate above this depth can be largely attributed to biological processes. February was selected to be the winter month for each year as the mixed layer is often maximal between January and March; this simplification

allows for a continuous time series to be calculated from February of each year. These choices are consistent with the previous study of Bif et al. (2019b).

Code availability. The MOM6 source code is publicly available at https://github.com/NOAA-GFDL/MOM6-examples/tree/dev/gfdl/ice_ocean_SIS2/OM4_05 (Adcroft, 2022).

Data availability. The model data used in this study are publicly available on Zenodo at <https://doi.org/10.5281/zenodo.7392414> (Wyatt, 2022).

Supplement. The supplement related to this article is available online at: <https://doi.org/10.5194/bg-19-5689-2022-supplement>.

Author contributions. AMW and LR performed the model simulation and data analysis. AM provided OSP Chl *a* measurements. AMW and LR prepared the manuscript with contributions from AM.

Competing interests. The contact author has declared that none of the authors has any competing interests.

Disclaimer. Publisher's note: Copernicus Publications remains neutral with regard to jurisdictional claims in published maps and institutional affiliations.

Acknowledgements. The authors thank David Luet and Enhui Liao for their help and technical support in developing and running the MOM6-COBALT ocean simulation used in this study. The authors also thank the Geophysical Fluid Dynamical Laboratory and the MOM6 ocean modeling team for developing, maintaining and making the MOM6 ocean model publicly available on GitHub (<https://github.com/NOAA-GFDL/MOM6-examples>, last access: 18 January 2022).

Financial support. This research has been supported by the NASA ROSES 2018 EXPORTS (award nos. 80NSSC17K0555 and 80NSSC17K0552), the National Science Foundation (NSF) project Eddy Effects on the Biological Carbon Pump (award no. 2023108), the Sloan Foundation, and the NSF Graduate Research Fellowship Program (NSF-GRFP). Funding that enabled Adrian Marchetti's participation on the Line P cruise in 2015 was provided by the NSF (award no. OCE1334935).

Review statement. This paper was edited by Koji Suzuki and reviewed by two anonymous referees.

References

- Aldcroft, A.: MOM6: Document units in 9 vertical param modules, GitHub [code], https://github.com/NOAA-GFDL/MOM6-examples/tree/dev/gfdl/ice_ocean_SIS2/OM4_05, last access: 9 December 2022.
- Aldcroft, A., Anderson, W., Balaji, V., Blanton, C., Bushuk, M., Dufour, C. O., Dunne, J. P., Griffies, S. M., Hallberg, R., Harrison, M. J., Held, I. M., Jansen, M. F., John, J. G., Krasting, J. P., Langenhorst, A. R., Legg, S., Liang, Z., McHugh, C., Radhakrishnan, A., Reichl, B. G., Rosati, T., Samuels, B. L., Shao, A., Stouffer, R., Winton, M., Wittenberg, A. T., Xiang, B., Zadeh, N., and Zhang, R.: The GFDL Global Ocean and Sea Ice Model OM4.0: Model Description and Simulation Features, *J. Adv. Model. Earth Syst.*, 11, 3167–3211, <https://doi.org/10.1029/2019MS001726>, 2019.
- Amaya, D. J., Alexander, M. A., Capotondi, A., Deser, C., Karinauskas, K. B., Miller, A. J., and Mantua, N. J.: Are Long-Term Changes in Mixed Layer Depth Influencing North Pacific Marine Heatwaves?, *Bull. Am. Meteorol. Soc.*, 102, S59–S66, <https://doi.org/10.1175/BAMS-D-20-0144.1>, 2021.
- Ayers, J. M. and Lozier, M. S.: Physical controls on the seasonal migration of the North Pacific transition zone chlorophyll front, *J. Geophys. Res.-Ocean.*, 115, C05001, <https://doi.org/10.1029/2009JC005596>, 2010.
- Bif, M. B. and Hansell, D. A.: Seasonality of Dissolved Organic Carbon in the Upper Northeast Pacific Ocean, *Global Biogeochem. Cy.*, 33, 526–539, <https://doi.org/10.1029/2018GB006152>, 2019a.
- Bif, M. B., Siqueira, L., and Hansell, D. A.: Warm Events Induce Loss of Resilience in Organic Carbon Production in the Northeast Pacific Ocean, *Global Biogeochem. Cy.*, 33, <https://doi.org/10.1029/2019GB006327>, 2019b.
- Bograd, S. J., Foley, D. G., Schwing, F. B., Wilson, C., Laurs, R. M., Polovina, J. J., Howell, E. A., and Brainard, R. E.: On the seasonal and interannual migrations of the transition zone chlorophyll front, *Geophys. Res. Lett.*, 31, L17204, <https://doi.org/10.1029/2004GL020637>, 2004.
- Bond, N. A., Cronin, M. F., Freeland, H., and Mantua, N.: Causes and impacts of the 2014 warm anomaly in the NE Pacific, *Geophys. Res. Lett.*, 42, 3414–3420, <https://doi.org/10.1002/2015GL063306>, 2015.
- Boyd, P. and Harrison, P. J.: Phytoplankton dynamics in the NE subarctic Pacific, *Deep-Sea Res. Pt. II*, 46, 2405–2432, [https://doi.org/10.1016/S0967-0645\(99\)00069-7](https://doi.org/10.1016/S0967-0645(99)00069-7), 1999.
- Boyd, P. W., Law, C. S., Wong, C. S., Nojiri, Y., Tsuda, A., Levasseur, M., Takeda, S., Rivkin, R., Harrison, P. J., Strzepek, R., Gower, J., McKay, R. M., Abraham, E., Arychuk, M., Barwell-Clarke, J., Crawford, W., Crawford, D., Hale, M., Harada, K., Johnson, K., Kiyosawa, H., Kudo, I., Marchetti, A., Miller, W., Needoba, J., Nishioka, J., Ogawa, H., Page, J., Robert, M., Saito, H., Sastri, A., Sherry, N., Soutar, T., Sutherland, N., Taira, Y., Whitney, F., Wong, S.-K. E., and Yoshimura, T.: The decline and fate of an iron-induced subarctic phytoplankton bloom, *Nature*, 428, 549–553, <https://doi.org/10.1038/nature02437>, 2004.
- Boyer, T. P., Antonov, J. I., Baranova, O. K., Garcia, H. E., Johnson, D. R., Mishonov, A. V., O'Brien, T. D., Seidov, D., I. (Igor), S., Zweng, M. M., Paver, C. R., Locarnini, R. A., Reagan, J. R., Coleman, C., and Grodsky, A.: World ocean database 2013, <https://doi.org/10.7289/V5NZ85MT>, 2013.
- Brand, L. E., Guillard, R. R. L., and Murphy, L. S.: A method for the rapid and precise determination of acclimated phytoplankton reproduction rates, *J. Plank. Res.*, 3, 193–201, <https://doi.org/10.1093/plankt/3.2.193>, 1981.
- Buesseler, K. O.: The decoupling of production and particulate export in the surface ocean, *Global Biogeochem. Cy.*, 12, 297–310, <https://doi.org/10.1029/97GB03366>, 1998.
- Chai, F., Jiang, M., Barber, R. T., Dugdale, R. C., and Chao, Y.: Interdecadal Variation of the Transition Zone Chlorophyll Front: A Physical-Biological Model Simulation between 1960 and 1990, *J. Oceanogr.*, 59, 461–475, 2003.
- Di Lorenzo, E. and Mantua, N.: Multi-year persistence of the 2014/15 North Pacific marine heatwave, *Nat. Clim. Change*, 6, 1042–1047, <https://doi.org/10.1038/nclimate3082>, 2016.
- Droop, M. R.: 25 Years of Algal Growth Kinetics A Personal View, *Bot. Mar.*, 23, 99–112, <https://doi.org/10.1515/botm.1983.26.3.99>, 1983.
- Dugdale, R. C. and Goering, J. J.: Uptake of New and Regenerated Forms of Nitrogen in Primary Productivity, *Limnol. Oceanogr.*, 12, 196–206, <https://doi.org/10.4319/lo.1967.12.2.0196>, 1967.
- Dunne, J. P., John, J. G., Aldcroft, A. J., Griffies, S. M., Hallberg, R. W., Shevliakova, E., Stouffer, R. J., Cooke, W., Dunne, K. A., Harrison, M. J., Krasting, J. P., Malyshev, S. L., Milly, P. C. D., Phillipps, P. J., Sentman, L. T., Samuels, B. L., Spelman, M. J., Winton, M., Wittenberg, A. T., and Zadeh, N.: GFDL's ESM2 Global Coupled Climate–Carbon Earth System Models. Part I: Physical Formulation and Baseline Simulation Characteristics, *J. Clim.*, 25, 6646–6665, <https://doi.org/10.1175/JCLI-D-11-00560.1>, 2012.
- Freeland, H. and Whitney, F.: Unusual warming in the Gulf of Alaska, *North Pacific Marine Science Organization*, 22, 51–52, 2014.
- Frölicher, T. L. and Laufkötter, C.: Emerging risks from marine heat waves, *Nat. Commun.*, 9, 650, <https://doi.org/10.1038/s41467-018-03163-6>, 2018.
- Geider, R., MacIntyre, H., and Kana, T.: Dynamic model of phytoplankton growth and acclimation: responses of the balanced growth rate and the chlorophyll a:carbon ratio to light, nutrient-limitation and temperature, *Mar. Ecol. Prog. Ser.*, 148, 187–200, <https://doi.org/10.3354/meps148187>, 1997.
- Giamalaki, K., Beaulieu, C., Henson, S. A., Martin, A. P., Kassem, H., and Faranda, D.: Future intensification of extreme Aleutian low events and their climate impacts, *Sci. Rep.*, 11, 18395, <https://doi.org/10.1038/s41598-021-97615-7>, 2021.
- Glover, D. M., Wroblewski, J. S., and McClain, C. R.: Dynamics of the transition zone in coastal zone color scanner-sensed ocean color in the North Pacific during oceanographic spring, *J. Geophys. Res.-Ocean.*, 99, 7501–7511, <https://doi.org/10.1029/93JC02144>, 1994.
- Harrison, P. J.: Station Papa Time Series: Insights into Ecosystem Dynamics, *J. Oceanogr.*, 58, 259–264, 2002.
- Huang, B., Banzon, V. F., Freeman, E., Lawrimore, J., Liu, W., Peterson, T. C., Smith, T. M., Thorne, P. W., Woodruff, S. D., and Zhang, H.-M.: Extended Reconstructed Sea Surface Temperature (ERSST), Version 4. NOAA National Centers for Environmental Information [data set], <https://doi.org/10.7289/V5KD1VVF>, 2015.
- Khatiwala, S., Tanhua, T., Mikaloff Fletcher, S., Gerber, M., Doney, S. C., Graven, H. D., Gruber, N., McKinley, G. A.,

- Murata, A., Ríos, A. F., and Sabine, C. L.: Global ocean storage of anthropogenic carbon, *Biogeosciences*, 10, 2169–2191, <https://doi.org/10.5194/bg-10-2169-2013>, 2013.
- Le, C., Wu, S., Hu, C., Beck, M. W., and Yang, X.: Phytoplankton decline in the eastern North Pacific transition zone associated with atmospheric blocking, *Glob. Change Biol.*, 25, 3485–3493, <https://doi.org/10.1111/gcb.14737>, 2019.
- Liao, E., Resplandy, L., Liu, J., and Bowman, K. W.: Amplification of the Ocean Carbon Sink During El Niños: Role of Poleward Ekman Transport and Influence on Atmospheric CO₂, *Global Biogeochem. Cy.*, 34, e2020GB006574, <https://doi.org/10.1029/2020GB006574>, 2020.
- Maritorena, S., d'Andon, O. H. F., Mangin, A., and Siegel, D. A.: Merged satellite ocean color data products using a bio-optical model: Characteristics, benefits and issues, *Remote Sens. Environ.*, 114, 1791–1804, <https://doi.org/10.1016/j.rse.2010.04.002>, 2010.
- Martin, J. H. and Fitzwater, S. E.: Iron deficiency limits phytoplankton growth in the north-east Pacific subarctic, *Nature*, 331, 341–343, <https://doi.org/10.1038/331341a0>, 1988.
- Munk, W. and Riley, G.: Absorption of nutrients by aquatic plants, *J. Mar. Res.*, 11, 121–152, 1952.
- Olsen, A., Key, R. M., van Heuven, S., Lauvset, S. K., Velo, A., Lin, X., Schirnick, C., Kozyr, A., Tanhua, T., Hoppema, M., Jutterström, S., Steinfeldt, R., Jeansson, E., Ishii, M., Pérez, F. F., and Suzuki, T.: The Global Ocean Data Analysis Project version 2 (GLODAPv2) – an internally consistent data product for the world ocean, *Earth Syst. Sci. Data*, 8, 297–323, <https://doi.org/10.5194/essd-8-297-2016>, 2016.
- Peña, M. A., Nemcek, N., and Robert, M.: Phytoplankton responses to the 2014–2016 warming anomaly in the north-east subarctic Pacific Ocean, *Limnol. Oceanogr.*, 64, 515–525, <https://doi.org/10.1002/lno.11056>, 2019.
- Plant, J. N., Johnson, K. S., Sakamoto, C. M., Jannasch, H. W., Coletti, L. J., Riser, S. C., and Swift, D. D.: Net community production at Ocean Station Papa observed with nitrate and oxygen sensors on profiling floats, *Global Biogeochem. Cy.*, 30, 859–879, <https://doi.org/10.1002/2015GB005349>, 2016.
- Polovina, J. J., Howell, E., Kobayashi, D. R., and Seki, M. P.: The transition zone chlorophyll front, a dynamic global feature defining migration and forage habitat for marine resources, *Prog. Oceanogr.*, 49, 469–483, [https://doi.org/10.1016/S0079-6611\(01\)00036-2](https://doi.org/10.1016/S0079-6611(01)00036-2), 2001.
- Seitzinger, S. P., Mayorga, E., Bouwman, A. F., Kroese, C., Beusen, A. H. W., Billen, G., Drecht, G. V., Dumont, E., Fekete, B. M., Garnier, J., and Harrison, J. A.: Global river nutrient export: A scenario analysis of past and future trends, *Global Biogeochem. Cy.*, 24, GB0A08, <https://doi.org/10.1029/2009GB003587>, 2010.
- Stock, C. A., Dunne, J. P., and John, J. G.: Global-scale carbon and energy flows through the marine planktonic food web: An analysis with a coupled physical–biological model, *Prog. Oceanogr.*, 120, 1–28, <https://doi.org/10.1016/j.pocean.2013.07.001>, 2014.
- Stock, C. A., Dunne, J. P., Fan, S., Ginoux, P., John, J., Krasting, J. P., Laufkötter, C., Paulot, F., and Zadeh, N.: Ocean Biogeochemistry in GFDL's Earth System Model 4.1 and Its Response to Increasing Atmospheric CO₂, *J. Adv. Model. Earth Syst.*, 12, e2019MS002043, <https://doi.org/10.1029/2019MS002043>, 2020.
- Suryan, R. M., Arimitsu, M. L., Coletti, H. A., Hopcroft, R. R., Lindeberg, M. R., Barbeaux, S. J., Batten, S. D., Burt, W. J., Bishop, M. A., Bodkin, J. L., Brenner, R., Campbell, R. W., Cushing, D. A., Danielson, S. L., Dorn, M. W., Drummond, B., Esler, D., Gelatt, T., Hanselman, D. H., Hatch, S. A., Haught, S., Holderied, K., Iken, K., Irons, D. B., Kettle, A. B., Kimmel, D. G., Konar, B., Kuletz, K. J., Laurel, B. J., Maniscalco, J. M., Matkin, C., McKinstry, C. A. E., Monson, D. H., Moran, J. R., Olsen, D., Palsson, W. A., Pegau, W. S., Piatt, J. F., Rogers, L. A., Rojek, N. A., Schaefer, A., Spies, I. B., Straley, J. M., Strom, S. L., Sweeney, K. L., Szymkowiak, M., Weitzman, B. P., Yasumiishi, E. M., and Zador, S. G.: Ecosystem response persists after a prolonged marine heatwave, *Sci. Rep.*, 11, 6235, <https://doi.org/10.1038/s41598-021-83818-5>, 2021.
- Tsujino, H., Urakawa, S., Nakano, H., Small, R. J., Kim, W. M., Yeager, S. G., Danabasoglu, G., Suzuki, T., Bamber, J. L., Bentzen, M., Böning, C. W., Bozec, A., Chassignet, E. P., Curchitser, E., Boeira Dias, F., Durack, P. J., Griffies, S. M., Harada, Y., Ilıcak, M., Josey, S. A., Kobayashi, C., Kobayashi, S., Komuro, Y., Large, W. G., Le Sommer, J., Marsland, S. J., Masina, S., Scheinert, M., Tomita, H., Valdivieso, M., and Yamazaki, D.: JRA-55 based surface dataset for driving ocean–sea-ice models (JRA55-do), *Ocean Model.*, 130, 79–139, <https://doi.org/10.1016/j.ocemod.2018.07.002>, 2018.
- Waythomas, C. F., Haney, M. M., Fee, D., Schneider, D. J., and Wech, A.: The 2013 eruption of Pavlof Volcano, Alaska: a spatter eruption at an ice- and snow-clad volcano, *Bull. Volcanol.*, 76, 862, <https://doi.org/10.1007/s00445-014-0862-2>, 2014.
- Whitney, F. A.: Anomalous winter winds decrease 2014 transition zone productivity in the NE Pacific, *Geophys. Res. Lett.*, 42, 428–431, <https://doi.org/10.1002/2014GL062634>, 2015.
- Wyatt, A.: MOM6-COBALTv2 model result for ecosystem response to marine heat waves (Version 1), Zenodo [data set], <https://doi.org/10.5281/zenodo.7392414>, 2022.
- Xu, T., Newman, M., Capotondi, A., and Lorenzo, E. D.: The Continuum of Northeast Pacific Marine Heatwaves and Their Relationship to the Tropical Pacific, *Geophys. Res. Lett.*, 48, 2020GL090661, <https://doi.org/10.1029/2020GL090661>, 2021.

*Look at the map. We go your way, that's about four
inches. We go my way, it's an inch and a half. You
wanna pay for the extra gas?*

—Steve Zissou

2

Quantifying spatiotemporal variability of ^{234}Th -derived estimates of the ocean biological carbon flux

2.0 ABSTRACT:

The NASA EXport Processes in the Ocean from Remote Sensing (EXPORTS) program was a large-scale campaign that sent multiple assets to two locations, the Northeast Pacific and the North Atlantic, to quantify the various processes and mechanisms associated with the ocean's biological carbon pump. At each site, one of the many diverse and high-resolution datasets collected were particle sinking fluxes derived from thorium-234 (^{234}Th), a proxy for particle sinking export. Here we examine these ^{234}Th data, characterizing the spatial and temporal variability in both regimes. In the Northeast Pacific, a region characterized by relatively low physical dynamics and a modest spring phytoplankton bloom, there was a decrease in the observed thorium flux from Aug. 2018 – Sep. 2018 that can be attributed to a seasonal decline in particle export or a spatial gradient in particle fluxes. Evidence presented here suggests that the change is likely caused by seasonal fluctuations, with fine-scale variations attributed to spatial variability. In contrast, the May 2021 eddy sampling of the North Atlantic, a region with high eddy kinetic energy and a strong seasonal bloom, reveals comparable spatial variability, indicating that the targeted sampling of a coherent eddy likely reduced spatial heterogeneity, reducing errors induced by dynamical thorium transport. While the high resolution of these datasets provided an unprecedented opportunity to characterize flux variabilities, further work is needed to examine the impact of fine-scale dynamics on ^{234}Th -derived particle fluxes.

2.1 INTRODUCTION

This chapter outlines my contributions to the analyses of three papers of which I am a co-author. The appendices contain those papers: Buesseler et al., 2020; Roca-Martí et al., 2021; and Clevenger et al., 2024. Here, I provide an overview of the context, methods, and results directly impacted by my work.

2.1.1 QUANTIFYING SINKING FLUXES IN TWO EXPORT REGIMES DURING THE NASA EXPORTS PROGRAM

The NASA EXport Processes in the Ocean from Remote Sensing (EXPORTS) program was a large-scale research campaign that supported two cruises to Ocean Station Papa (OSP, 50° N, 145° W, August 2018) in the North Pacific (Siegel et al., 2021) and the Porcupine Abyssal Plain (PAP, 48° N, 22° E, May 2021) in the North Atlantic (yellow stars, Fig 2.1; Johnson et al., 2024). Both cruises were supported by multiple ships and collected an unprecedented number of diverse and complementary datasets, including thorium-234 (^{234}Th) samples, over approximately four weeks. These cruises were designed to capture large and diverse datasets that quantified the various mechanisms of the biological carbon pump, the processes by which the surface ocean ecosystem transports organic carbon to the deep ocean (Siegel et al., 2016). With observations of primary productivity, ecosystem composition, particulate and dissolved organic detritus production, nutrient concentrations, water column dynamics, and more, these cruises provided a unique opportunity to observe and quantify the processes that control the production and fate of organic carbon detritus. In particular, this campaign produced two unprecedented, high spatial and temporal resolution ^{234}Th datasets, which can be used to estimate particle sinking fluxes.

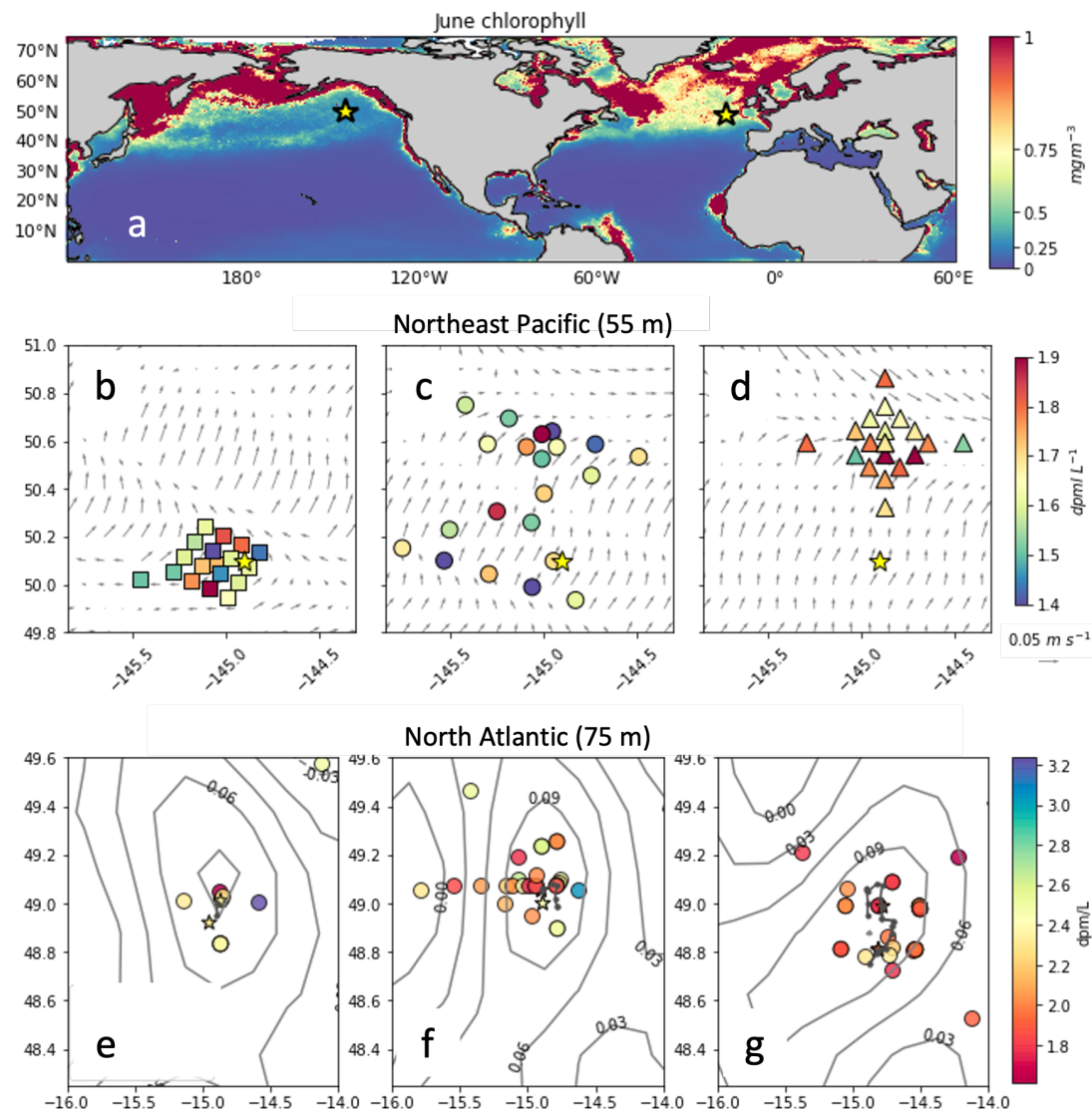


Figure 2.1: Sampling locations of NASA EXPORTS field campaigns. a) Mean June satellite chlorophyll concentration from 1997-2020 from Globcolour with locations of NASA EXPORTS field campaigns, OSP (50° N, 145° W, Aug. 2018) and PAP (48° N, 22° E, May 2021) denoted as yellow stars. b-d) Pacific cruise and e-g) Atlantic cruise sampling patterns and thorium activities for each epoch 1-3 at 55 m and 75 m respectively. Pacific epoch-mean velocity field derived from satellite altimetry. Atlantic sea surface height anomalies show eddy boundary.

The first study site was the Northeast Pacific Ocean near OSP sampled in August 2018. This region is a high nutrient, low chlorophyll region where phytoplankton production is

iron-limited, thus, a large nitrate concentration ($> 10 \text{ mmol m}^{-3}$) is always present (Martin and Fitzwater 1988). The region features low biomass seasonality with a modest spring bloom (Boyd and Harrison, 1999; Goes et al., 2004; Fassbender et al., 2016). The region is also home to several long-term datasets, including floating sediment traps (Timothy et al., 2013), drifting arrays (Wong et al., 2002), and ^{234}Th studies (Charette et al., 1999).

In contrast, the second study site, the Northeast Atlantic Ocean near the PAP in May 2021, hosts a large spring bloom dominated by fast-growing diatoms and coccolithophores (Lochte et al., 1993; Leblanc et al., 2009). This results in substantial export production of large, fast sinking particles, though zooplankton grazing and disaggregation results in a significant proportion of smaller sinking particles at depth (Giering et al., 2016). Further, this region is known to exhibit sporadic pulses of increased export activity (e.g., Lampitt et al., 1985), which led to the establishment of a long-term time series that captures the temporal variability of the region (Hartman et al., 2021).

Across both regions, disentangling spatial and temporal changes in tracer concentrations (e.g. ^{234}Th) is a challenge that we address here. Relying on contemporaneously obtained cruise datasets, regional flux characterizations from past literature, and the sub-sampling of two general circulation models we provide context from which to untangle the cruise data to characterize the sinking fluxes of the two regimes. We quantify the spatial gradients observed in situ and credit the high-resolution sampling with enabling the discernment of multiple scales of variability. This work helps refine our estimates and interpretation of particle sinking fluxes, one mechanism that controls the strength of the biological carbon pump as part of the NASA EXPORTS program objectives.

2.1.2 ESTIMATING PARTICULATE SINKING FLUX FROM ^{234}Th DYNAMICS

The radioactive pairing, ^{234}Th and uranium-238 (^{238}U) can be used to estimate in situ particle fluxes using a ^{234}Th balance equation that assumes that the disequilibrium between the particle-reactive ^{234}Th and its conservative parent ^{238}U must be due to a flux of organic matter on which ^{234}Th is adsorbed. In the simplest case, it is assumed that the only flux leaving the system is that which is sinking and so the observed difference between ^{234}Th and uranium can be integrated in depth and equated to a sinking particle flux (Eq. 2.1).

This 1D steady-state (1D-SS) flux estimate can be expressed as:

$$E_{SS} = \int_z \lambda (A_U - A_{Th}) dz \quad (2.1)$$

where E_{SS} is the 1D-SS flux of sinking particles at a depth, z . A_U and A_{Th} are the observed radioactivities of ^{238}U and ^{234}Th , respectively and $\lambda = 0.02876 \text{ d}^{-1}$ is the radioactive decay constant set by the half-life of ^{234}Th (24.1 days).

However, a full accounting of the ^{234}Th tracer equation would also include a term that accounts for changes in ^{234}Th due to physical dynamics () and would not assume a steady state (Eq. 2.2).

$$\frac{dA_{Th}}{dt} = \int_z \lambda (A_U - A_{Th}) - E + D \quad (2.2)$$

Here, the time tendency of ^{234}Th , dA_{Th}/dt , and the physical transport of ^{234}Th through advection and diffusion both horizontally and vertically, D , are both non-zero. When a steady state cannot be assumed, i.e., during or shortly after a phytoplankton bloom, equation 2.2 can be used to get a 1D non-steady state (1D-NSS) sinking flux estimate by solving

the first order linear equation:

$$E_{NSS} = \int_z \lambda \times \frac{1 - e^{-\lambda \Delta t} A_U + A_{Th_{t_0}} e^{-\lambda \Delta t} - A_{Th_{t_f}}}{(1 - e^{-\lambda \Delta t})} dz \quad (2.3)$$

This formulation, however, requires repeat sampling of the same water mass in time to get starting radioactivity ($A_{Th_{t_0}}$) and ending radioactivity ($A_{Th_{t_f}}$) over a time interval ($\Delta t = t_f - t_0$).

However, both the 1D-SS and 1D-NSS approaches neglect the physical transport of ^{234}Th (D) that may impact the ^{234}Th - ^{238}U disequilibrium, due to the difficulty in quantifying the magnitude of thorium advection and mixing. Thus, in regions where turbulent dynamics are significant, e.g. the North Atlantic, ^{234}Th -derived estimates of particle fluxes are associated with high uncertainties.

2.1.3 AUTHOR'S CONTRIBUTION TO PUBLISHED WORKS

As a member of the 2018 EXPORTS cruise to the North Pacific, I participated in the initial data collection, processing, and validation of ^{234}Th radioactivity samples. Post-processing of these data, including quantification and removal of background radiation, was done by the team at Woods Hole Oceanographic Institution (WHOI) approximately six months after initial data collection. The 1D-SS and 1D-NSS ^{234}Th fluxes derived from these data followed the methodology outlined in Buesseler et al. (2020) and were cooperatively performed and verified by both the WHOI and Princeton groups. The analysis of physical transport was primarily done at Princeton. Carbon and other bio-element fluxes were derived from C:Th ratios obtained from the cruise pump and sediment trap data led by the WHOI and University of Maine teams, with some analysis done by me at Princeton.

In the following I break down the Methods and Results sections into two parts each, addressing the Northeast Pacific and North Atlantic separately, then in the Discussion, I compare and contrast the variability observed in both. For both regions, I provide estimates of dynamical thorium transport and quantify the impact on 1D ^{234}Th -derived estimates. Then I demonstrate the difficulty in disentangling seasonal variation and mesoscale spatial variability in the Northeast Pacific due to high fine-scale spatial variability of the data. In contrast, the North Atlantic data exhibit a strong seasonal signal and relatively low spatial variability thanks to the Lagrangian sampling inside an eddy.

2.2 METHODS

THE NORTHEAST PACIFIC OCEAN

2.2.1 ^{234}Th -DERIVED PARTICLE FLUXES IN THE NORTHEAST PACIFIC

The EXPORTS cruise to the Northeast Pacific consisted of two ships, the R/V Revelle and the R/V Sally Ride, the latter was the collection platform for ^{234}Th data. The sampling was conducted following a Lagrangian float from August 9 to September 13, 2018, released near 100 m in depth, where the photosynthetic active radiation (PAR) penetration reached 0.1% (Siegel et al., 2020). While the R/V Revelle followed the float directly, the R/V Sally ride sampled in three 8-day grids termed “epochs,” the pattern of which can be seen in Figure 2.1b-d. At each sampling site, a conductivity, temperature, and depth (CTD) cast was performed, providing 2 L of water for ship-board ^{234}Th analysis.

The total ^{234}Th of 950+ samples from 61 stations was precipitated onto 25 mm diameter quartz microfiber filters (QMA) and dried. The radioactivity of the dried filters was

then counted at least twice on ship-board low-level Risø β counters, with extreme outliers removed. Corrections for precipitate efficiency and background radiation were performed post-cruise at Woods Hole Oceanographic Institute (WHOI). ^{234}Th radioactivity was averaged per epoch, with final profiles shown in Figure 2.2, for further details, see Buessler et al., 2020.

To convert to particulate organic carbon fluxes, carbon- ^{234}Th ratios were obtained from six battery-powered in situ pumps (McLane Industries) with attached filter systems, deployed four times per epoch for a total of 12 casts, for 4-5 hours per deployment. ^{234}Th activities of these filters were processed comparably to those from the filtered CTD samples, with particulate carbon derived from high-temperature combustion at the WHOI Nutrient Analytical Facility with the inorganic component determined by closed-system digestion with phosphoric acid by coulometry (see Roca-Martí et al., 2021 for full details).

2.2.2 ESTIMATING PHYSICAL TRANSPORT OF ^{234}Th FROM IN-SITU OBSERVATIONS IN THE NORTHEAST PACIFIC

To estimate the physical ^{234}Th transport (in Eq. 2.2), the horizontal advection, vertical advection, and vertical diffusion can be calculated.

$$D = \int_z \left(\mathbf{u} \frac{\Delta A_{Tb}}{\Delta \mathbf{x}} + \mathbf{w} \frac{\Delta A_{Tb}}{\Delta z} + \frac{\Delta k \Delta A_{Tb}}{\Delta z^2} \right) \quad (2.4)$$

where horizontal advection was estimated using an average mixed layer (< 25 m) horizontal northeastward velocity, $\mathbf{u} = 3 \text{ km d}^{-1}$, obtained from acoustic Doppler current profiler measurements (Fig. 2.1b-d; Siegel et al., 2020). As the northeastward direction of \mathbf{u} was also the direction of displacement (\mathbf{x}) from epoch 1 to epoch 3 (Fig. 2.1b-d), we were able

to estimate the mesoscale transport of ^{234}Th by \mathbf{u} using the ^{234}Th gradient obtained from samples epochs 1 and 2. The average ^{234}Th activity in the upper 25 m of each epoch was 1.36 dpm L $^{-1}$ for epoch 1 and 1.48 dpm L $^{-1}$ for epoch 3, leading to $a = 0.12 \text{ dpm L}^{-1}$, with a distance between the two epochs of $x = 75 \text{ km}$. These values are used to compute the horizontal ^{234}Th transport in section 3.1.3.

For the vertical advection and diffusion, we calculated the vertical ^{234}Th gradients, $\Delta A_{\text{Th}} / \Delta z$, for each ^{234}Th profile (Fig 2.2 profiles). We then used an average vertical velocity and diffusivity coefficient derived from two years (Jun. 2008 – Jan. 2010) of Seaglider data at OSP (Pelland et al. 2017). The upward mean vertical velocity, $= 0.25 \text{ m d}^{-1}$, reflects seasonal Ekman pumping. The diffusivity coefficients obtained by Pelland et al. (2017) varied in depth at the boundaries of the transition layer (35-80 m). Based on their results, we used a high diffusivity coefficient of $k=10\cdot3 \text{ m}^2 \text{ s}^{-1}$ to simulate diffusion above the transition layer, $k=10\cdot4 \text{ m}^2 \text{ s}^{-1}$ was used inside the transition layer (35-80 m), and $k= 10\cdot5 \text{ m}^2 \text{ s}^{-1}$ below ($> 80 \text{ m}$).

2.2.3 CONVERSION TO PARTICLE FLUXES USING SIZE-FRACTIONATED PARTICLE-TO- ^{234}Th RATIOS

POC/ ^{234}Th ratios derived from the in situ pumps were used to obtain carbon fluxes. Because zooplankton swimmers contaminated the larger particles ($>51 \mu\text{m}$), the medium-sized particle class ($5 - 51 \mu\text{m}$) was used to calculate reported POC fluxes. These pump-derived ratios were averaged across the cruise duration and linearly interpolated to the SS model depth bins. The POC/ ^{234}Th ratio average values were highest near the surface (from 5.30 ± 1.90 at 50 m), decreasing rapidly with depth below the primary production zone (to

$0.88 \pm 0.16 \mu\text{mol dpm}^{-1}$ at 500 m).

THE NORTH ATLANTIC OCEAN

2.2.4 ^{234}Th -DERIVED PARTICLE FLUXES IN THE NORTH ATLANTIC

The data used in this analysis comes from the NASA EXPORTS cruise to the North Atlantic in May 2021 which consisted of three ships, the RRS Cook, the RSS Discovery, and a ship from a complementary study, the R/V Sarmiento de Gamboa (WHOI Ocean Twilight Zone Project; Johnson et al., 2024). Similar to the Pacific cruise (Section 2.1.1), a 3-epoch style sampling pattern following a Lagrangian float was utilized (Fig. 2.1b-d). However, because of the intense dynamics in the North Atlantic (Damerell et al., 2016; Erickson et al., 2020), the float was strategically placed inside a previously identified anticyclonic eddy (Erickson et al., 2023). Once released, the float was followed by a process ship, the RRS Cook, while a sampling ship, RSS Discovery, sampled a grid-like pattern around the float (Johnson et al., 2024). Over 800 ^{234}Th samples were obtained from over 50 CTD casts off the RSS Discovery, with casts organized into eddy-core and outside-eddy-core bins (for full details, see Clevenger et al., 2024).

In brief, the eddy-core samples (within 15 km from the eddy center) were used to compute ^{234}Th and particulate carbon fluxes. Both 1D-SS and 1D-NSS models were assessed, with the 1D-NSS model results reported as the best estimate as it accounts for the temporal change in the flux expected at the end of a phytoplankton bloom (Clevenger et al., 2024).

In-situ physical features were measured by gliders, and geostrophic velocities were obtained from aviso-derived sea surface height (SSH). However, contrary to what had been done in the North Pacific, the nature of the survey and the intense dynamics made an in-

situ-derived calculation of the transport difficult and unreliable. Instead, I use a modeling approach (NEMO-LOBSTER) to quantify the potential impact of physical ^{234}Th transport inside a simulated eddy (see section 2.2.2, Clevenger et al., 2024) that is expanded to include analysis across all identified eddies and frontal regions in the model in Chapter 3 (Wyatt et al., 2024 in prep).

2.2.5 ESTIMATING PHYSICAL ^{234}Th TRANSPORT INSIDE A SIMULATED NORTH ATLANTIC EDDY

To examine the impact of eddy dynamics and transport on the ^{234}Th tracer budget (Eq. 2.2), I used a case study approach inside an idealized model coupled with a ^{234}Th dynamics model (Clevenger et al., 2024). This model is the idealized, submesoscale permitting physical model (NEMO; Madec, 2008) coupled with a simplified biogeochemical model with explicit ^{234}Th cycling (LOBSTER-Th; Resplandy, 2012) also used in Chapter 3 (Wyatt et al., 2024 in prep). In brief, the modified NEMO-LOBSTER model is an idealized double-gyre model representative of the North Atlantic Ocean, consisting of a rotated beta-plane with $1/54^\circ$ (2 km) physical resolution in the horizontal, degraded to $1/9^\circ$ (12 km) for the biogeochemistry, and 30 z-coordinate vertical layers that resolve eddies and fronts. The model was forced with a climatological atmosphere, simulating generalized North Atlantic dynamics, comparable to but not specifically simulating the EXPORTS campaign location or timing. The ^{234}Th model includes radioactive production and decay, with adsorption to the particulate stocks (phytoplankton, zooplankton, or the two classes of detrital particles) and desorption to a dissolved state.

The model output was examined, and a simulated mesoscale eddy (sim-eddy) compa-

rable to the observed 2021 EXPORTS North Atlantic eddy (obs-eddy) was selected and analyzed as a case study. The simulated eddy was located at 44° N, 64° E and appeared on February 19th, lasting for > 90 days until May 20th. This is compared to the sampled EXPORTS eddy, identified on March 19th and lasted through the end of the cruise deployment, May 30th (Erickson et al., 2020). Both eddies (sim-eddy and obs-eddy) were anti-cyclonic, establishing themselves during the spring phytoplankton bloom and remaining coherent until the post-peak period. The sim-eddy was roughly 50 km in diameter, comparable to the 30 km diameter of the obs-eddy. The simulated horizontal ^{234}Th gradient at 75 m depth reached a maximum of approximately 0.3 dpm km^{-1} , comparable to the obs-eddy maximum gradient of 0.2 dpm km^{-1} . The observational cruise sampling occurred at roughly 2-day intervals with distances of 1-15 km between samples. Thus, the model biogeochemical resolution of 12 km and the 2-day output were reasonable approximations for the observed sampling intervals, while the higher physical resolution (2 km) resolves the fine-scale dynamics in which we are interested.

A full accounting of the ^{234}Th budget (e.g., the radioactive production and decay of ^{234}Th , adsorption/desorption, the sinking particulate flux, and the physical transport of ^{234}Th) inside the sim-eddy core was then analyzed to estimate the fraction of the ^{234}Th disequilibrium that could be attributed to physical transport following equation 2.2.

2.3 RESULTS

NORTH PACIFIC RESULTS

2.3.1 OBSERVED ^{234}Th RADIOACTIVITY AND STEADY-STATE FLUXES NEAR OSP

Profiles of ^{234}Th activity were assembled from over 60 CTD casts. Generally, ^{234}Th was low in the surface ($1 - 2 \text{ dpm L}^{-1}$, solid markers, Fig 2.2), where chlorophyll fluorescence was high ($> 0.1 \mu\text{g L}^{-1}$, hollow markers), consistent with a sinking flux generated by surface primary production. ^{234}Th activity increased with depth until 110 m, where it reached equilibrium with observed ^{238}U activity near the bottom of the primary production zone (where chlorophyll fluorescence drops below 10% of the upper water column maximum, $117 +/- 5 \text{ m}$).

A cruise mean 1D-SS estimate was also prepared using the 1D-SS model calculated for every profile (n=61), with uncertainty given as the standard deviation across all profiles ($324 + 80 \text{ dpm m}^{-2} \text{ d}^{-1}$ in the upper 10 m to $1,452 + 304 \text{ dpm m}^{-2} \text{ d}^{-1}$ by 100 m). At 200 m, some fluxes reached $3,000 \text{ dpm m}^{-2} \text{ d}^{-1}$ or higher (Fig. 2.2; Table S1 in Buesseler et al., 2020), while at other stations, the flux estimate was indistinguishable from zero.

^{234}Th activities were also averaged across epochs, with these averages used to calculate a 1D-NSS estimate (see section 3.1.2) that was roughly 30% lower than the 1D-SS cruise average throughout the upper 200 m. Whether the cruise sinking fluxes are better represented by the 1D-SS or 1D-NSS estimate of the flux is further explored in the discussion section 4.1.

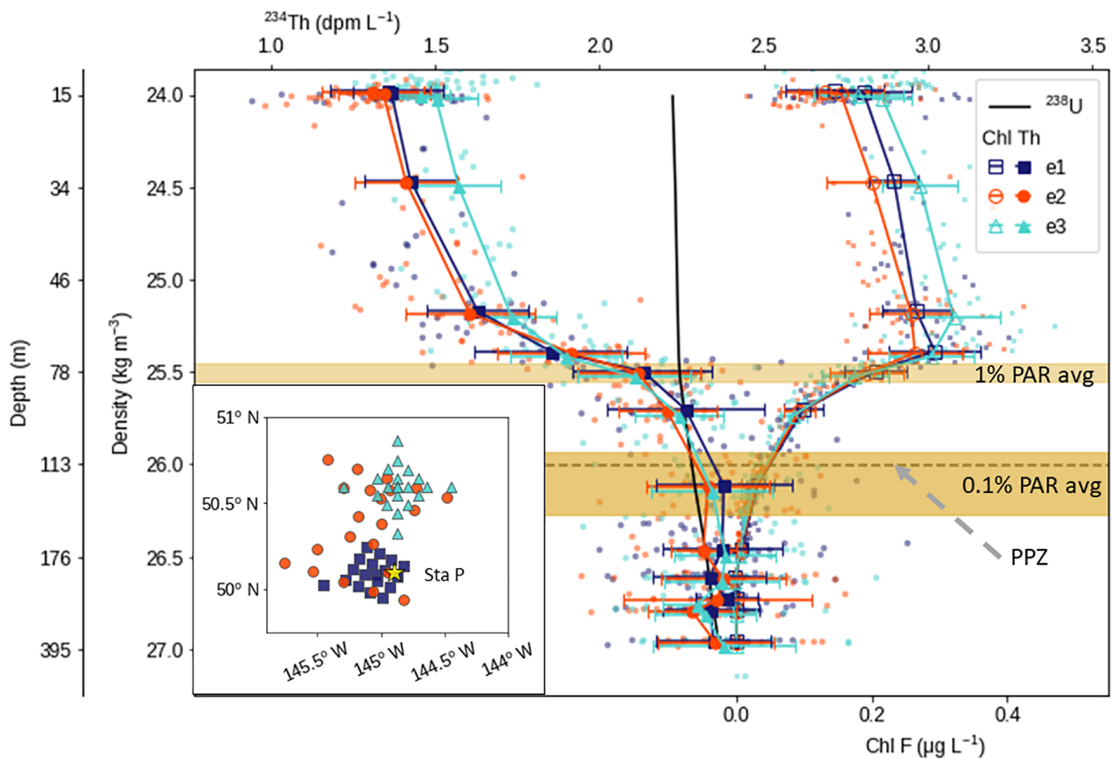


Figure 2.2: Thorium-234 activity and chlorophyll fluorescence versus density with equivalent depths on secondary y-axis. Thorium-234 activity (circles, dpm L⁻¹, upper x-axis) and chlorophyll fluorescence (squares, µg L⁻¹, lower offset x-axis) versus density, colored by epoch. Epoch averages shown as larger symbols with the error bar denoting one standard deviation. Uranium-238 activity (dpm L⁻¹) is shown as a vertical black line. Significant depths indicated are the cruise average 1% photosynthetic active radiation zone (PAR, light shaded yellow; 79 ± 6 m) and 0.1% PAR (medium shaded yellow, 118 ± 9 m) regions, the bottom of the primary production zone (PPZ, dashed gray line; 117 ± 5 m). Map insert shows spatial location of sampling relative to Station P. DOI: <https://doi.org/10.1525/elementa.2020.030.f1>

2.3.2 INTERPRETING CHANGE IN ^{234}Th RADIOACTIVITY AS TEMPORAL VARIABILITY

The high resolution and sampling size of this study captured a total spatiotemporal variability of ^{234}Th activity that was relatively low at all depths in the water column (one standard deviation 0.17 dpm L⁻¹ per depth, between 6%–11% of the mean ^{234}Th activity). However, despite this consistency in ^{234}Th activity across all three epochs, there is a visible deviation between the epoch 1 mean ($^{234}\text{Th}_{e1} = 1.63 \pm 0.15 \text{ dpm L}^{-1}$ at 55 m) and

epoch 3 mean ($^{234}\text{Th}_{e3} = 1.73$ at +/- 0.13 dpm L $^{-1}$ at 55 m, Fig. 2.2) that is statistically significant in the upper 65 m (p-values < 0.05, welch's t-test). As this change occurs over approximately 3 weeks, this deviation suggests consideration of the 1D-NSS model (Eq. 2.3). Using the epoch mean ^{234}Th activities at each depth from epoch 1 and epoch 3 over a period of 18 days, we find a cruise average 1D-NSS flux of 221 + 120 dpm m $^{-2}$ d $^{-1}$ in the upper 10 m to 1,024 + 545 dpm m $^{-2}$ d $^{-1}$ at 100 m, which is significantly lower than the 1D-SS estimate at depths shallower than 200 m (p-values < .05).

2.3.3 INTERPRETING CHANGES IN ^{234}Th RADIOACTIVITY AS SPATIAL VARIABILITY AND TRANSPORT

Alternatively, the deviation in ^{234}Th activity from epoch 1 to epoch 3, with the center points of these epochs located roughly 75 km apart, can be interpreted as a mesoscale (100 km) spatial gradient (1.6 x 10 $^{-6}$ dpm L $^{-1}$ m $^{-1}$ at < 25 km) subject to large-sale transport by the northeastward velocity field. With horizontal surface velocities of 2–3 km d $^{-1}$, this gradient would result in a horizontal advection of 125 dpm m 2 d 1 or 20% of the cruise average 1D-SS flux (666 dpm m $^{-2}$ d $^{-1}$ at 25 m). The relative impact of this horizontal advection decreases with depth as velocities decrease thus we can consider 20% an upper bound. However, the mesoscale spatial variability is somewhat obscured by stronger fine-scale (< 10 km) spatial variability. Differences between stations produce fine-scale spatial variability, an order of magnitude greater than the mesoscale (1 x 10 $^{-5}$ dpm L $^{-1}$ m $^{-1}$) in the upper 100 m (Fig. 2.1b-d).

Unlike horizontal transport, vertical transport is relatively easy to calculate as the data is vertically resolved for each CTD cast, thus gradients can be calculated per profile then

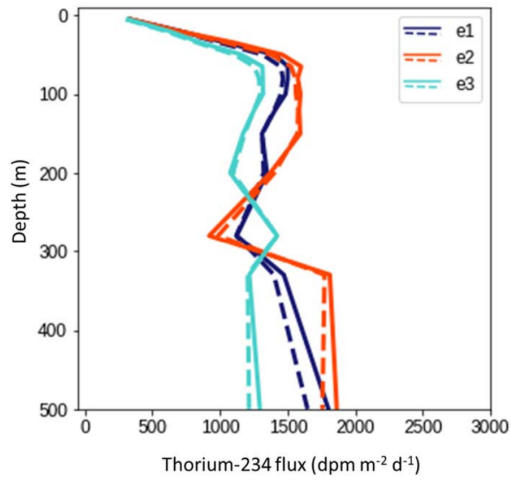


Figure 2.3: Epoch average 1D-SS ^{234}Th flux (dashed lines) with integrated vertical advection and diffusion included (solid lines), colored by epoch.

averaged across each epoch for comparison to epoch mean fluxes. During the EXPORTS cruise, the strongest vertical gradient occurred at 60–100 m, close to the 1% PAR boundary where chlorophyll fluorescence also exhibited strong variation (average $0.0175 \text{ dpm L}^{-1} \text{ m}^{-1}$, Fig. 2.2). Using the seasonal Ekman pumping vertical velocity ($w = 0.25 \text{ m s}^{-1}$) and diffusivity coefficients ($k = 10^{-3} \text{ m}^2 \text{ s}^{-1}$ in upper 35 m, $k = 10^{-4} \text{ m}^2 \text{ s}^{-1}$ from 35–80 m, $k = 10^{-5} \text{ m}^2 \text{ s}^{-1}$ below 80 m) from Pelland et al. (2016), we get a total vertical transport of less than $20 \text{ dpm m}^2 \text{ d}^{-1}$ into the upper 25 m (< 6% epoch averaged 1D-SS fluxes at 25 m, Fig. 2.3). This decreases the size of the ^{234}Th - ^{238}U deficit at the surface but does not affect sinking particle flux (Eq. 2.2), however, because dynamical transport is not included in the 1D-SS estimate (Eq. 2.1), this upward transport causes the 1D-SS model to underestimate the sinking (dashed vs. solid lines, Fig. 2.3). Combined with the impact from the horizontal transport we would expect that physical ^{234}Th transport could have biased the 1D-SS estimate by up to 26%.

NORTH ATLANTIC RESULTS

2.3.4 OBSERVED ^{234}Th RADIOACTIVITY AND STEADY-STATE FLUXES NEAR PAP

Similarly to the Northeast Pacific, ^{234}Th radioactivity was gathered from over 50 CTD casts, however, in the North Atlantic the cruise timing, May 1 - May 27, was coincident with the decline of the spring phytoplankton bloom (e.g. Martin et al., 2012; Le Moigne et al., 2013), leading to a strong temporal change in ^{234}Th activities of -1.0 dpm L^{-1} at 20-50 m over the 26-day cruise duration. This ultimately led to the use of the 1D-NSS model for POC flux calculations, which we report here. Generally, ^{234}Th fluxes in the North Atlantic were much larger than observed in the Pacific and increased as the cruise progressed, from $2200 \pm 1400 \text{ dpm m}^{-2} \text{ d}^{-1}$ in epoch 1, to $5400 \pm 1680 \text{ dpm m}^{-2} \text{ d}^{-1}$ in epoch 3 at 500 m (See Clevenger et al., 2024 for full details).

2.3.5 ^{234}Th SPATIAL VARIABILITY AND TRANSPORT IN A SIMULATED

NORTH ATLANTIC EDDY

From model output specific to the eddy center, we determined the percentage of the total simulated ^{234}Th downward flux (sinking + transported) due to dynamical transport and compared it to the percentage of the 1D-NSS term. The total modeled physical transport was 11% of the total 1D-NSS ^{234}Th flux at 75 m, increasing to 27% of the total 1D-NSS ^{234}Th flux at 550 m. These percentages are generally within the error of the total flux measurements presented in this study, supporting the assumption that the physical transport term is small compared to the sinking flux inside a coherent eddy during the decline of a spring phytoplankton bloom. Model physical transport in sim-eddy increased with depth,

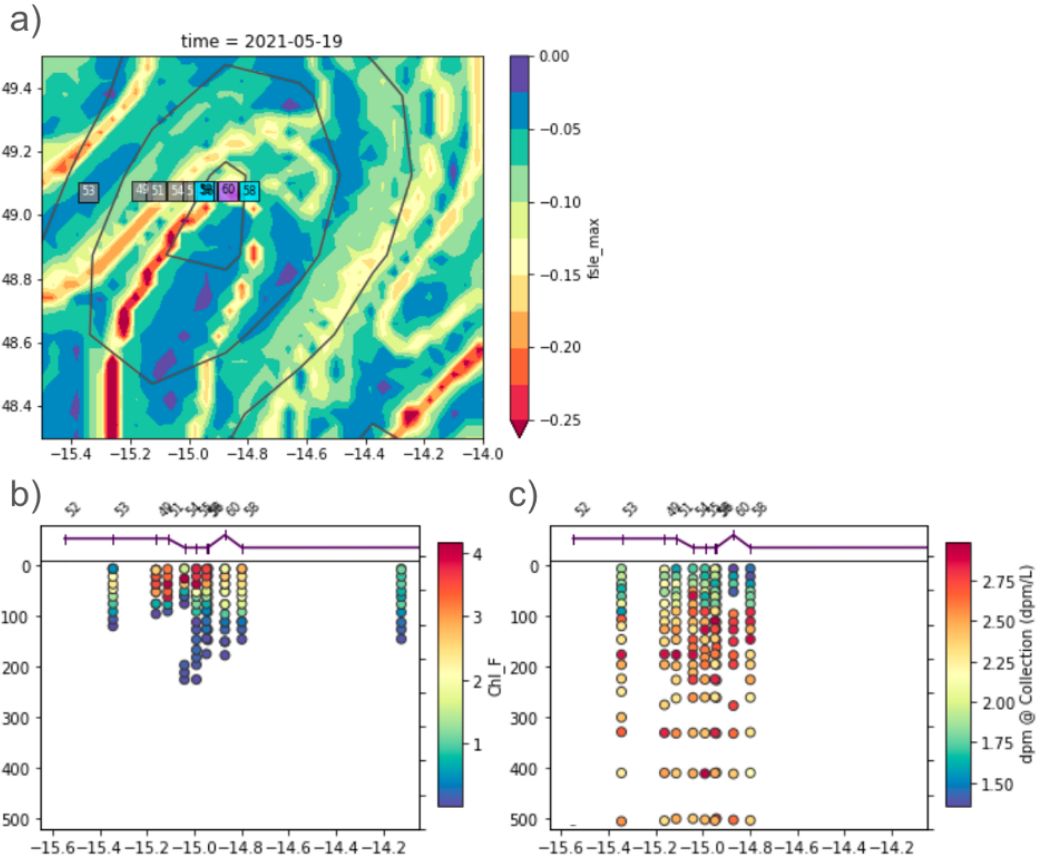


Figure 2.4: "Edge" experiment, sampling across a front. a) sampling site locations (squares) across a strong front indicated by high absolute values of finite series Lyapunov exponents (FSLE) which indicate areas where there is strong stretching caused by mesoscale velocities (red regions), with sea surface heights shown as black contours. Lower panels are sample site profiles in depth (y-axis) of by longitude (x-axis) for b) chlorophyll fluorescence and c) thorium radioactivity.

from 11% of the 1D-NSS estimate (2721 dpm L^{-1}) at 75 m to 40% of the 1D-NSS estimate (5398 dpm L^{-1}) at 500 m depth. This indicates that targeting an eddy for ^{234}Th sampling provides a reasonable framework from which to use the 1D ^{234}Th estimates, as the impact of physical dynamics in the sim-eddy is relatively small near the surface.

During the second epoch, a transect perpendicular to the eddy boundary was also sam-

pled (“edge experiment”, Fig. 2.4). However, these data were not reported by Clevenger and co-authors, as the transect crosses a strong front (red region, panel a) making interpretation of that data difficult. Figure 2.4 shows that in the vicinity of the front (station 60), spatial gradients in ^{234}Th activity approach $10^{-4} \text{ dpm L}^{-1} \text{ m}^{-1}$ indicating intense fine-scale spatial variability, likely induced by stirring and potentially vertical transport generated by the eddy and its interactions with the flow field around it. Indications that vertical transport is important across this front are visible at station 54, where high ^{234}Th ($> 2.75 \text{ dpm L}^{-1}$) and low chlorophyll ($< 1 \mu\text{g L}^{-1}$) water is observed above 100 m, while they are only observed below 100 m at other stations (panel c, Fig. 2.4). The presence of this high-thorium, low-chlorophyll water at shallower depth at the front are consistent with a vertical transport of deep water upward. In contrast, to the east of this location (stations 56, 58 & 60), ^{234}Th activity is comparatively low ($< 2 \text{ dpm L}^{-1}$ at 80 m), with high chlorophyll penetrating to 100 m suggesting downwelling velocities.

2.4 DISCUSSION

2.4.1 SPATIAL VS. TEMPORAL VARIABILITY OF SINKING FLUXES IN THE NORTHEAST PACIFIC

In section 3.1.1 we showed that there is a discernible difference between epoch 1 (1.63 dpm L^{-1}) and epoch 3 (1.73 dpm L^{-1}) near-surface ^{234}Th activity during the 2018 Northeast Pacific EXPORTS cruise. If we attribute the change to a mesoscale spatial gradient (Section 3.1.3), then our estimate of horizontal transport would reduce the 1D-SS estimate by 20%. In contrast, if we consider the change as a seasonal temporal variation, then the 1D-NSS estimate, which is 30% less than the 1D-SS, is more likely to represent the true

sinking flux. In Buesseler et al., (2020) the 1D-NSS estimate was thus considered a lower bound and the 1D-SS an upper bound of the sinking flux. Here we build on that interpretation and suggest that there is more evidence to support the 1D-NSS interpretation.

Generally, the 1D-NSS is used to interpret ^{234}Th deficits when it is expected that there will be large changes in ^{234}Th radioactivity over time, e.g. during or after a spring phytoplankton bloom. In the Northeast Pacific in August, the modest spring phytoplankton bloom has passed and we expect particle flux changes to be relatively small due to the low seasonality of the region but still declining in time (Wong et al., 1999; Charette et al., 1999). While it is difficult to discern whether that is the signal observed in the EXPORTS data, we examine other lines of support for this result.

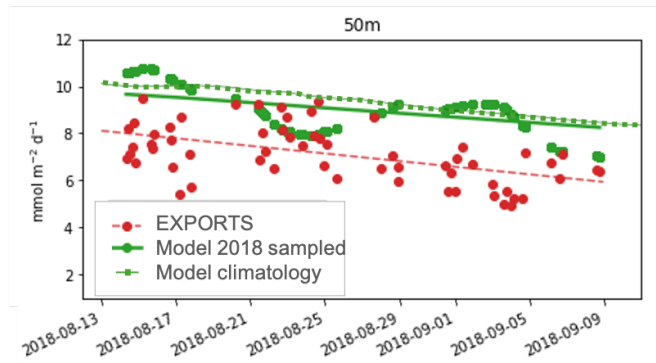


Figure 2.5: Observed North Pacific EXPORTS POC flux at 50 m (red dots) and mean observed trend (red dashed) vs. subsampled MOM6-COBALT model 2018 output (green dots) with linear trend (green line) compared to model climatology (green dashed).

The model, MOM6-COBALT used in Chapter 1, is a global general circulation model forced with a realistic atmospheric reanalysis, with $\frac{1}{2}$ degree (50 km) resolution in the horizontal (See Wyatt et al., 2022, for full details). Due to the model resolution, it is not expected to reproduce comparable mesoscale (75 km) spatial variability, however, it has shown some skill in representing the seasonal trends of this region. This model was subsampled using latitude, longitude, and time of the EXPORTS ^{234}Th data. Despite a mean positive bias in the model POC flux (high bias of $2\text{ mmol C, m}^{-2}\text{ d}^{-1}$), the subsampled

model (green dots) captures the temporal change of the cruise data (red dots) of approximately $-2 \text{ mmol POC m}^{-2} \text{ d}^{-1}$ over the 35-day cruise (Figure 2.5). Further, this decline is also consistent with the model seasonal climatology (dashed line), supporting the idea that the change in sinking flux between epochs 1 and 3 captures the seasonality of the sinking flux.

Thus here I conclude that the 1D-NSS estimate is likely more representative of the true sinking flux during the cruise period, though the 1D-SS still represents an upper bound. However, the difficulty in interpreting these data, despite the high-resolution sampling, highlights the fact that variability in ^{234}Th observations can conflate spatial and temporal changes.

2.4.2 HIGH-RESOLUTION SAMPLING CAPTURES FINE-SCALE SPATIAL VARIABILITY

The fine-scale ($< 10 \text{ km}$) spatial variability sampled in the Northeast Pacific ($10^{-5} \text{ dpm L}^{-1} \text{ m}^{-1}$) suggests that it would be difficult to distinguish the mesoscale (100 km) spatial variability ($10^{-6} \text{ dpm L}^{-1} \text{ m}^{-1}$) without the high sampling density in epochs 1 and 3. Moreover, the standard deviation across each epoch 0.17 dpm L^{-1} exceeds the observed difference between the epoch 1 and epoch 3 means (0.1 dpm L^{-1} difference at 55 m) indicating that a shorter cruise duration ($< 30 \text{ days}$) may have been insufficient to capture the long term temporal variability given the high fine-scale spatial variability. In the North Atlantic, where fine-scale spatial variability is comparable but the temporal signal is an order of magnitude stronger, (1.0 dpm L^{-1} from epoch 1 to epoch 3), sampling density is less of a concern.

Similar to past work which has set conditions such as duration, timing, and method of

sampling, that should be met for the use of the 1D-NSS model (Savoye et al., 2006; Resplandy et al., 2012; Ceballos-Romero 2018) these results indicate that the number of samples taken at each time step (e.g. epoch 1 and epoch 3 of the EXPORTS Pacific cruise) should be large enough to capture fine-scale variability to obtain a meaningful measure of average ^{234}Th activities in order to use the 1D-NSS framework (Eq. 2.3).

2.4.3 NORTH ATLANTIC SMALL-SCALE SPATIAL VARIABILITY

In the North Atlantic, despite the higher ^{234}Th export fluxes (maximum flux $> 5000 \text{ dpm L}^{-1}$ vs. $< 3000 \text{ dpm L}^{-1}$ in the Northeast Pacific) and strong temporal variability that decreased ^{234}Th activity 1.0 dpm L^{-1} over the duration of the cruise, the fine-scale spatial gradients of ^{234}Th radioactivity in the North Atlantic eddy core sampling are surprisingly comparable in magnitude to those observed in the Northeast Pacific (on the order of $10^{-5} \text{ dpm L}^{-1} \text{ m}^{-1}$). This suggests that targeting an eddy was a successful way to minimize large variations in spatio-temporal dynamics. This result is further supported by the subsampling of the simulated eddy (sim-eddy), for which the full ^{234}Th tracer budget showed that physical dynamic transport accounted for a relatively small proportion of the total sinking flux (11% of 2721 $\text{dpm L}^{-1} < 75 \text{ m}$, 27% at 500 m). During the sampling across the front (edge experiment), however, the spatial gradient reached $10^{-4} \text{ dpm L}^{-1} \text{ m}^{-1}$, an order of magnitude larger than inside the eddy, indicating influences from fine-scale dynamics. This motivates further study of how fine-scale physical dynamics may induce variations that impact the 1D ^{234}Th estimates which I will examine in Chapter 3 (Wyatt et al, in prep).

2.5 CONCLUSIONS

Here we have examined the spatial and temporal variability of ^{234}Th -derived sinking fluxes during two NASA EXPORTS field campaigns in two contrasted export regimes, the low eddy kinetic energy, productivity, and seasonality of the Northeast Pacific, and the large eddy kinetic energy and strongly seasonally productive North Atlantic. Work in the Northeast Pacific highlights the difficulty in disentangling seasonal temporal and mesoscale spatial variability while suggesting that the observed variability captured between epochs was most likely temporal, and linked to the seasonal decline in export production. This work also highlights that the high spatial and temporal resolution of these data was necessary to reveal seasonal decline, as fine-scale spatial variability was relatively high compared to this small temporal variation.

We also show that sampling inside an eddy during the North Atlantic cruise was a successful way to mitigate considerable spatial heterogeneity, as fine-scale spatial variability inside the eddy was comparable to the background variability observed in the Northeast Pacific. The assumption of low physical dynamics was further justified by the use of a model case study that demonstrated that dynamic transport inside a comparable simulated eddy was relatively small, particularly in the upper ocean (11% of 2721 dpm L^{-1} at 75 m, 27% at 500 m). However, the intense variability observed during the cross-eddy front sampling demonstrates the need for a more focused study that quantitatively explores the impact of fine-scale dynamics on particle export and the 1D ^{234}Th flux estimates. Using an idealized model, we examine this fine-scale variability and the implications for ^{234}Th -derived flux estimates in Chapter 3.

*That was one of the most dramatic things that's ever
happened on this boat. I just lost all my best interns.*

—Steve Zissou

3

Evaluation of 1D thorium models and
export around dynamic physical structures
like eddies and fronts

3.0 ABSTRACT

Fine-scale dynamics, such as mesoscale eddies, and fronts in the ocean, can dramatically impact the transport and mixing of biogeochemical tracers, enhancing or suppressing primary production and sinking particle fluxes. To capture the spatio-temporal variability of these fluxes, observations have targeted different regimes, including coherent eddy centers and the highly dynamic frontal regions around them. The naturally occurring radiotracer thorium-234 (^{234}Th) is one method of estimating particle export fluxes in situ, relying on one-dimensional (1D) vertical models of ^{234}Th - and uranium-238 (^{234}Th) radioactive disequilibrium. These 1D models, however, are limited as they lack an accounting of physical dynamics and, therefore, may misattribute changes in ^{234}Th caused by transport to sinking flux. In this work, we use a high-resolution general circulation and biogeochemical model, coupled with a dynamic ^{234}Th model, to assess the ability of 1D steady state (1D-SS, assuming no temporal changes in sinking fluxes and no contribution from transport) and 1D non-steady state (1D-NSS, including temporal changes in sinking but no contribution from transport) models to estimate ^{234}Th sinking fluxes in eddies and fronts. We find that the dynamical transport of ^{234}Th and associated biases on sinking fluxes are statistically lower inside eddies than in frontal regions. The 1D-SS model is, therefore, associated with smaller errors inside eddies, implying that Lagrangian sampling along eddy tracks can minimize errors. Generally, we find that the 1D-NSS estimate should be reserved for cases when export fluxes are large, and the dynamic transport is low, conditions which are met by 25% of the simulated eddies that last longer than 20 days. Near frontal regions, high vertical velocities are shown to decouple the 1D-SS estimate from the actual sinking ^{234}Th .

flux, introducing large variations in sinking estimates ($> 30\%$ of the sinking flux) that make interpretation of ^{234}Th data in such regimes difficult.

3.1 INTRODUCTION

Since the 1960s, the naturally occurring radioisotope thorium-234 (^{234}Th) has been used as a proxy for particle cycling and transport in the upper ocean (Ceballos-Romero et al., 2022). In particular, ^{234}Th -based studies have been invaluable in evaluating the strength of the gravitational sinking pump, the process by which upper ocean ecosystems vertically transport surface ocean carbon to the abyss primarily via the sinking of organic particles. Because it adsorbs to particles, ^{234}Th is subject to transport and sinking on nearby organic matter (OM), while its non-particle reactive parent, Uranium-238 (238U), remains conservative throughout the water column. This results in a measurable disequilibrium between the two, proportional to the fluxes of matter on which the ^{234}Th is adsorbed (Fig. 3.1). For example, regions of high biological production correspond to low $^{234}\text{Th} : 238\text{U}$ ratios, as ^{234}Th is scavenged out of the dissolved pool and exported on sinking OM particles like dead phytoplankton and zooplankton fecal pellets (Waples et al., 2006;). However, it has been shown that fine-scale dynamical features, such as eddies and fronts, may induce intense vertical velocities that modulate plankton production (Freilich and Mahadevan, 2019; Levy et al., 2012, 2024) and the magnitude of local sinking fluxes (e.g. Stukel et al., 2018, Liu et al 2018). Capturing this variability accurately is one challenge of observing sinking fluxes and obtaining global estimates of the biological carbon pump (Boyd et al., 2019).

Particulate organic carbon (POC) collection methods, like sediment traps, require long in situ collection periods and are subject to sampling biases that can vary with local con-

ditions, such as hydrodynamics or zooplankton grazing near the trap mouth. In contrast, thorium-based method is invariable despite changes in ocean temperature, dynamics, or chemistry and require a small sample volume (Clevenger et al., 2021) that can be obtained from conductivity, temperature and depth (CTD) casts making ^{234}Th -derived POC export observations easily obtainable and performable at high spatial and temporal density (Buesseler et al., 2020). Thus, to date, the ^{234}Th method has been used in over 200 studies (Ceballos-Romero et al., 2021) to calculate over 10,000 POC export profiles (Le Moigne et al., 2013).

The ^{234}Th method of estimating POC export relies on a 1D accounting of radioactivity in seawater samples that neglects the impact of physical dynamics, such as the advection and diffusion of ^{234}Th -laden or ^{234}Th -replete waters into the sampling area. These models equate the entire depth-integrated ^{234}Th - ^{238}U deficit (Fig. 3.1) to a sinking ^{234}Th flux. This flux is then converted using a carbon-to- ^{234}Th ratio derived from co-located sediment traps or in situ pumps to estimate a POC flux. The steady-state (1D-SS) version of this model requires a single CTD cast and pump or sediment trap deployment. However, previous work has shown that the 1D-SS assumption is poor in highly productive regions when temporal changes in particles production cannot be neglected (Ceballos-Romero et al., 2018). For example, the 1D-SS estimate is systematically biased in highly temporally variable phytoplankton blooming period, underestimating the export flux when particle production is increasing (before and during peak bloom) and overestimating the export flux when production is decreasing (post-bloom). A non-steady-state model aims at improving this bias by considering the temporal change in thorium activity estimated in-situ from repeat sampling (e.g. Buesseler et al., 2009). This 1D-NSS estimate, however, requires the reoccu-

pation of a sampling site over at least 10 days (Savoye et al., 2006; Resplandy et al., 2012), making the estimate more operationally difficult and expensive. Both 1D ^{234}Th export estimates (1D-SS and 1D-NSS) still generally disregard the impact of physical dynamics despite the importance of dynamical ^{234}Th transport on ^{234}Th budgets due to the presence of fine-scale dynamics (Resplandy et al., 2012; Roy-Barman et al., 2019; Xie et al., 2020).

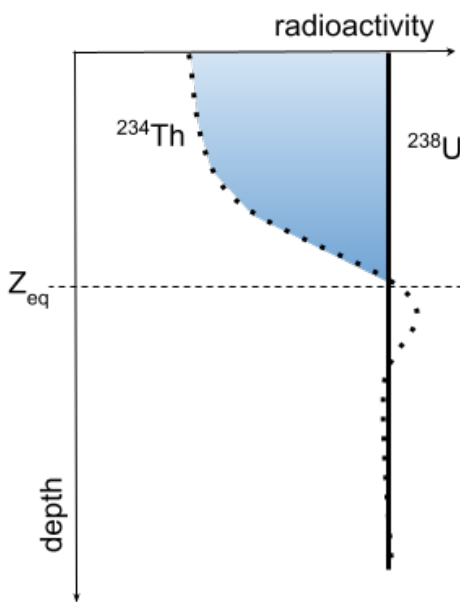


Figure 3.1: Schematic of thorium-234 (dotted line) and uranium-238 (solid line) radioactivity in the water column. Near the surface, thorium activity is lower than uranium as it is removed from the water column on sinking particles to which it is adsorbed. The thorium deficit with respect to uranium can be integrated in depth (blue shading) to calculate a 1D estimate of the sinking thorium flux (see Method section 2.2). At the equilibrium depth, Z_{eq} , the two isotopes reach equilibrium as sinking fluxes equate with remineralization rates.

Fine-scale dynamical structures, like eddies and fronts, are viewed as hot spots of POC export (e.g. Benitez-Nelson et al., 2007; Shatova et al., 2012; Estapa et al., 2015; Waite et al., 2016; Haeck et al., 2023) thus there is interest in targeting such features in observational studies to better understand the processes that control POC export variability. For example, in 2022, the NASA EXPORTS campaign in the North Atlantic Ocean targeted the core of an anticyclonic eddy as well as the frontal structures at its periphery, with a suite of

observational tools and techniques to study the mechanisms of biological pump efficiency, from primary productivity through particle export. This campaign included more than 50 1D ^{234}Th -derived profiles of POC export, capturing the spatial and temporal variability in the eddy and the associated fronts (Clevenger et al., 2024). Interpretation of these results, however, was limited to the eddy core, where the eddy's coherency allowed for an assumption of low physical dynamical impact on the ^{234}Th -derived estimates.

In this study, we simulate in situ sampling strategies, including Lagrangian eddy tracking and cross-frontal sampling, inside a general circulation model coupled with biogeochemical and ^{234}Th dynamics. We estimate the 3D-model sinking flux using three observation-like 1D ^{234}Th sinking flux models (steady state, non-steady state, and non-steady state with Lagrangian eddy tracking) and compare them to the fully coupled, ground truth 3D-model sinking flux. This allows us to assess and quantify the bias induced by physical dynamics near eddies and fronts. We confirm that eddy centers have statistically lower dynamical contributions to the ^{234}Th budget, allowing for smaller errors when using the 1D steady-state estimate for sinking fluxes. The non-steady state approach, however, should be reserved only for periods of high fluxes and when dynamical transport is low, e.g. inside an eddy during a spring bloom as not to conflate physical transport of ^{234}Th with temporal changes). Frontal regions, characterized by large horizontal gradients, exhibit strong vertical velocities that decouple the magnitude of the deficit from the sinking flux, which introduce strong biases in the 1D approach. Thus, interpreting ^{234}Th and particle fluxes across fronts should be cautiously approached.

3.2 METHODS

3.2.1 OCEAN MODEL DESCRIPTION

This study uses the modified NEMO-LOBSTER idealized double gyre model described in Resplandy et al. (2012). In brief, the double gyre represents the North Atlantic Ocean, consisting of a rotated beta-plane with $1/54^\circ$ (2 km) physical resolution in the horizontal and 30 z-coordinate vertical layers (5, 15, 25, 36, 48, 60, 75, 91, 111, 136, 167, 209, 263, 335, 428, 547 and 15 deeper depths) that resolves eddies and fronts (Fig. 3.2). Model circulation is driven by seasonal zonal profiles of wind, solar radiation, heat, and salt fluxes, producing a baroclinically unstable jet region that separates the subpolar gyre in the north from the subtropical gyre in the south (Lévy et al., 2010, 2012a).

The biogeochemical model, LOBSTER, was run offline at a $1/9^\circ$ (12 km) horizontal resolution using the physical model output of the $1/54^\circ$ and the grid degradation technique detailed in Lévy et al. (2012b). This simplification has previously been shown to sufficiently resolve tracer patterns while improving computational costs. The LOBSTER model includes six tracer pools: phytoplankton, zooplankton, dissolved organic matter (DOM), nitrate, ammonium, and detritus. The detritus pool is formulated with two sinking speeds (large speed = 50 m d^{-1} and small speed = 5 m d^{-1}), allowing for a parametrization of particle aggregation and disaggregation (Aumont, 2003). This model is then coupled to a dynamic ^{234}Th cycling model described in Resplandy et al (2012). The ^{234}Th model includes radioactive production and decay, partitioned between the six biogeochemical tracer pools in either a dissolved or particulate (adsorbed to phytoplankton, zooplankton, or the two classes of detrital particles) state.

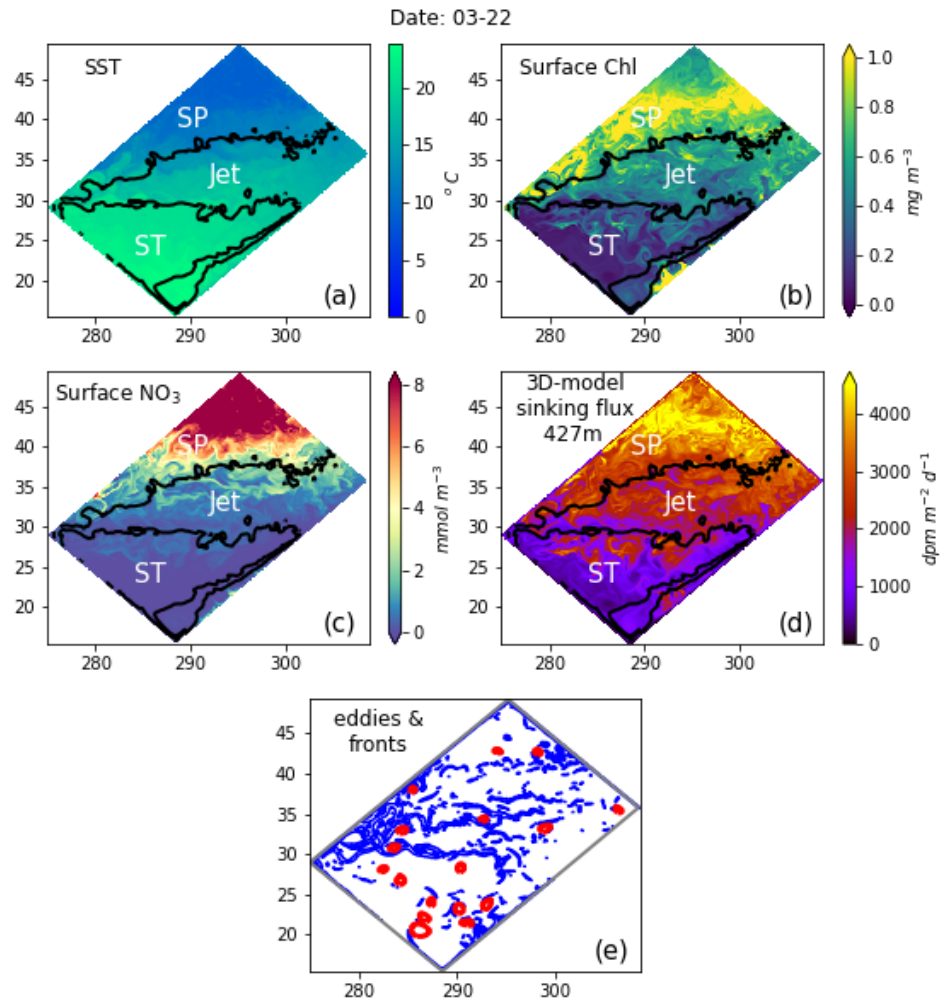


Figure 3.2: NEMO-LOBSTER model snapshot on March 31st. of a) sea surface temperature, b) chlorophyll concentration derived from phytoplankton biomass nitrogen using using a constant chlorophyll to carbon mass ratio of 1:60 and a C:N Redfield ratio of 6.6, c) surface nitrate concentration and d) sinking thorium flux at 428 m. Subtropical region in the south, jet region in the middle and subpolar region in the north are separated by black contours in panels a-d.

This study analyzes the last year of a 100-year model spinup. Because the physical model is forced with a climatological atmosphere, this simulated year is not representative of any particular period but is representative of a typical year spanning the three biomes: the low productivity subtropical gyre (annual mean chlorophyll $< 0.15 \text{ mg m}^{-3}$), and a spring bloom that propagates northward across the jet region ($0.15 \text{ mg m}^{-3} < \text{annual mean chlorophyll} < 0.3 \text{ mg m}^{-3}$) and subpolar gyre (annual mean chlorophyll $> 0.3 \text{ mg m}^{-3}$, Fig 3.2b).

3.2.2 ^{234}Th SINKING FLUXES: 1D-SS AND 1D-NSS MODELS

All the 1D ^{234}Th sinking fluxes are calculated from simulated ^{234}Th activity in the water column using a depth-integrated $^{234}\text{Th} - ^{238}\text{U}$ disequilibrium. The parent radioisotope, ^{238}U , is conservative throughout the water column, scaling with salinity (Chen et al., 1986, Owens et al., 2011; Resplandy et al. 2012) while the daughter isotope, ^{234}Th , adsorbs to particles and is therefore subject to the dynamical transport (advection and mixing) that affect them. The variation of ^{234}Th radioactivity over time can be represented as follows:

$$\frac{dA_{Tb}}{dt} = \int_z \lambda(A_U - A_{Tb}) - E + D \quad (3.1)$$

Where the time tendency of ^{234}Th activity (dA_{Tb}/dt) equals the depth-integrated radioactive disequilibrium between the production of ^{234}Th from parent ^{238}U (λA_U) and the decay of ^{234}Th already present in the water column (λA_{Tb}), minus the sinking flux of ^{234}Th (E), and the three-dimensional ^{234}Th dynamical transport (D). These dynamics are resolved at every grid point in the coupled physics-biogeochemistry-thorium NEMO-LOBSTER model, using the model output depths in section 2.1 for vertical integration. In this study,

the 3D-model sinking flux is considered the model’s “ground truth,” which we compare against using observation-based sampling patterns and analysis to test the influence of the assumptions made during field studies.

In this paper, we discuss four different sinking ^{234}Th fluxes: the ground truth sinking flux (3D-model sinking flux), a one-dimensional steady-state flux (1D-SS) calculated at each model grid point, a 1D non-steady state (1D-NSS) also calculated at each model grid point over a 30-day period, and a Lagrangian non-steady state (1D-NSS-eddy) that tracks the ^{234}Th budget at the center of all modeled eddies over their lifetimes. The 3D-model sinking flux is obtained from the NEMO-LOBSTER model, which includes the full effects of ecosystem and ^{234}Th dynamics, including transport by advection and mixing; it is the baseline to which we compare our 1D models.

The 1D-SS estimate is computed from the coupled NEMO-LOBSTER output as if samples were collected from shipboard casts. The ^{234}Th and ^{238}U activities at every horizontal grid point and time step are taken at each model output depth. From these, a Th deficit term is calculated for use in the Th equation (equation 2). The depth-integrated difference is the 1D-SS sinking flux () according to equation 1, assuming that is negligible. This results in a ^{234}Th -derived 1D-SS export estimate and time series at every point that can be compared to the model output sinking ^{234}Th .

$$E_{SS} = \int_z \lambda(A_U - A_{Th}) dz \quad (3.2)$$

The 1D-NSS estimate is also applied to the NEMO-LOBSTER model at every grid point using a 10-day estimation of the ^{234}Th temporal change. This dA_{Th}/dt was calculated at each depth as the 10-day linear trend of ^{234}Th activity A_{Th} (dpm L $^{-1}$) over time,

from 5 days before to 5 days after a given time step. The time scale of 10 days was chosen as it has been recommended by past literature because as a minimum time frame to capture temporal changes (e.g., Savoye et al., 2006; Resplandy et al., 2012) and minimizes the time lost on the calculation – i.e. a term cannot be calculated for the first 5 days and last 5 days of the simulated year.

The 1D-NSS-eddy Lagrangian estimate is applied to the NEMO-LOBSTER model following eddy trajectories. This flux is calculated using a 10-day similar to the 1D-NSS, but the ^{234}Th and uranium activities are taken as the average inside the eddy boundary.

For each of these 1D estimates, the error is calculated as the difference between the 1D estimated flux and the 3D-model sinking flux at that point in space and time. A root-mean-squared error is calculated for a given period, t , as follows:

$$\text{rmse}_{1\text{D}} = \sqrt{\frac{1}{|t|} \sum_t \left(E_{1\text{D}}(t_i) - E_{3\text{D}}(t_i) \right)^2} \quad (3.3)$$

For the 1D-SS and 1D-NSS estimates taken at every model grid point, this error is calculated over 30 days ($t = 30$) to exceed the 1D-NSS period ($t > 10$ days). This error is also calculated over the eddy lifetime for the 1D-SS and 1D-NSS-eddy using the flux estimates inside a single eddy.

3.2.3 EDDY DETECTION AND SELECTION

We detected eddies in the NEMO-LOBSTER double gyre model using the py-eddy-tracker python program (<https://py-eddy-tracker.readthedocs.io/en/stable/>). The model output was interpolated from two-day averages to one-day temporal resolution. At each time step, a vorticity field is generated using geostrophic velocities calculated from the model

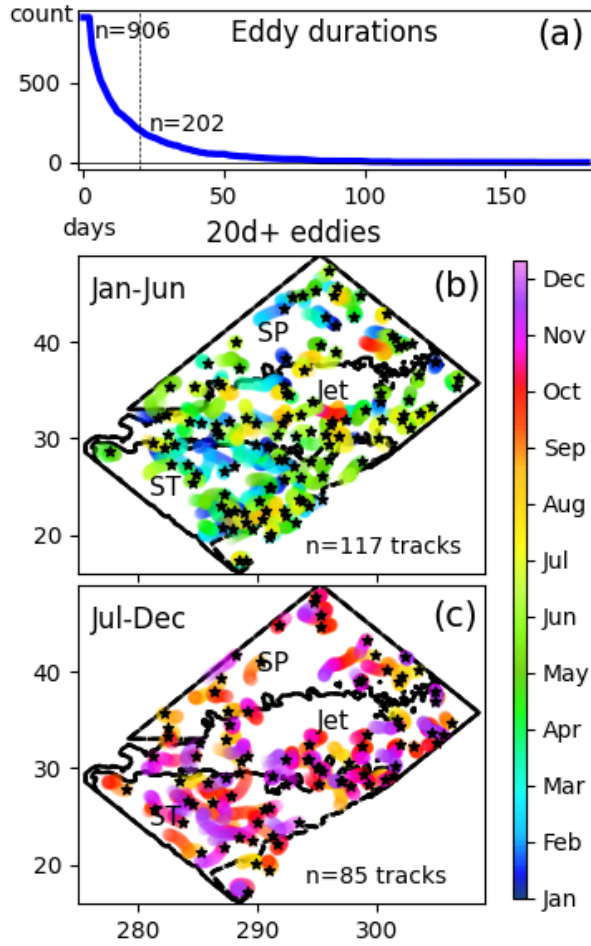


Figure 3.3: Spatial and temporal distribution of simulated eddies in the model domain. a) Number of eddies that last a given duration (days) or more. b-c) Trajectories of the 202 eddies that lasted more than 20 days and started between January-June (b) and July-December (c). Black stars denote eddy start location, colors trails show trajectory and are colored based on timing (months).

sea surface height anomalies. Then a 30-day water parcel trajectory (S) is used to calculate Lagrangian-averaged vorticity deviations (LAVD, ω_{LAVD}) from the mean vorticity ($\bar{\omega}$).

$$\omega_{LAVD} = \int_0^S |\omega - \bar{\omega}| dS \quad (3.4)$$

Closed contours of LAVD, which avoid regions of high strain that may induce large variability in tracer concentrations, are then identified as eddies (Abernathy 2018), comparable to the closed-contour sea surface height method of eddy detection (Chelton 2011). Using this method, 906 distinct eddies were detected in the model domain during the analyzed year. Of these, 202 had eddy tracks lasting 20 days or more (Fig. 3.3a), with a median duration of 43 days. Eddies are located across all biomes and all seasons (Fig. 3.3b & c).

The 1D-SS and 1D-NSS ^{234}Th fluxes were calculated using the average ^{234}Th and uranium activities inside the eddy boundary. For the 1D-NSS model, the linear 10-day term was calculated following the eddy trajectory.

3.2.4 IDENTIFICATION OF FRONTAL REGIONS

Ocean fronts are temporary structures that mark the boundaries between water masses and are characterized by intense horizontal tracer gradients. In this study, fronts were identified as regions where the horizontal sea surface temperature (SST) gradient exceeded 0.15°C per grid cell (Fig. 3.2e), similar to Lévy et al., 2015. This threshold in this study is lower than in Lévy et al. (2015) to include areas of modest strain for more robust statistics. Although the coherent nature of eddies should prevent strong gradients in SST, any points that overlap between this metric and an eddy boundary are classified as eddy points (< .01%). Because fronts are transient, we do not attempt to calculate a 1D-NSS estimate in these regions and instead constrain this study to the 1D-SS ^{234}Th flux estimate only.

3.3 RESULTS

3.3.1 SIMULATED CONTRASTS BETWEEN EDDIES AND FRONTAL REGIONS

The model reproduces the large-scale features of circulation and nutrient dynamics controlling primary production in the three biomes: the subtropical gyre, the jet, and the subpolar gyre. In particular, the model simulates the contrast between the low productivity, low seasonality subtropical gyre and the seasonally high productivity in the subpolar gyre, separated by the jet. The late winter shoaling of the mixed layer spurs a spring bloom of phytoplankton that starts in the jet region in early March and then propagates northward into the subpolar gyre, reaching 42° N by March 22 (Fig. 3.2b). This bloom is associated with a drawdown of the surface nitrate and an increase in particle and ^{234}Th export (Fig. 3.2c & d; See Resplandy et al., 2012 and Levy 2010 for further details). The model is populated by eddies (more than 900 eddies detected in one simulation year) and fronts across all three regions throughout the year (Figs. 3.2e and 3.3b,c). Together, the identified eddies and fronts comprise less than 5% of the total model area for a given time step, with a slightly higher proportion in the jet and subpolar regions (~8%) of the total area, though these numbers may vary slightly with selection criteria.

We find that net primary productivity (NPP) is generally lower inside the eddies (70% of eddies have $\text{NPP} < 1 \text{ mmol N m}^{-2} \text{ d}^{-1}$), than frontal regions (65% of fronts have $\text{NPP} > 1 \text{ mmol N m}^{-2} \text{ d}^{-1}$, Fig. 3.4a). In regions not detected as eddies or fronts, productivity lies between these extremes (55% of points have $< 1 \text{ mmol N m}^{-2} \text{ d}^{-1}$). The lower productivity in eddies yields lower particle export fluxes (~80% of eddies have $\text{export} < 0.5 \text{ mmol N m}^{-2} \text{ d}^{-1}$), whereas high productivity frontal regions are characterized by higher

particle export (50% have $> 1 \text{ mmol N m}^{-2} \text{ d}^{-1}$, Fig. 3.4b).

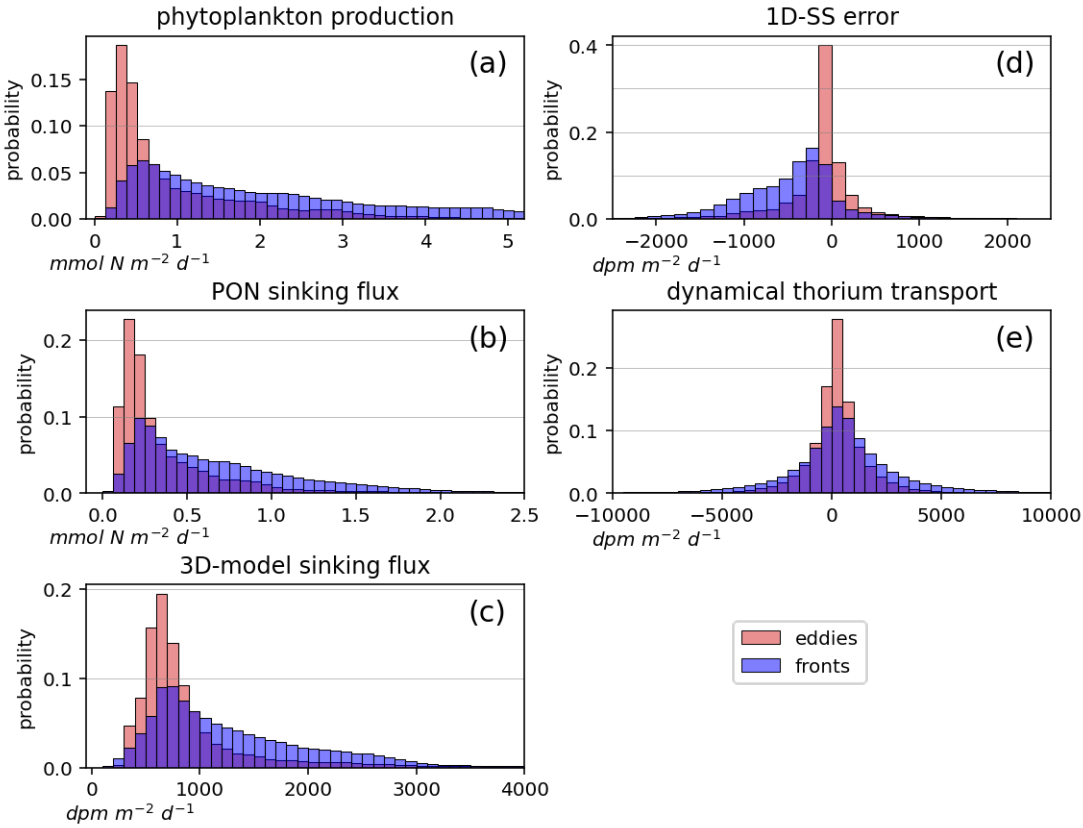


Figure 3.4: Probability density distribution inside eddies (blue) and fronts (red) of a) depth-integrated phytoplankton production, b) sinking particulate organic nitrogen (PON), c) sinking thorium flux, d) 1D-SS error (i.e. difference between 1D-SS sinking flux estimate and model ground truth sinking flux), e) and depth-integrated dynamical thorium transport. All sinking fluxes are shown at 427 m.

We calculate the ^{234}Th -based 1D-SS sinking flux estimate at every model grid point and time step, classifying each point as inside an eddy, inside a front, or neither. We find that the error in the 1D-SS sinking flux estimate generally exhibits a negative bias in all regions (80% of the time in eddies, 90% of the time in fronts, Fig. 3.4d), indicating that the 1D-SS estimate frequently underestimates the ground truth 3D-model sinking flux. However, the error associated with the 1D-SS estimate is smaller inside eddies (70% have er-

rors $< 250 \text{ dpm m}^{-2} \text{ d}^{-1}$), than in frontal regions (only 30% of fronts have errors $< 250 \text{ dpm m}^{-2} \text{ d}^{-1}$). The higher error in frontal regions is driven by the stronger dynamical transport of thorium (in 35% of fronts transport is more than twice the sinking flux) compared to eddies (in $> 80\%$ of eddies, dynamical transport is less than twice the sinking flux, Fig. 3.4e), consistent with the fact that the core of eddies tends to be coherent and experiences weaker advection. These results support the view that targeting and tracking an eddy center for sampling will likely help reduce the uncertainty in ^{234}Th sinking flux estimates than using random location and/or frontal regions.

3.3.2 LAGRANGIAN EDDY SAMPLING IMPROVES HIGH SINKING FLUX ESTIMATES

Because eddies are associated with lower dynamical transport of ^{234}Th (section 3.3.1), Lagrangian sampling along an eddy track sampling can be expected to result in more accurate 1D ^{234}Th estimates. To test this, we compute the 1D-SS and 1D-NSS-eddy errors along the track of every eddy lasting longer than 20 days and classify each according to which estimate provides a smaller error.

For example, eddy #144 located in the jet region at approximately 32° N , 285° W is a long lasting eddy (> 90 days) that captured a peak phytoplankton bloom on April 1st and the correlated peak thorium sinking flux shortly after (Fig. 3.3c, orange line). The 1D-SS estimated flux is lower than the 3D-model flux through the entire blooming period until it peaks in early May at $2200 \text{ dpm m}^{-2} \text{ d}^{-1}$ vs. an April 15 peak of the 3D-model flux at $3300 \text{ dpm m}^{-2} \text{ d}^{-1}$ (blue vs orange line on Fig. 3.3c). After the peak the 1D-SS model then consistently overestimates the sinking flux. In contrast, the 1D-NSS-eddy estimate (black line), provides a better estimate of the 3D-model flux, peaking in mid-April, but exhibit-

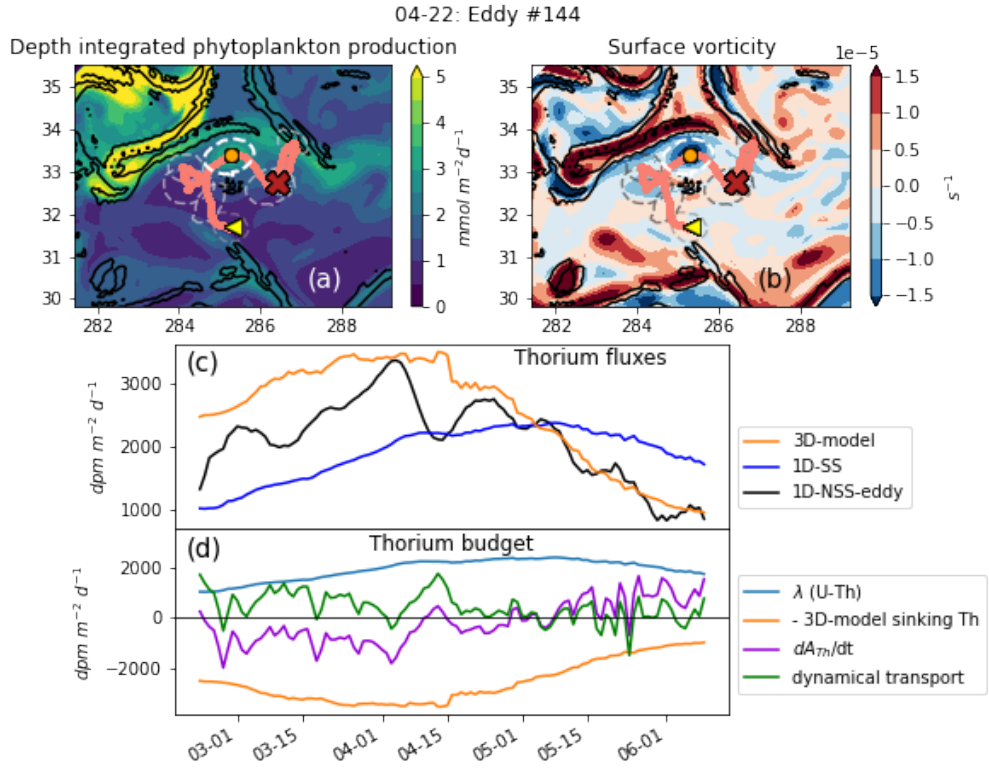


Figure 3.5: Example of an eddy trajectory (eddy #144) over field of a) phytoplankton production integrated to 427m and b) surface potential vorticity. Eddy trajectory in coral starts on Feb. 26 at yellow arrow and ends on Jun. 9 at red cross. Gray contours show evolution of eddy boundary at several timesteps. Black contours denote frontal regions defined by a strong SST gradient. c) evolution of thorium-derived sinking fluxes: the model ground truth (orange), 1D-SS (blue), and 1D-NSS (black). d) Modeled thorium budget terms from equation 1.

ing stronger variability driven by dynamical fluctuations (green line, panel d). Post-bloom, when the dynamical ^{234}Th transport is close to zero, the 1D-NSS-eddy model closely follows the 3D-model sinking flux. Integrated over the eddy lifetime, the root mean square error for the 1D-NSS-eddy is 22% of the mean sinking flux, a significant improvement over the 1D-SS error of > 45%. In this eddy, the dynamical transport of ^{234}Th (green line) remains well below both the sinking ^{234}Th and the ^{234}Th deficit terms, with the variability

and magnitude of the dynamical transport term driven by horizontal advection compensated by vertical advection (not shown).

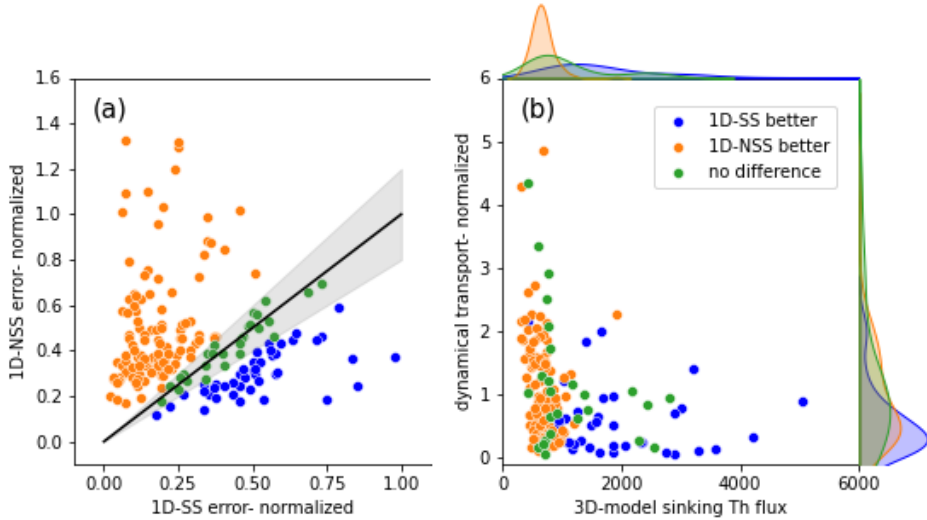


Figure 3.6: Classification of eddies based on their 1D-SS and 1D-NSS-eddy errors normalized to the 3D-model sinking flux (a). Eddy classification criteria. Eddies above the 1:1 line (black line, shading indicates 20% boundary) are designated as 1D-NSS is better (orange markers). Eddies below are designated as 1D-SS is better (blue markers). Eddies for which the relative errors are within 20% of each other are designated as no difference (green markers). (b) Eddy 3D-model sinking flux (probability density function top x-axis) vs. the standard deviation of their dynamical transport normalized to the 3D-model sinking flux (probability density function right y-axis).

We expand this analysis to all simulated eddies that last more than 20 days. This threshold was chosen to capture eddies that may have greater coherence than those that quickly dissipate. This analysis shows that the 1D-NSS-eddy estimate improves on the 1D-SS estimate in only about 30% of the 20-day eddies (61 out of 202 eddies, orange symbols in Fig. 3.6), while the 1D-SS estimate is better in 57% of eddies (116 out of 202, blue symbols in Fig. 3.6). The performance of the 1D-SS and 1D-NSS is similar in the remaining 25 eddies (less than 20% difference between the two estimates, green symbols in Fig. 3.6). The ed-

dies that we classify as improved by the 1D-NSS-eddy estimate are characterized by large 3D-model sinking fluxes ($> 1000 \text{ dpm m}^{-2} \text{ d}^{-1}$) and relatively low dynamical transport of ^{234}Th (standard deviation less than twice the 3D-model sinking flux). This demonstrates that in most cases, the simpler 1D-SS approach yields a more accurate estimation of the sinking flux, likely because the 1D-NSS-eddy method may incorrectly misclassify dynamic ^{234}Th transport as a temporal variation in sinking rates.

3.3.3 STRONG VERTICAL TRANSPORT IN FRONTAL REGIONS OBSCURES SINKING FLUX ESTIMATES

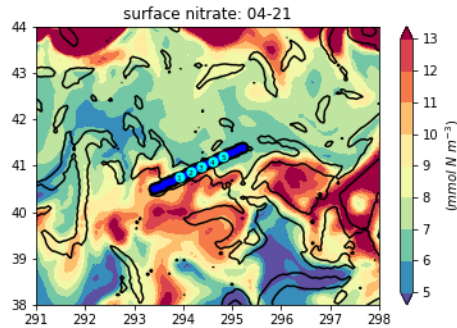


Figure 3.7: Transect location over model surface phytoplankton biomass (mmol N m^{-2}) in upper 15 m on April 21 with contours where SST gradient exceeds $0.15^\circ \text{C per cell}$. Transect shown as dark blue line, with profile sites denoted as numbered cyan dots.

Here, we use a case study approach to explore the impact of frontal dynamics on the 1D-SS thorium flux estimates. We do not consider the 1D-NSS estimate in this context because the transient nature of the front does not allow for meaningful tracking like in the eddy analysis in section 3.2. We sample across a front extending from $293.4^\circ - 295^\circ \text{ W}$ and $40.5^\circ - 41.3^\circ \text{ N}$ three weeks after the peak phytoplankton bloom, which occurred on April 1 (Fig. 3.7). At this time, nitrate has largely been depleted ($< 1 \text{ mmol m}^{-3}$) in the shallow surface mixed layer ($< 15 \text{ m}$, defined where) limiting phytoplankton growth. The region exhibits high spatial variability on scales of tens of kilometers. The northeastern side of the

front is characterized by high stratification and slightly lower phytoplankton biomass ($< 10 \text{ mmol m}^{-2}$) compared to the less stratified southwestern segment (12.5 mmol m^{-2}). We subsampled the model front at 5 locations similar to what could be done in the field (points 1-5, cyan dots), capturing small-scale vertical velocities of $>20 \text{ m d}^{-1}$ that vary from positive (upward) to negative (downward) over distances $< 7 \text{ km}$ (Fig. 3.8c & d).

These vertical velocities produce two competing effects. The first is the impact on primary production (Fig. 3.8a) and the associated influence on ^{234}Th and particle export (Fig. 8b). Positive, upwelling velocities (red arrows) at points p.1 and p.3 are correlated with relatively high surface phytoplankton ($> 6 \text{ mmol m}^{-2}$, green line Fig. 3.8a). The upward velocity brings higher concentrations of nitrate present in deeper waters up toward the surface, supporting increased production (Fig. 3.8c). The increased phytoplankton productivity drives higher POC and ^{234}Th sinking fluxes at these locations ($> 3700 \text{ dpm m}^{-2} \text{ d}^{-1}$, orange line, Fig. 3.8b). In contrast, negative or downwelling velocities at points p.2 and p.4 transport nitrate-depleted waters downward (panel c), limiting production at the surface (panel a). The phytoplankton concentration at these points (4.5 and 3 mmol m^{-2} , respectively) is notably lower than the neighboring points where vertical velocities are upward ($> 6 \text{ mmol m}^{-2}$) and is correlated with lower sinking ^{234}Th fluxes ($< 3000 \text{ dpm m}^{-2} \text{ d}^{-1}$, orange line, panel c).

The strong vertical velocities around the front have a second effect, acting on the dissolved ^{234}Th gradient and directly impacting the 1D ^{234}Th -derived flux estimates (Fig. 3.8b, Fig. 3.9f-j) via the dynamical transport term. Similar to the effect on nitrate, upward velocities at p.1 and p.3 bring high concentrations of dissolved ^{234}Th (Fig. 3.8d) from deep in the water column toward the surface. This transport of high ^{234}Th subsurface waters decreases

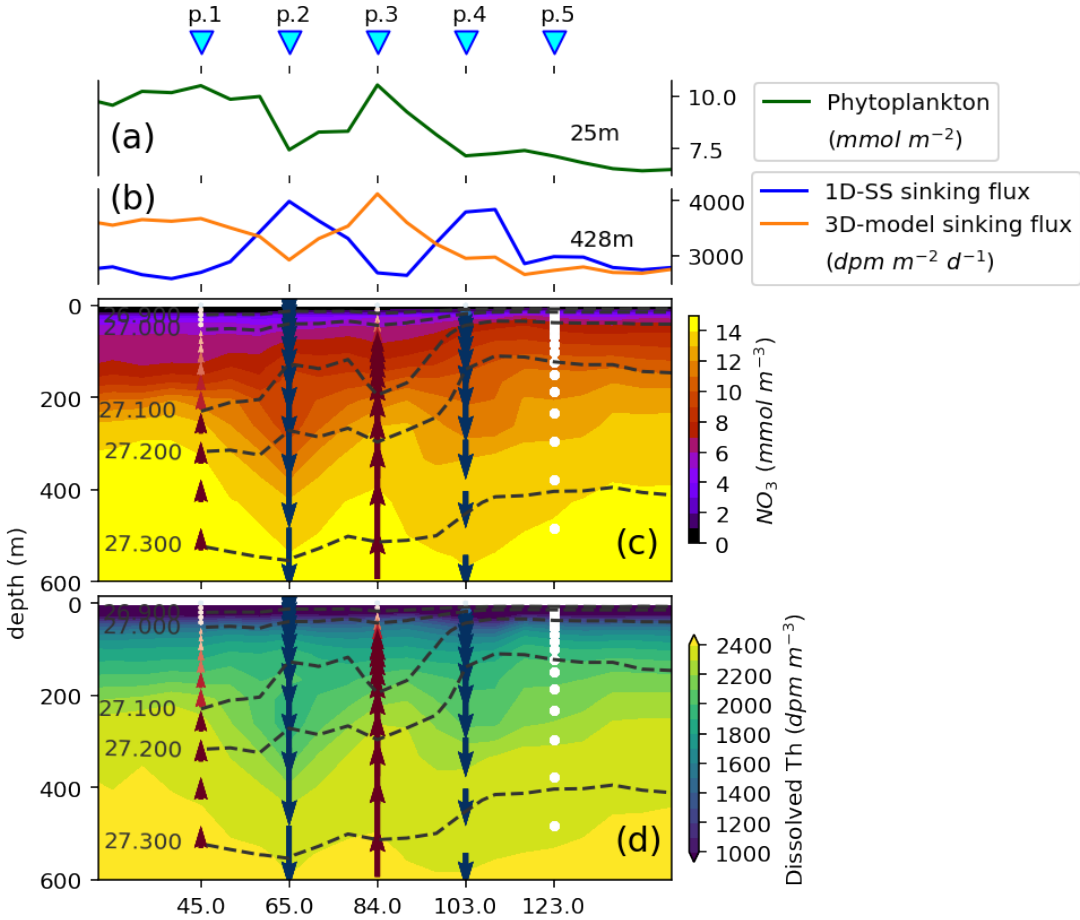


Figure 3.8: Transect sampling across a front, stations (cyan triangles) shown as p. 1-5. First panel (a) shows surface phytoplankton biomass concentrations as if sampled along the transect, with thorium sinking fluxes on the panel below (b). Next two panels show depth-dependent nitrate concentration (c) and dissolved thorium activity (d), overlaid with contours of potential density. Vertical velocities for the five-station profiles are shown as arrows with the intensity of the velocity denoted by both the size and color of the arrow.

the ^{234}Th to ^{238}U deficit in the upper ocean, with the equilibrium depth where ^{234}Th and uranium activities are equally moving to shallower depths (green line, Fig. 3.9a,c). This decrease in the ^{234}Th deficit is wrongly interpreted by the 1D-SS model as a low particle sinking flux (low $< 3000 \text{ dpm m}^{-2} \text{ d}^{-1}$ 1D-SS flux, blue line, relative to 3D-model sinking flux, orange line, Fig. 3.8b, Fig. 3.9f,h).

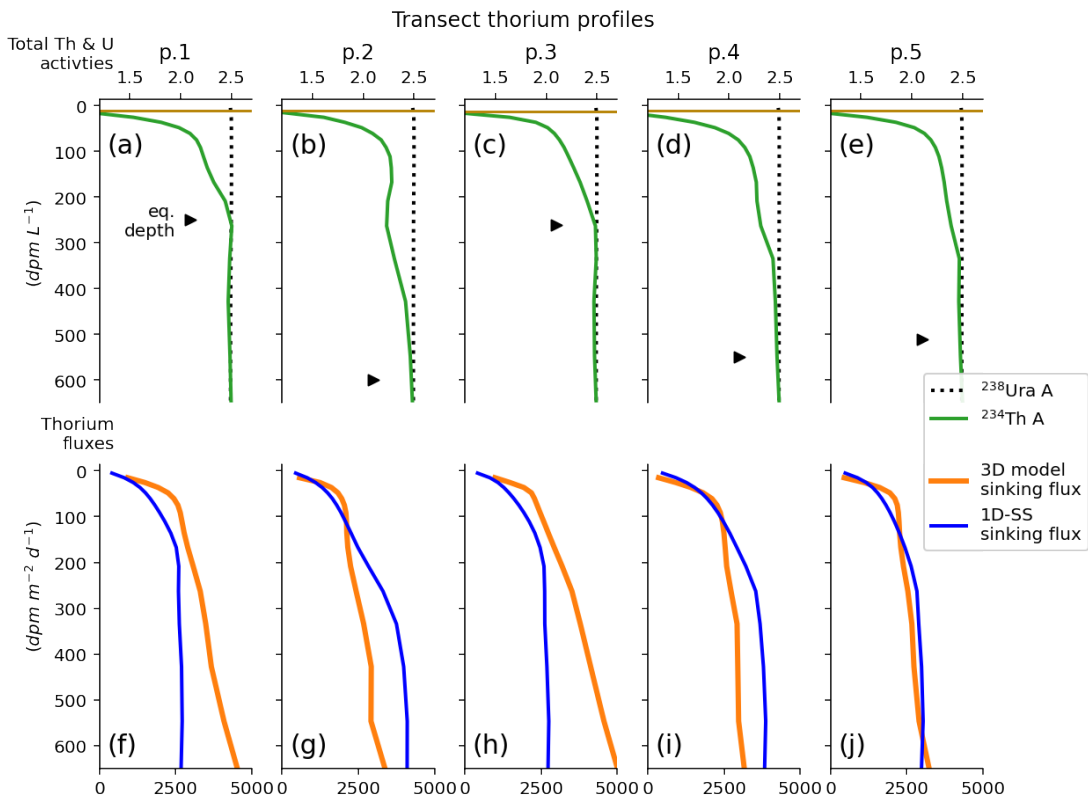


Figure 3.9: Profiles of sampling across a front, stations shown at the top as p. 1-5. a-e) ^{234}Th (green line) and ^{238}U (black line) radioactivity with the equilibrium depth (small black triangle) and mixed layer depth (yellow lines). f-j) 3D-model sinking flux (orange lines) and 1D-SS (blue line) sinking fluxes derived from ^{234}Th - ^{238}U disequilibrium.

In contrast, negative, downwelling velocities observed at points p.2 and p.4 (blue arrows, Fig. 3.8d) transport low ^{234}Th surface waters down the water column, creating a large ^{234}Th deficit that pushes the equilibrium depth deeper (green line, Fig. 3.9b,d). This again is misattributed to a change in the sinking flux, with the 1D-SS flux (orange line, Fig. 3.9b, Fig. 3.9g,i) exceeding the 3D-model sinking flux (blue line $4000 \text{ dpm m}^{-2} \text{ d}^{-1}$, Fig. 3.8b, Fig. 3.8g,i). While this is a case study approach, these results are consistent with the probability distributions in Figure 3.4, which show that frontal regions are associated with high dynamic ^{234}Th transport and large 1D-SS errors. Further, while this case study is focused

on the impact of vertical velocities and gradients, the dynamic transport thorium activity across

3.4 DISCUSSION

3.4.1 EFFICACY OF THE STEADY-STATE MODEL

Across the model domain, the 1D-SS estimate generally performs better than the 1D-NSS estimate, consistent with previous studies which have shown that the 1D-NSS estimate should be reserved for regions with high productivity, i.e. during phytoplankton blooms (Resplandy et al., 2012; Ceballos-Romero et al., 2018). In this work, we find similar results, adding the caveat that dynamical ^{234}Th transport must also be low for the most effective use of the 1D-NSS estimate. This suggests that the use of the 1D-NSS model should be reserved when the two conditions are met: (1) that sinking fluxes are large ($> 1000 \text{ dpm m}^{-2} \text{ d}^{-1}$) and (2) when dynamical ^{234}Th transport is small (less than twice the 3D model sinking flux). When these two conditions are not expected to be satisfied, e.g., in regions with low primary productivity or high in situ velocities, the 1D-SS estimate should be used.

When sampling an eddy, the 1D estimates can be performed in a Lagrangian framework, reducing 1D-SS errors and naturally providing an opportunity for a 1D-NSS-eddy calculation. Our results show that in eddies lasting 20 days or more, the 1D-NSS-eddy estimate is an improvement 25% of the time. In contrast, if we apply the 1D-NSS-eddy agnostically at any model grid point in the entire model domain, the 1D-NSS-eddy only improves on the 1D-SS estimate in <3% of cases. This is because eddies retain a coherent structure that results in a low dynamical ^{234}Th transport that can be sampled repeatedly over their lifespans.

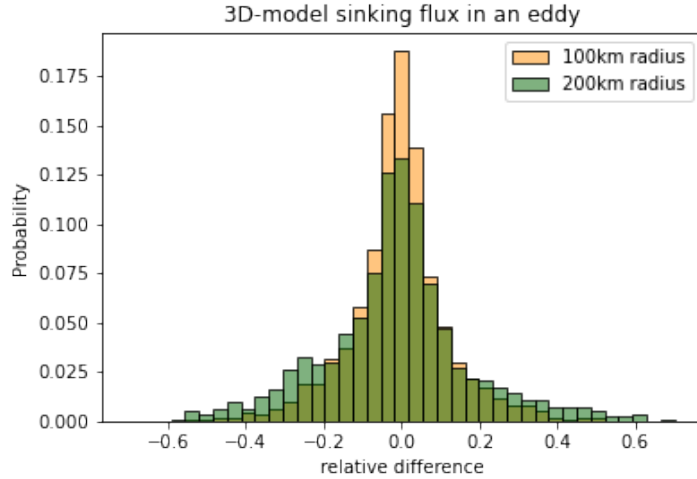


Figure 3.10: How representative are eddies of the flux surrounding them? Difference of the 3D-model thorium sinking flux inside each eddy vs. a 100 km (orange) and 200 km (green) radius around it, relative to the magnitude of the 3D-model sinking flux.

Eddies can provide a naturally low transport setting but are they representative of the surrounding areas? Figure 3.10 shows that for 74% of the eddies, the average sinking ^{234}Th flux found inside the eddy is representative within 20% of the mean flux in a 200 km radius (For a 100 km radius 90% of eddies meet the 20% threshold). This suggests that targeting eddies for ^{234}Th sampling could be an effective way to estimate sinking fluxes in situ, producing smaller errors when using the 1D-SS or the 1D-NSS to capture high sinking fluxes.

These findings are constrained, however, by the limitations of the model. For example, model vertical resolution may not fully resolve the submesoscale dynamics examined in this study. Here, the magnitude of the vertical velocities in our case study (20 m d^{-1}) is smaller than submesoscale-induced velocities in other studies (up to 100 m d^{-1} , e.g. Thomas et al., 2008; Siegelman et al., 2020). The simplified ecosystem dynamics of our model (one phytoplankton, one zooplankton, two sinking detritus classes) and simple mesopelagic rep-

resentation (constant sinking rates, no explicit bacteria class) may also limit the magnitude and variability of the 3D model sinking fluxes. Additionally, our eddy and front detection methods were applied across a large domain, which may limit their ability to categorize more nuanced and transient structures that are likely associated with even larger dynamics.

3.4.2 SYSTEMATIC UNDERESTIMATION OF SINKING FLUXES USING THE 1D-SS ESTIMATE

We see that across eddies, fronts, and the entire model domain, the 1D-SS estimate is more often lower than the 3D-model sinking flux (distribution of 1D-SS errors is skewed negative, Fig. 3.4d), with the bias especially pronounced across frontal regions (blue bars, Fig. 3.4d). Integrated over the entire model domain, the 1D-SS estimate results in a 20–35% lower than the 3D-model sinking flux at depths shallower than 1000 m. This is likely caused by two factors: (1) the 1D-SS estimate systematically underestimates fluxes during the first part of the spring phytoplankton bloom, and (2) the dynamical transport of ^{234}Th , especially in the vicinity of fronts, causes a net increase in ^{234}Th activity resulting in lower 1D-SS estimates.

The first factor has been discussed in previous work (Resplandy et al., 2012; Ceballos-Romero et al., 2018). These studies have shown that during the growth phase and peak phytoplankton bloom, the 1D-SS estimate is systematically lower than the true sinking fluxes, underestimating the true sinking flux, and shortly after the peak bloom, the 1D-SS estimate systematically overestimates the true sinking fluxes. This is because ^{234}Th integrates over a time scale as a function of its half-life and removal time scale (Turnewitsch and Springer, 2001). Thus, 1D-SS estimates lag the 3D-model sinking flux when it changes over short time scales. However, integrated over the entire bloom period, the underestimation

pre-bloom peak exceeds the overestimation post-peak, resulting in an estimated sinking flux that is 20-35% lower when integrated over the entire model domain. Post-bloom, the bias of the SS estimate shifts to consistently overestimating the sinking flux.

The second reason for the bias is that dynamical transport across frontal boundaries results in a net addition of ^{234}Th activity. This is because high ^{234}Th water is transported down-gradient toward the surface by upward velocities, while low- ^{234}Th water is moved deeper by downward velocities, as seen in the case study (Fig. 3.8). Despite compensation by the vertical velocities, the upward flux is greater because sinking particles reinforce the ^{234}Th gradient. This is a comparable effect to that observed on the nutrient field near fronts (e.g. McGillicuddy, 2016; Mahadevan, 2016). Thus, considering phytoplankton bloom timing and some characterization of the velocity field that drives dynamic transport can suggest whether observations will likely have this systematic bias, leading to an underestimation of true sinking fluxes.

3.4.3 FRONTAL DYNAMICS MAY INHIBIT THE INTERPRETATION OF SINKING FLUXES

It has been shown in the literature that small-scale vertical velocities can act across nutrient gradients, supplying nutrients that stimulate local surface phytoplankton production (Omand et al., 2015; Levy et al., 2018). In our case study, the front is studded with deep (> 1000 m) and persistent (> 1 month) small-scale velocities associated with upwelling and downwelling of nitrate and corresponding increases and decreases in phytoplankton biomass across the transect. The change in biomass triggers comparable changes in the ^{234}Th sinking flux as increased phytoplankton enhance the generation of sinking particles on which ^{234}Th adsorbs.

We show here that the dissolved ^{234}Th is subject to the same small-scale upwelling/downwelling as the nutrient field, leading to biases in the SS estimated flux. As ^{234}Th activity is generally low in the surface and increases with depth (e.g. Fig. 3.9a–e), vertical velocities can act across this gradient to increase (downward velocities) or decrease (upward velocities) the ^{234}Th - ^{238}U deficit. This shifts the apparent equilibrium depth (Fig. 3.9f–j), leading to a decoupling of the 1D estimate from the ground truth sinking ^{234}Th flux (3D-model flux). Here, the true sinking flux increases near upwelling velocities due to the stimulation of phytoplankton production, which produces sinking particles. Meanwhile, the SS estimate decreases due to the same upward velocity bringing high ^{234}Th water toward the surface, reducing the ^{234}Th deficit. Near downwelling velocities, the reverse is true: phytoplankton production is inhibited, and the sinking fluxes decrease while the 1D-SS estimate increases due to the downward movement of low ^{234}Th water from the surface. While this case study is an example that includes phytoplankton growth, which is easily stimulated by additional nitrate, during periods when phytoplankton are less sensitive to nutrient injection, e.g. after deep winter convection when nitrate is abundant, there may still be a decoupling between the 1D-SS estimate and the true sinking ^{234}Th flux due to the impact on the ^{234}Th gradient alone.

These changes in the 1D-SS estimate and sinking flux can also affect the known systematic bias of the SS estimate in highly productive regions (see section 3.4.2). The 1D-SS estimate has been shown to have a systematic bias during (negative bias) and after (positive bias) phytoplankton blooms (Resplandy et al., 2012; Ceballos-Romero et al., 2018) and discussed in section 4.2. During the transition window between those two regimes, ranging from 10 days before to 60 days after peak bloom, depending on bloom duration (Cebal-

los-Romero et al., 2018), submesoscale vertical velocities can alter the direction and magnitude of the 1D-SS bias, as seen in this case study.

However, during the phytoplankton bloom growth phase, when the 1D-SS is systematically lower than ground truth sinking fluxes, upward velocities that transport high ^{234}Th water toward the surface would exacerbate this negative bias by making the 1D estimated fluxes smaller. Whereas, downward velocities during this phase increase the observed ^{234}Th deficit, bringing the 1D estimated flux closer to the true sinking flux, reducing the systematic negative bias.

3.5 CONCLUSIONS

This work finds that fine-scale dynamics can act across ^{234}Th gradients to transport ^{234}Th three-dimensionally, for example, causing higher 1D estimated fluxes when ^{234}Th -depleted water is transported into the observed water column, making the ^{234}Th deficit appear larger than that which can be attributed to sinking particles only. Dynamical ^{234}Th transport, however, is generally lower in eddies, resulting in smaller differences between the 1D estimates and 3D-model sinking flux. Eddies can be tracked, and sampling can occur in a Lagrangian framework that also allows for a 1D-NSS-eddy estimated flux, which improves on the 1D-SS model when fluxes are large ($> 1000 \text{ dpm L}^{-1}$), and dynamics are relatively low (< 2 times the sinking flux). This result holds in general, i.e. the 1D-NSS estimate should be reserved for use during phytoplankton blooms where dynamical ^{234}Th transport is low, otherwise the 1D-SS provides more accurate estimates that do not conflate physical transport with temporal changes in ^{234}Th . Finally, we demonstrate that fronts, which are associated with large dynamical physical transport and large 1D-SS errors, can create large vertical

velocities that decouple the 1D estimate from the 3D-model sinking flux, suggesting that interpretation of fluxes in these regions should be approached cautiously.

*No. I can't give you full credit, but I'm not gonna flunk
you either. You're all getting incompletes.*

—Steve Zissou

4

Conclusion

This thesis builds on the NASA EXport Processes in the Ocean from Remote Sensing (EXPORTS) program, a large-scale sampling campaign designed to constrain estimates of the biological carbon pump and the processes that control it by using high-resolution datasets characterizing the biological pump in two export regimes: the low eddy kinetic energy and low export efficiency of the Northeast Pacific and the highly eddying, highly productive

North Atlantic. This dissertation examines interannual variability in the low export regime near Ocean Station Papa (OSP) in the Northeast Pacific in Chapter 1. The latter half of this dissertation examines the spatial and temporal variability of sinking particle fluxes derived from the export proxy, Thorium-234 (^{234}Th). The collection and analysis of in situ data from OSP and the North Atlantic porcupine abyssal plain (PAP) are presented in Chapter 2. While a more generalized analysis of the impact of fine-scale dynamics on ^{234}Th -derived sinking fluxes using a biogeochemical coupled double gyre model that resolves eddies and fronts is covered in Chapter 3.

Throughout this dissertation, my work is a unique combination of observational methods/datasets and general circulation models, that leverages the complementary strengths and limitations of each. Observations, which capture snapshots of in situ biological carbon pump (BCP) activity in space and time, can be difficult to interpret due to the lack of full spatial and temporal context that requires assumptions of convenience, e.g. the neglect of physical tracer transport in 1D models. In contrast, 3D ocean biogeochemical models give us the ability to test the interplay of mechanisms and processes controlling the BCP, but are based on our limited understanding and assumptions of the BCP and do not reproduce the full complexity of the ocean and climate systems. While the focus of my work is modeling, having contributed to the shipboard collection of nearly 1000 ^{234}Th samples during the Northeast Pacific cruise and the subsequent processing and analysis thereafter, I have been able to combine complementary expertise in model and observational data processing to produce quantitative analyses of ecosystem and particle flux variabilities.

For example, one method employed frequently in this dissertation is the subsampling of model output using observational sampling patterns, allowing me to test the associated

biases. In Chapter 1, I applied this technique to Argo float trajectories, revealing that past work misinterpreted a large-scale spatial gradient as an interannual anomaly during the 2014-2015 marine heatwave and wrongly concluded that the ecosystem near OSP had collapsed in response to the prolonged nature of the event. In revealing this bias, I showed that the ecosystem response was more subtle, with likely a smaller decrease in primary production, and a shift in the size-class distribution of the phytoplankton assemblage toward smaller phytoplankton. In Chapter 2, I subsampled the same model with station location and timing from the 2018 NASA EXPORTS cruise. This time, my analysis suggested that the observed change in sinking fluxes between two sampling epochs was attributable to temporal variability rather than a mesoscale spatial gradient. Then I tested sampling strategies near eddies and fronts to understand how fine-scale variability impacts in situ estimates of sinking fluxes.

Overall, this thesis addresses and quantifies multiple scales of variability that affect the BCP, from the interannual ecosystem dynamics at OSP to the impact of fine-scale physical dynamics, including those induced by fronts and eddies on ^{234}Th -based estimates of particle fluxes. Understanding the variability of the BCP allows for an improved representation and quantification of the processes that control it, which in turn helps constrain the uncertainty around estimates of the global BCP.

This work primarily focuses on only two regions of the ocean, whereas accurate accounting of the global BCP would require analyses in other regions of the ocean, including additional large-scale sampling campaigns like NASA EXPORTS, which require intense coordination and planning. Further, most of this analysis is constrained to the near-surface (< 500 m) ocean, where observations are more plentiful, and models can reliably simulate

bio-physical interactions. Below this region, more work is needed to address how physical dynamics and biological processes mediate the downward transport of organic matter. Finally, given the importance of the BCP to the global carbon budget and the importance of primary productivity to economic concerns like fisheries, the looming question is: how will the processes controlling the BCP evolve in response to anthropogenic carbon emissions? Current projections of the BCP disagree on whether the global carbon flux will increase or decrease in the future, highlighting a need to better represent the various pathways of the BCP in global models. Thus, more effort will be needed to synthesize observational data and validate observational techniques in order to enhance our data interpretation and deepen our understanding of BCP mechanisms.

References

- [1] Abernathey, R. & Haller, G. (2018). Transport by lagrangian vortices in the eastern pacific. *Journal of Physical Oceanography*, 48(3), 667–685.
- [2] Adcroft, A., Anderson, W., Balaji, V., Blanton, C., Bushuk, M., Dufour, C. O., Dunne, J. P., Griffies, S. M., Hallberg, R., Harrison, M. J., et al. (2019). The gfdl global ocean and sea ice model om4. 0: Model description and simulation features. *Journal of Advances in Modeling Earth Systems*, 11(10), 3167–3211.
- [3] Alldredge, A. L. & Silver, M. W. (1988). Characteristics, dynamics and significance of marine snow. *Progress in oceanography*, 20(1), 41–82.
- [4] Amaya, D. J., Alexander, M. A., Capotondi, A., Deser, C., Karnauskas, K. B., Miller, A. J., & Mantua, N. J. (2021). Are long-term changes in mixed layer depth influencing north pacific marine heatwaves? *Bulletin of the American Meteorological Society*, 102(1), S59–S66.
- [5] Archer, D. E., Eshel, G., Winguth, A., Broecker, W., Pierrehumbert, R., Tobis, M., & Jacob, R. (2000). Atmospheric pco₂ sensitivity to the biological pump in the ocean. *Global Biogeochemical Cycles*, 14(4), 1219–1230.
- [6] Aumont, O., Maier-Reimer, E., Blain, S., & Monfray, P. (2003). An ecosystem model of the global ocean including fe, si, p colimitations. *Global Biogeochemical Cycles*, 17(2).
- [7] Ayers, J. M. & Lozier, M. S. (2010). Physical controls on the seasonal migration of the north pacific transition zone chlorophyll front. *Journal of Geophysical Research: Oceans*, 115(C5).
- [8] Baker, C. A., Estapa, M. L., Iversen, M., Lampitt, R., & Buesseler, K. (2020). Are all sediment traps created equal? an intercomparison study of carbon export methodologies at the pap-so site. *Progress in Oceanography*, 184, 102317.
- [9] Baumann, M., Paul, A. J., Taucher, J., Bach, L. T., Goldenberg, S., Stange, P., Minutolo, F., & Riebe-sell, U. (2023). Drivers of particle sinking velocities in the peruvian upwelling system. *Biogeosciences*, 20(13), 2595–2612.
- [10] Benitez-Nelson, C., Buesseler, K. O., Karl, D. M., & Andrews, J. (2001). A time-series study of particulate matter export in the north pacific subtropical gyre based on 234th: 238u disequilibrium. *Deep Sea Research Part I: Oceanographic Research Papers*, 48(12), 2595–2611.
- [11] Benitez-Nelson, C. R., Bidigare, R. R., Dickey, T. D., Landry, M. R., Leonard, C. L., Brown, S. L., Nencioli, F., Rii, Y. M., Maiti, K., Becker, J. W., et al. (2007). Mesoscale eddies drive increased silica export in the subtropical pacific ocean. *Science*, 316(5827), 1017–1021.

- [12] Bif, M. B. & Hansell, D. A. (2019). Seasonality of dissolved organic carbon in the upper northeast pacific ocean. *Global Biogeochemical Cycles*, 33(5), 526–539.
- [13] Bif, M. B., Siqueira, L., & Hansell, D. A. (2019). Warm events induce loss of resilience in organic carbon production in the northeast pacific ocean. *Global Biogeochemical Cycles*, 33(9), 1174–1186.
- [14] Bograd, S. J., Foley, D. G., Schwinger, F. B., Wilson, C., Laurs, R. M., Polovina, J. J., Howell, E. A., & Brainard, R. E. (2004). On the seasonal and interannual migrations of the transition zone chlorophyll front. *Geophysical Research Letters*, 31(17).
- [15] Bond, N. A., Cronin, M. F., Freeland, H., & Mantua, N. (2015). Causes and impacts of the 2014 warm anomaly in the ne pacific. *Geophysical Research Letters*, 42(9), 3414–3420.
- [16] Boyd, P. & Harrison, P. (1999). Phytoplankton dynamics in the ne subarctic pacific. *Deep Sea Research Part II: Topical Studies in Oceanography*, 46(11-12), 2405–2432.
- [17] Boyd, P. W., Claustre, H., Levy, M., Siegel, D. A., & Weber, T. (2019). Multi-faceted particle pumps drive carbon sequestration in the ocean. *Nature*, 568(7752), 327–335.
- [18] Boyd, P. W., Law, C. S., Wong, C., Nojiri, Y., Tsuda, A., Levasseur, M., Takeda, S., Rivkin, R., Harrison, P. J., Strzepek, R., et al. (2004). The decline and fate of an iron-induced subarctic phytoplankton bloom. *Nature*, 428(6982), 549–553.
- [19] Boyer, T. P., Antonov, J. I., Baranova, O. K., Garcia, H. E., Johnson, D. R., Mishonov, A. V., O'Brien, T. D., Seidov, D., Smolyar, I., Zweng, M. M., et al. (2013). World ocean database 2013.
- [20] Brand, L. E., Guillard, R. R., & Murphy, L. S. (1981). A method for the rapid and precise determination of acclimated phytoplankton reproduction rates. *Journal of plankton research*, 3(2), 193–201.
- [21] Buesseler, K. O. (1998). The decoupling of production and particulate export in the surface ocean. *Global Biogeochemical Cycles*, 12(2), 297–310.
- [22] Buesseler, K. O., Benitez-Nelson, C. R., Roca-Martí, M., Wyatt, A. M., Resplandy, L., Clevenger, S. J., Drysdale, J. A., Estapa, M. L., Pike, S., & Umhau, B. P. (2020). High-resolution spatial and temporal measurements of particulate organic carbon flux using thorium-234 in the northeast pacific ocean during the export processes in the ocean from remote sensing field campaign. *Elem Sci Anth*, 8(1), 030.
- [23] Buesseler, K. O. & Boyd, P. W. (2009). Shedding light on processes that control particle export and flux attenuation in the twilight zone of the open ocean. *Limnology and Oceanography*, 54(4), 1210–1232.
- [24] Buesseler, K. O., Lamborg, C., Cai, P., Escoube, R., Johnson, R., Pike, S., Masque, P., McGillicuddy, D., & Verdeny, E. (2008). Particle fluxes associated with mesoscale eddies in the sargasso sea. *Deep Sea Research Part II: Topical Studies in Oceanography*, 55(10-13), 1426–1444.
- [25] Buesseler, K. O., Lamborg, C. H., Boyd, P. W., Lam, P. J., Trull, T. W., Bidigare, R. R., Bishop, J. K., Casciotti, K. L., Dehairs, F., Elskens, M., et al. (2007). Revisiting carbon flux through the ocean's twilight zone. *science*, 316(5824), 567–570.
- [26] Buesseler, K. O., Pike, S., Maiti, K., Lamborg, C. H., Siegel, D. A., & Trull, T. W. (2009). Thorium-234 as a tracer of spatial, temporal and vertical variability in particle flux in the north pacific. *Deep Sea Research Part I: Oceanographic Research Papers*, 56(7), 1143–1167.

- [27] Cael, B. & Bisson, K. (2018). Particle flux parameterizations: Quantitative and mechanistic similarities and differences. *Frontiers in Marine Science*, 5, 395.
- [28] Ceballos-Romero, E., Buesseler, K. O., & Villa-Alfageme, M. (2021). Revisiting five decades of ^{234}Th data: a comprehensive global oceanic compilation. *Earth System Science Data Discussions*, 2021, 1–64.
- [29] Ceballos-Romero, E., De Soto, F., Le Moigne, F. A., García-Tenorio, R., & Villa-Alfageme, M. (2018). ^{234}Th -derived particle fluxes and seasonal variability: When is the ss assumption reliable? insights from a novel approach for carbon flux simulation. *Geophysical Research Letters*, 45(24), 13–414.
- [30] Chai, F., Jiang, M., Barber, R. T., Dugdale, R. C., & Chao, Y. (2003). Interdecadal variation of the transition zone chlorophyll front: A physical-biological model simulation between 1960 and 1990. *Journal of Oceanography*, 59, 461–475.
- [31] Charette, M. A., Moran, S. B., & Bishop, J. K. (1999). ^{234}Th as a tracer of particulate organic carbon export in the subarctic northeast pacific ocean. *Deep Sea Research Part II: Topical Studies in Oceanography*, 46(11-12), 2833–2861.
- [32] Chelton, D. B., Schlax, M. G., & Samelson, R. M. (2011). Global observations of nonlinear mesoscale eddies. *Progress in oceanography*, 91(2), 167–216.
- [33] Chen, J., Edwards, R. L., & Wasserburg, G. J. (1986). ^{238}U , ^{234}U and ^{232}Th in seawater. *Earth and Planetary Science Letters*, 80(3-4), 241–251.
- [34] Clevenger, S. J., Benitez-Nelson, C. R., Drysdale, J., Pike, S., Puigcorbé, V., & Buesseler, K. O. (2021). Review of the analysis of ^{234}Th in small volume (2–4 l) seawater samples: improvements and recommendations. *Journal of Radioanalytical and Nuclear Chemistry*, 329(1), 1–13.
- [35] Clevenger, S. J., Benitez-Nelson, C. R., Roca-Martí, M., Bam, W., Estapa, M., Kenyon, J. A., Pike, S., Resplandy, L., Wyatt, A., & Buesseler, K. O. (2024). Carbon and silica fluxes during a declining north atlantic spring bloom as part of the exports program. *Marine Chemistry*, 258, 104346.
- [36] CS, W. (1999). Seasonal and interannual variability in particle fluxes of carbon, nitrogen and silicon from time series of sediment traps at ocean station p, 1982-1993: relationship to changes in subarctic primary productivity. *Deep Sea Res II*, 46, 2735–2760.
- [37] Damerell, G. M., Heywood, K. J., Thompson, A. F., Binetti, U., & Kaiser, J. (2016). The vertical structure of upper ocean variability at the porcupine abyssal plain during 2012–2013. *Journal of Geophysical Research: Oceans*, 121(5), 3075–3089.
- [38] Delepoulle, A., evanmason, Clément, CoriPegliasco, Capet, A., Troupin, C., & Koldunov, N. (2022). Antsimi/py-eddy-tracker: v3.6.1.
- [39] DeVries, T., Primeau, F., & Deutsch, C. (2012). The sequestration efficiency of the biological pump. *Geophysical Research Letters*, 39(13).
- [40] DeVries, T. & Weber, T. (2017). The export and fate of organic matter in the ocean: New constraints from combining satellite and oceanographic tracer observations. *Global Biogeochemical Cycles*, 31(3), 535–555.
- [41] Di Lorenzo, E. & Mantua, N. (2016). Multi-year persistence of the 2014/15 north pacific marine heatwave. *Nature Climate Change*, 6(11), 1042–1047.
- [42] Droop, M. R. (1983). 25 years of algal growth kinetics a personal view.

- [43] Dugdale, R. & Goering, J. (1967). Uptake of new and regenerated forms of nitrogen in primary productivity 1. *Limnology and oceanography*, 12(2), 196–206.
- [44] Dunne, J. P., John, J. G., Adcroft, A. J., Griffies, S. M., Hallberg, R. W., Shevliakova, E., Stouffer, R. J., Cooke, W., Dunne, K. A., Harrison, M. J., et al. (2012). Gfdl's esm2 global coupled climate–carbon earth system models. part i: Physical formulation and baseline simulation characteristics. *Journal of climate*, 25(19), 6646–6665.
- [45] Emerson, S. (2014). Annual net community production and the biological carbon flux in the ocean. *Global Biogeochemical Cycles*, 28(1), 14–28.
- [46] Erickson, Z. K., Fields, E., Johnson, L., Thompson, A. F., Dove, L. A., D'Asaro, E., & Siegel, D. A. (2023). Eddy tracking from in situ and satellite observations. *Journal of Geophysical Research: Oceans*, 128(8), e2023JC019701.
- [47] Erickson, Z. K. & Thompson, A. F. (2018). The seasonality of physically driven export at submesoscales in the northeast atlantic ocean. *Global Biogeochemical Cycles*, 32(8), 1144–1162.
- [48] Erickson, Z. K., Thompson, A. F., Callies, J., Yu, X., Garabato, A. N., & Klein, P. (2020). The vertical structure of open-ocean submesoscale variability during a full seasonal cycle. *Journal of Physical Oceanography*, 50(1), 145–160.
- [49] Estapa, M., Buesseler, K., Durkin, C. A., Omand, M., Benitez-Nelson, C. R., Roca-Martí, M., Breves, E., Kelly, R., & Pike, S. (2021). Biogenic sinking particle fluxes and sediment trap collection efficiency at ocean station papa. *Elem Sci Anth*, 9(1), 00122.
- [50] Estapa, M., Siegel, D., Buesseler, K., Stanley, R., Lomas, M., & Nelson, N. (2015). Decoupling of net community and export production on submesoscales in the sargasso sea. *Global Biogeochemical Cycles*, 29(8), 1266–1282.
- [51] Estapa, M., Valdes, J., Tradd, K., Sugar, J., Omand, M., & Buesseler, K. (2020). The neutrally buoyant sediment trap: Two decades of progress. *Journal of Atmospheric and Oceanic Technology*, 37(6), 957–973.
- [52] Fassbender, A. J., Sabine, C. L., & Cronin, M. F. (2016). Net community production and calcification from 7 years of noaa station papa mooring measurements. *Global Biogeochemical Cycles*, 30(2), 250–267.
- [53] Freeland, H. (2007). A short history of ocean station papa and line p. *Progress in Oceanography*, 75(2), 120–125.
- [54] Freeland, H. & Whitney, F. (2014). Unusual warming in the gulf of alaska. *PICES press*, 22(2), 51.
- [55] Freilich, M. & Mahadevan, A. (2021). Coherent pathways for subduction from the surface mixed layer at ocean fronts. *Journal of Geophysical Research: Oceans*, 126(5), e2020JC017042.
- [56] Freilich, M. A. & Mahadevan, A. (2019). Decomposition of vertical velocity for nutrient transport in the upper ocean. *Journal of Physical Oceanography*, 49(6), 1561–1575.
- [57] Frölicher, T. L. & Laufkötter, C. (2018). Emerging risks from marine heat waves. *Nature communications*, 9(1), 650.
- [58] Garçon, V. C., Oschlies, A., Doney, S. C., McGillicuddy, D., & Waniek, J. (2001). The role of mesoscale variability on plankton dynamics in the north atlantic. *Deep Sea Research Part II: Topical Studies in Oceanography*, 48(10), 2199–2226.

- [59] Geider, R., MacIntyre, H., & Kana, T. (1997). Dynamic model of phytoplankton growth and acclimation: responses of the balanced growth rate and the chlorophyll a: carbon ratio to light, nutrient-limitation and temperature. *Marine Ecology Progress Series*, 148, 187–200.
- [60] Giamalaki, K., Beaulieu, C., Henson, S., Martin, A., Kassem, H., & Faranda, D. (2021). Future intensification of extreme aleutian low events and their climate impacts. *Scientific reports*, 11(1), 18395.
- [61] Giering, S., Sanders, R., Martin, A., Lindemann, C., Möller, K., Daniels, C., Mayor, D., & St. John, M. (2016). High export via small particles before the onset of the north atlantic spring bloom. *Journal of Geophysical Research: Oceans*, 121(9), 6929–6945.
- [62] globcolour (2020). (<http://globcolour.info>) used in this study has been developed, validated, and distributed by ACRI-ST, France. Last accessed 10/29/2020.
- [63] Gloege, L., McKinley, G. A., Mouw, C. B., & Ciochetto, A. B. (2017). Global evaluation of particulate organic carbon flux parameterizations and implications for atmospheric pco₂. *Global Biogeochemical Cycles*, 31(7), 1192–1215.
- [64] Glover, D. M., Wroblewski, J., & McClain, C. R. (1994). Dynamics of the transition zone in coastal zone color scanner-sensed ocean color in the north pacific during oceanographic spring. *Journal of Geophysical Research: Oceans*, 99(C4), 7501–7511.
- [65] Goes, J. I., do R. Gomes, H., Limsakul, A., & Saino, T. (2004). The influence of large-scale environmental changes on carbon export in the north pacific ocean using satellite and shipboard data. *Deep Sea Research Part II: Topical Studies in Oceanography*, 51(1-3), 247–279.
- [66] Haëck, C., Lévy, M., Mangolte, I., & Bopp, L. (2023). Satellite data reveal earlier and stronger phytoplankton blooms over fronts in the gulf stream region. *Biogeosciences*, 20(9), 1741–1758.
- [67] Harrison, P. J. (2002). Station papa time series: Insights into ecosystem dynamics. *Journal of Oceanography*, 58, 259–264.
- [68] Hartman, S. E., Bett, B. J., Durden, J. M., Henson, S. A., Iversen, M., Jeffreys, R. M., Horton, T., Lampitt, R., & Gates, A. R. (2021). Enduring science: three decades of observing the northeast atlantic from the porcupine abyssal plain sustained observatory (pap-so). *Progress in Oceanography*, 191, 102508.
- [69] Haskell, W., Fassbender, A., Long, J., & Plant, J. (2020). Annual net community production of particulate and dissolved organic carbon from a decade of biogeochemical profiling float observations in the northeast pacific. *Global Biogeochemical Cycles*, 34(10), e2020GB006599.
- [70] Henson, S. A., Dunne, J. P., & Sarmiento, J. L. (2009). Decadal variability in north atlantic phytoplankton blooms. *Journal of Geophysical Research: Oceans*, 114(C4).
- [71] Henson, S. A., Sanders, R., Madsen, E., Morris, P. J., Le Moigne, F., & Quartly, G. D. (2011). A reduced estimate of the strength of the ocean's biological carbon pump. *Geophysical Research Letters*, 38(4).
- [72] Honjo, S. & Manganini, S. J. (1993). Annual biogenic particle fluxes to the interior of the north atlantic ocean; studied at 34 n 21 w and 48 n 21 w. *Deep Sea Research Part II: Topical Studies in Oceanography*, 40(1-2), 587–607.

- [73] Huang, B., Banzon, V. F., Freeman, E., Lawrimore, J., Liu, W., Peterson, T. C., Smith, T. M., Thorne, P. W., Woodruff, S. D., & Zhang, H.-M. (2015). Extended reconstructed sea surface temperature version 4 (ersst. v4). part i: Upgrades and intercomparisons. *Journal of climate*, 28(3), 911–930.
- [74] Johnson, L., Siegel, D. A., Thompson, A. F., Fields, E., Erickson, Z. K., Cetinic, I., Lee, C. M., D'Asaro, E. A., Nelson, N. B., Omand, M. M., et al. (2024). Assessment of oceanographic conditions during the north atlantic export processes in the ocean from remote sensing (exports) field campaign. *Progress in Oceanography*, 220, 103170.
- [75] Karl, D., Christian, J., Dore, J., Hebel, D., Letelier, R., Tupas, L., & Winn, C. (1996). Seasonal and interannual variability in primary production and particle flux at station aloha. *Deep Sea Research Part II: Topical Studies in Oceanography*, 43(2-3), 539–568.
- [76] Khatiwala, S., Tanhua, T., Mikaloff Fletcher, S., Gerber, M., Doney, S. C., Graven, H. D., Gruber, N., McKinley, G., Murata, A., Ríos, A., et al. (2013). Global ocean storage of anthropogenic carbon. *Biogeosciences*, 10(4), 2169–2191.
- [77] Kwiatkowski, L., Torres, O., Bopp, L., Aumont, O., Chamberlain, M., Christian, J. R., Dunne, J. P., Gehlen, M., Ilyina, T., John, J. G., et al. (2020). Twenty-first century ocean warming, acidification, deoxygenation, and upper-ocean nutrient and primary production decline from cmip6 model projections. *Biogeosciences*, 17(13), 3439–3470.
- [78] Kwon, E. Y., Primeau, F., & Sarmiento, J. L. (2009). The impact of remineralization depth on the air-sea carbon balance. *Nature Geoscience*, 2(9), 630–635.
- [79] Lam, P. J. & Marchal, O. (2015). Insights into particle cycling from thorium and particle data. *Annual Review of Marine Science*, 7, 159–184.
- [80] Lampitt, R. (1985). Evidence for the seasonal deposition of detritus to the deep-sea floor and its subsequent resuspension. *Deep Sea Research Part A. Oceanographic Research Papers*, 32(8), 885–897.
- [81] Lampitt, R., Salter, I., de Cuevas, B., Hartman, S., Larkin, K., & Pebody, C. (2010). Long-term variability of downward particle flux in the deep northeast atlantic: Causes and trends. *Deep Sea Research Part II: Topical Studies in Oceanography*, 57(15), 1346–1361.
- [82] Laufkötter, C., John, J. G., Stock, C. A., & Dunne, J. P. (2017). Temperature and oxygen dependence of the remineralization of organic matter. *Global Biogeochemical Cycles*, 31(7), 1038–1050.
- [83] Le, C., Wu, S., Hu, C., Beck, M. W., & Yang, X. (2019). Phytoplankton decline in the eastern north pacific transition zone associated with atmospheric blocking. *Global change biology*, 25(10), 3485–3493.
- [84] Le Moigne, F. A., Henson, S., Sanders, R., & Madsen, E. (2013). Global database of surface ocean particulate organic carbon export fluxes diagnosed from the ^{234}Th technique. *Earth System Science Data*, 5(2), 295–304.
- [85] Leblanc, K., Hare, C., Feng, Y., Berg, G., DiTullio, G., Neeley, A., Benner, I., Sprengel, C., Beck, A., Sanudo-Wilhelmy, S., et al. (2009). Distribution of calcifying and silicifying phytoplankton in relation to environmental and biogeochemical parameters during the late stages of the 2005 north east atlantic spring bloom. *Biogeosciences*, 6(10), 2155–2179.
- [86] Lehodey, P., Hampton, J., Brill, R. W., Nicol, S., Senina, I., Calmettes, B., Pörtner, H. O., Bopp, L., Ilyina, T., Bell, J. D., et al. (2011). Vulnerability of oceanic fisheries in the tropical pacific to climate change. *Vulnerability of tropical Pacific fisheries and aquaculture to climate change*, (pp. 433–492).

- [87] Lévy, M., Couespel, D., Haëck, C., Keerthi, M. G., Mangolte, I., & Prend, C. J. (2024). The impact of fine-scale currents on biogeochemical cycles in a changing ocean. *Annual Review of Marine Science*, 16, 191–215.
- [88] Lévy, M., Ferrari, R., Franks, P. J., Martin, A. P., & Rivière, P. (2012a). Bringing physics to life at the submesoscale. *Geophysical Research Letters*, 39(14).
- [89] Lévy, M., Iovino, D., Resplandy, L., Klein, P., Madec, G., Tréguier, A.-M., Masson, S., & Takahashi, K. (2012b). Large-scale impacts of submesoscale dynamics on phytoplankton: Local and remote effects. *Ocean Modelling*, 43, 77–93.
- [90] Lévy, M., Klein, P., Tréguier, A.-M., Iovino, D., Madec, G., Masson, S., & Takahashi, K. (2010). Modifications of gyre circulation by sub-mesoscale physics. *Ocean Modelling*, 34(1-2), 1–15.
- [91] Lévy, M., Resplandy, L., Klein, P., Capet, X., Iovino, D., & Éthé, C. (2012c). Grid degradation of submesoscale resolving ocean models: Benefits for offline passive tracer transport. *Ocean Modelling*, 48, 1–9.
- [92] Lévy, M., Resplandy, L., Palter, J. B., Couespel, D., & Lachkar, Z. (2022). The crucial contribution of mixing to present and future ocean oxygen distribution. In *Ocean mixing* (pp. 329–344). Elsevier.
- [93] Liao, E., Resplandy, L., Liu, J., & Bowman, K. W. (2020). Amplification of the ocean carbon sink during el niños: Role of poleward ekman transport and influence on atmospheric co₂. *Global Biogeochemical Cycles*, 34(9), e2020GB006574.
- [94] Liu, G., Bracco, A., & Passow, U. (2018). The influence of mesoscale and submesoscale circulation on sinking particles in the northern gulf of mexico. *Elem Sci Anth*, 6, 36.
- [95] Lochte, K., Ducklow, H., Fasham, M., & Stienen, C. (1993). Plankton succession and carbon cycling at 47° n 20° w during the jgofs north atlantic bloom experiment. *Deep Sea Research Part II: Topical Studies in Oceanography*, 40(1-2), 91–114.
- [96] Luo, H., Zheng, F., Keenlyside, N., & Zhu, J. (2020). Ocean–atmosphere coupled pacific decadal variability simulated by a climate model. *Climate Dynamics*, 54, 4759–4773.
- [97] Maas, A. E., Frazar, S. L., Outram, D. M., Seibel, B. A., & Wishner, K. F. (2014). Fine-scale vertical distribution of macroplankton and microneuston in the eastern tropical north pacific in association with an oxygen minimum zone. *Journal of plankton research*, 36(6), 1557–1575.
- [98] Madec, G., Bourdallé-Badie, R., Bouttier, P.-A., Bricaud, C., Bruciaferri, D., Calvert, D., Chanut, J., Clementi, E., Coward, A., Delrosso, D., et al. (2017). Nemo ocean engine.
- [99] Mahadevan, A. (2016). The impact of submesoscale physics on primary productivity of plankton. *Annual review of marine science*, 8, 161–184.
- [100] Mahadevan, A., D'asaro, E., Lee, C., & Perry, M. J. (2012). Eddy-driven stratification initiates north atlantic spring phytoplankton blooms. *Science*, 337(6090), 54–58.
- [101] Maritorena, S., d'Andon, O. H. F., Mangin, A., & Siegel, D. A. (2010). Merged satellite ocean color data products using a bio-optical model: Characteristics, benefits and issues. *Remote Sensing of Environment*, 114(8), 1791–1804.
- [102] Martin, J. H. & Fitzwater, S. E. (1988). Iron deficiency limits phytoplankton growth in the north-east pacific subarctic. *Nature*, 331(6154), 341–343.

- [103] Martin, J. H., Knauer, G. A., Karl, D. M., & Broenkow, W. W. (1987). Vertex: carbon cycling in the northeast pacific. *Deep Sea Research Part A. Oceanographic Research Papers*, 34(2), 267–285.
- [104] McDonnell, A. M. & Buesseler, K. O. (2010). Variability in the average sinking velocity of marine particles. *Limnology and Oceanography*, 55(5), 2085–2096.
- [105] McGillicuddy Jr, D. J. (2016). Mechanisms of physical-biological-biogeochemical interaction at the oceanic mesoscale. *Annual Review of Marine Science*, 8, 125–159.
- [106] Munk, W. H. & Riley, G. A. (1952). Absorption of nutrients by aquatic plants.
- [107] Olsen, A., Key, R. M., Van Heuven, S., Lauvset, S. K., Velo, A., Lin, X., Schirnick, C., Kozyr, A., Tanhua, T., Hoppema, M., et al. (2016). The global ocean data analysis project version 2 (glodapv2)—an internally consistent data product for the world ocean. *Earth System Science Data*, 8(2), 297–323.
- [108] Omand, M. M., D'Asaro, E. A., Lee, C. M., Perry, M. J., Briggs, N., Cetinić, I., & Mahadevan, A. (2015). Eddy-driven subduction exports particulate organic carbon from the spring bloom. *Science*, 348(6231), 222–225.
- [109] Omand, M. M., Govindarajan, R., He, J., & Mahadevan, A. (2020). Sinking flux of particulate organic matter in the oceans: Sensitivity to particle characteristics. *Scientific reports*, 10(1), 5582.
- [110] Owens, S., Buesseler, K., & Sims, K. (2011). Re-evaluating the ^{238}U -salinity relationship in seawater: Implications for the ^{238}U – ^{234}Th disequilibrium method. *Marine Chemistry*, 127(1-4), 31–39.
- [111] Palevsky, H. I. & Doney, S. C. (2021). Sensitivity of 21st century ocean carbon export flux projections to the choice of export depth horizon. *Global Biogeochemical Cycles*, 35(2), e2020GB006790.
- [112] Pellant, N. A., Eriksen, C. C., & Cronin, M. F. (2017). Seaglider surveys at ocean station papa: Diagnosis of upper-ocean heat and salt balances using least squares with inequality constraints. *Journal of Geophysical Research: Oceans*, 122(6), 5140–5168.
- [113] Peña, M. A., Nemcek, N., & Robert, M. (2019). Phytoplankton responses to the 2014–2016 warming anomaly in the northeast subarctic pacific ocean. *Limnology and Oceanography*, 64(2), 515–525.
- [114] Peña, M. A. & Varela, D. E. (2007). Seasonal and interannual variability in phytoplankton and nutrient dynamics along line p in the ne subarctic pacific. *Progress in Oceanography*, 75(2), 200–222.
- [115] Plant, J. N., Johnson, K. S., Sakamoto, C. M., Jannasch, H. W., Coletti, L. J., Riser, S. C., & Swift, D. D. (2016). Net community production at ocean station papa observed with nitrate and oxygen sensors on profiling floats. *Global Biogeochemical Cycles*, 30(6), 859–879.
- [116] Polovina, J. J., Howell, E., Kobayashi, D. R., & Seki, M. P. (2001). The transition zone chlorophyll front, a dynamic global feature defining migration and forage habitat for marine resources. *Progress in oceanography*, 49(1-4), 469–483.
- [117] Resplandy, L., Lévy, M., & McGillicuddy Jr, D. J. (2019). Effects of eddy-driven subduction on ocean biological carbon pump. *Global Biogeochemical Cycles*, 33(8), 1071–1084.
- [118] Resplandy, L., Martin, A. P., Le Moigne, F., Martin, P., Aquilina, A., Mémery, L., Lévy, M., & Sanders, R. (2012). How does dynamical spatial variability impact ^{234}Th -derived estimates of organic export? *Deep Sea Research Part I: Oceanographic Research Papers*, 68, 24–45.

- [119] Riley, J., Sanders, R., Marsay, C., Le Moigne, F. A., Achterberg, E. P., & Poulton, A. J. (2012). The relative contribution of fast and slow sinking particles to ocean carbon export. *Global Biogeochemical Cycles*, 26(1).
- [120] Roca-Martí, M., Benitez-Nelson, C. R., Umhau, B. P., Wyatt, A. M., Clevenger, S. J., Pike, S., Horner, T. J., Estapa, M. L., Resplandy, L., & Buesseler, K. O. (2021). Concentrations, ratios, and sinking fluxes of major bioelements at ocean station papa. *Elem Sci Anth*, 9(1), 00166.
- [121] Roy-Barman, M., Thil, F., Bordier, L., Dapoigny, A., Foliot, L., Ayrault, S., Lacan, F., Jeandel, C., Pradoux, C., & Garcia-Solsona, E. (2019). Thorium isotopes in the southeast atlantic ocean: Tracking scavenging during water mass mixing along neutral density surfaces. *Deep Sea Research Part I: Oceanographic Research Papers*, 149, 103042.
- [122] Savoye, N., Benitez-Nelson, C., Burd, A. B., Cochran, J. K., Charette, M., Buesseler, K. O., Jackson, G. A., Roy-Barman, M., Schmidt, S., & Elskens, M. (2006). 234th sorption and export models in the water column: A review. *Marine Chemistry*, 100(3-4), 234–249.
- [123] Seitzinger, S. P., Mayorga, E., Bouwman, A. F., Kroese, C., Beusen, A. H., Billen, G., Van Drecht, G., Dumont, E., Fekete, B., Garnier, J., et al. (2010). Global river nutrient export: A scenario analysis of past and future trends. *Global biogeochemical cycles*, 24(4).
- [124] Shatova, O., Kowek, D., Conte, M. H., & Weber, J. C. (2012). Contribution of zooplankton fecal pellets to deep ocean particle flux in the sargasso sea assessed using quantitative image analysis. *Journal of plankton research*, 34(10), 905–921.
- [125] Siegel, D., Buesseler, K., Doney, S. C., Sailley, S., Behrenfeld, M. J., & Boyd, P. (2014). Global assessment of ocean carbon export by combining satellite observations and food-web models. *Global Biogeochemical Cycles*, 28(3), 181–196.
- [126] Siegel, D., Doney, S., & Yoder, J. (2002). The north atlantic spring phytoplankton bloom and sverdrup's critical depth hypothesis. *science*, 296(5568), 730–733.
- [127] Siegel, D. A., Buesseler, K. O., Behrenfeld, M. J., Benitez-Nelson, C. R., Boss, E., Brzezinski, M. A., Burd, A., Carlson, C. A., D'Asaro, E. A., Doney, S. C., et al. (2016). Prediction of the export and fate of global ocean net primary production: The exports science plan. *Frontiers in Marine Science*, 3, 22.
- [128] Siegel, D. A., Cetinić, I., Graff, J. R., Lee, C. M., Nelson, N., Perry, M. J., Ramos, I. S., Steinberg, D. K., Buesseler, K., Hamme, R., et al. (2021). An operational overview of the export processes in the ocean from remote sensing (exports) northeast pacific field deployment. *Elem Sci Anth*, 9(1), 00107.
- [129] Siegelman, L., Klein, P., Rivière, P., Thompson, A. F., Torres, H. S., Flexas, M., & Menemenlis, D. (2020). Enhanced upward heat transport at deep submesoscale ocean fronts. *Nature Geoscience*, 13(1), 50–55.
- [130] Steinberg, D. K. & Landry, M. R. (2017). Zooplankton and the ocean carbon cycle. *Annual review of marine science*, 9, 413–444.
- [131] Stock, C. A., Dunne, J. P., Fan, S., Ginoux, P., John, J., Krasting, J. P., Laufkötter, C., Paulot, F., & Zadeh, N. (2020). Ocean biogeochemistry in gfdl's earth system model 4.1 and its response to increasing atmospheric co₂. *Journal of Advances in Modeling Earth Systems*, 12(10), e2019MS002043.
- [132] Stock, C. A., Dunne, J. P., & John, J. G. (2014). Global-scale carbon and energy flows through the marine planktonic food web: An analysis with a coupled physical–biological model. *Progress in Oceanography*, 120, 1–28.

- [133] Stukel, M. R., Aluwihare, L. I., Barbeau, K. A., Chekalyuk, A. M., Goericke, R., Miller, A. J., Ohman, M. D., Ruacho, A., Song, H., Stephens, B. M., et al. (2017). Mesoscale ocean fronts enhance carbon export due to gravitational sinking and subduction. *Proceedings of the National Academy of Sciences*, 114(6), 1252–1257.
- [134] Stukel, M. R., Song, H., Goericke, R., & Miller, A. J. (2018). The role of subduction and gravitational sinking in particle export, carbon sequestration, and the remineralization length scale in the California current ecosystem. *Limnology and Oceanography*, 63(1), 363–383.
- [135] Suryan, R. M., Arimitsu, M. L., Coletti, H. A., Hopcroft, R. R., Lindeberg, M. R., Barbeaux, S. J., Batten, S. D., Burt, W. J., Bishop, M. A., Bodkin, J. L., et al. (2021). Ecosystem response persists after a prolonged marine heatwave. *Scientific reports*, 11(1), 6235.
- [136] Thomas, L. N., Tandon, A., & Mahadevan, A. (2008). Submesoscale processes and dynamics. *Ocean modeling in an Eddying Regime*, 177, 17–38.
- [137] Timothy, D., Wong, C., Barwell-Clarke, J., Page, J., White, L., & Macdonald, R. (2013). Climatology of sediment flux and composition in the subarctic northeast Pacific ocean with biogeochemical implications. *Progress in Oceanography*, 116, 95–129.
- [138] Tsujino, H., Urakawa, S., Nakano, H., Small, R. J., Kim, W. M., Yeager, S. G., Danabasoglu, G., Suzuki, T., Bamber, J. L., Bentsen, M., et al. (2018). Jra-55 based surface dataset for driving ocean-sea-ice models (jra55-do). *Ocean Modelling*, 130, 79–139.
- [139] Turnewitsch, R. & Springer, B. M. (2001). Do bottom mixed layers influence 234th dynamics in the abyssal near-bottom water column? *Deep Sea Research Part I: Oceanographic Research Papers*, 48(5), 1279–1307.
- [140] Waite, A. M., Stemmann, L., Guidi, L., Calil, P. H., Hogg, A. M. C., Feng, M., Thompson, P. A., Picheral, M., & Gorsky, G. (2016). The wineglass effect shapes particle export to the deep ocean in mesoscale eddies. *Geophysical Research Letters*, 43(18), 9791–9800.
- [141] Wang, W.-L., Fu, W., Le Moigne, F. A., Letscher, R. T., Liu, Y., Tang, J.-M., & Primeau, F. W. (2023). Biological carbon pump estimate based on multidecadal hydrographic data. *Nature*, 624(7992), 579–585.
- [142] Waples, J. T., Benitez-Nelson, C., Savoye, N., van der Looff, M. R., Baskaran, M., & Gustafsson, Ö. (2006). An introduction to the application and future use of 234th in aquatic systems. *Marine Chemistry*, 100(3-4), 166–189.
- [143] Waythomas, C. F., Haney, M. M., Fee, D., Schneider, D. J., & Wech, A. (2014). The 2013 eruption of Pavlof volcano, Alaska: a spatter eruption at an ice-and snow-clad volcano. *Bulletin of Volcanology*, 76, 1–12.
- [144] Whitney, F. A. (2015). Anomalous winter winds decrease 2014 transition zone productivity in the North Pacific. *Geophysical Research Letters*, 42(2), 428–431.
- [145] Wong, C., Waser, N., Nojiri, Y., Whitney, F., Page, J., & Zeng, J. (2002). Seasonal cycles of nutrients and dissolved inorganic carbon at high and mid latitudes in the North Pacific Ocean during the Skagway cruises: determination of new production and nutrient uptake ratios. *Deep Sea Research Part II: Topical Studies in Oceanography*, 49(24-25), 5317–5338.

- [146] Wyatt, A. M., Resplandy, L., & Marchetti, A. (2022). Ecosystem impacts of marine heat waves in the northeast pacific. *Biogeosciences*, 19(24), 5689–5705.
- [147] Xie, R., Le Moigne, F. A., Rapp, I., Lüdke, J., Gasser, B., Dengler, M., Liebetrau, V., & Achterberg, E. P. (2020). Effects of 238 u variability and physical transport on water column 234 th downward fluxes in the coastal upwelling system off peru. *Biogeosciences Discussions*, 2020, 1–42.
- [148] Xu, T., Newman, M., Capotondi, A., & Di Lorenzo, E. (2021). The continuum of northeast pacific marine heatwaves and their relationship to the tropical pacific. *Geophysical Research Letters*, 48(2), 2020GL090661.
- [149] Yang, B., Emerson, S. R., & Peña, M. A. (2018). The effect of the 2013–2016 high temperature anomaly in the subarctic northeast pacific (the “blob”) on net community production. *Biogeosciences*, 15(21), 6747–6759.
- [150] Yang, B., Fox, J., Behrenfeld, M. J., Boss, E. S., Haëntjens, N., Halsey, K. H., Emerson, S. R., & Doney, S. C. (2021). In situ estimates of net primary production in the western north atlantic with argo profiling floats. *Journal of Geophysical Research: Biogeosciences*, 126(2), e2020JG006116.



T HIS is an adventure.

– Steve Zissou